

Experimental Investigation of Strain Distributions and Polarization in Lead-based and Lead-free Ferroelec- trics

zur Erlangung des akademischen Grades eines
Doktors der Ingenieurwissenschaften

von der Fakultät für Maschinenbau
des Karlsruher Instituts für Technologie (KIT)

genehmigte

Dissertation

von

Di Chen

aus Shanxi, China

Tag der mündlichen Prüfung: 27. April 2017
Erster Gutachter: Prof. Dr. Marc Kamlah
Zweiter Gutachter: Prof. Dr. Michael J. Hoffmann



This document is licensed under the Creative Commons Attribution –
Share Alike 4.0 International License (CC BY-SA 4.0):
<https://creativecommons.org/licenses/by-sa/4.0/deed.de>

Kurzfassung

Experimentelle Untersuchung von Dehnungsverteilungen und Polarisation in bleihaltigen und bleifreien Ferroelektrika

Die experimentelle Untersuchung von Dehnungen und Polarisationszuständen in bleibasierten und bleifreien Ferroelektrika induziert durch einachsige Belastungen wurde in dieser Arbeit durchgeführt. In dieser Studie wurden kommerziell erhältliches, weiches PZT (PIC 151), sowie $(\text{Na}_{1/2}\text{Bi}_{1/2})\text{TiO}_3$ -basierte bleifreie Piezokeramiken untersucht. Die bleifreien Proben umfassen die reinen $0.93(\text{Na}_{1/2}\text{Bi}_{1/2})\text{TiO}_3$ - 0.07BaTiO_3 (NBT-7BT) und $0.91(\text{Na}_{1/2}\text{Bi}_{1/2})\text{TiO}_3$ - 0.06BaTiO_3 - $0.03\text{K}_{0.5}\text{Na}_{0.5}\text{NbO}_3$ (NBT-6BT-3KNN) Keramiken, sowie aus beiden bleifreien Keramiken bestehende Doppelschicht- und Dreischicht-„Sandwich“-Verbundwerkstoffe. Die elektromechanischen Eigenschaften dieser Materialien wurden an zwei Versuchsständen gemessen. Einer wurde zur Untersuchung der durch das elektrische Feld induzierten Dehnungen und Polarisationen verwendet, der andere zur Beobachtung der Verformung der Piezokeramiken unter einachsigem Druck entwickelt.

Für die PZT-Proben wurden die Deformationen, die entweder durch ein bipolares elektrisches Feld oder durch eine reine Druckspannung verursacht wurden, getrennt voneinander untersucht. Gleichzeitig konnten die Polarisationen, die durch die elektrischen Felder und die mechanischen Belastungen hervorgerufen werden, gemessen werden. Die digitale Bildkorrelationsmethode (DIC) wurde angewandt, um die Verformung der Proben unter stärkeren elektrischen Feldern und Spannungen nachzuverfolgen. Longitudinale und transversale Dehnungen wurden mithilfe von Aufnahmen der Proben unter einem elektrischen Feld von ± 2 kV/mm berechnet. Durch Vergleich mit den Daten eines linearen Wegaufnehmers (LVDT) wurden die Ergebnisse der DIC-Methode validiert. Die Untersuchung der Dehnungsverteilung an der Probenoberfläche zeigt, dass die durch elektrisches Feld induzierte Verformung von Keramiken auf der makroskopischen Beobachtungsskala homogen ist.

Die mechanischen Druckversuche wurden an PZT-Proben mit einem Aspektverhältnis von 3:1 durchgeführt. Aufgrund der Reibung an der Ober- und Unter Oberfläche der PZT-Keramikproben ist die Verformungsverteilung unter großen, uniaxialen Druckspannungen üblicherweise tonnenförmig, welche mittels der Ergebnisse der Dehnungsverteilungen nachgewiesen wurde. Dieser mechanische Druckversuch rechtfertigt experimentell die Auswahl eines Aspektverhältnisses von 3: 1 für die Proben, da lediglich deren zentraler, quadratischer Bereich den gewünschten Zustand einer rein einachsigen Belastung repräsentiert.

Die NBT-7BT- und die NBT-6BT-3KNN-Keramiken wurden sowohl mittels zyklischer, als auch konstanter elektrischer Felder belastet. Aufgrund der Eigenschaften des nicht-ergodischen und ergodischen Relaxors in NBT-7BT und NBT-6BT-3KNN zeigen die gemessenen Polarisations-Spannungsfeld (P - E)- und Dehnungs-Spannungsfeld (S - E)-Zyklen erkennbare Unterschiede für beide Keramiken. Um ein besseres Verständnis des ergodischen und nicht-ergodischen Verhaltens der beiden Relaxoren zu erhalten, wurde das Kriechverhalten beider Keramiken in einem konstanten elektrischen Feld gemessen. Ein sogenanntes „zweistufiges“ Kaskade-Phänomen kann bei einer ungepolten NBT-7BT Probe beobachtet werden, wenn das elektrische Feld für längere Zeit über einem bestimmten Schwellwert gehalten wird. Dagegen kann dieser Effekt bei den NBT-6BT-3KNN-Proben nicht beobachtet werden. Das zeitabhängige elektromechanische Verhalten zeigt, dass das Kriechen schrittweise abnimmt und schließlich eine Sättigung erreicht.

Die DIC-Methode wurde auch zur Untersuchung der durch das elektrische Feld induzierten Verformung auf die NBT-6BT-3KNN/NBT-7BT-Doppelschicht- und NBT-6BT-3KNN/NBT-7BT/NBT-6BT-3KNN-Dreischichtverbundmaterialien angewandt. Durch die Auswahl eines geeigneten Untersuchungsbereichs (ROIs) in jeder Schicht und der Berechnung der lokalen Dehnungen kann die Dehnungsverteilung bestimmt werden. Alle diese Ergebnisse wurden durch Vergleich der reinen-, der Doppelschicht- und der Dreischicht-Proben anhand der bipolaren longitudinalen Dehnungen und der Polarisationszyklen aufgelistet. Obwohl die internen Spannungen, die durch die Variation der Sintergeschwindigkeiten zwischen den beiden Schichten verursacht wurden, fehlen, wurden die Spannungen ungefähr mittels der Dehnungen ermittelt. Diese Datensätze der Dehnungsverteilungen schlagen eine Brücke zum Aufbau eines Modells, welches die Kopplung der Polarisation und der Dehnung berücksichtigt, um schließlich zu einem besseren Verständnis des elektromechanischen Verhaltens zu gelangen.

Abstract

Experimental Investigation of Strain Distributions and Polarization in Lead-based and Lead-free Ferroelectrics

Experimental investigation of strain and polarization induced by uniaxial loads in lead-based and lead-free ferroelectrics was performed in this work. The commercial soft PZT (PIC 151) and $(\text{Na}_{1/2}\text{Bi}_{1/2})\text{TiO}_3$ -based lead-free piezoceramics are the main objects of this study. The lead-free specimens include pure $0.93(\text{Na}_{1/2}\text{Bi}_{1/2})\text{TiO}_3$ - 0.07BaTiO_3 (NBT-7BT) ceramics, pure $0.91(\text{Na}_{1/2}\text{Bi}_{1/2})\text{TiO}_3$ - 0.06BaTiO_3 - $0.03\text{K}_{0.5}\text{Na}_{0.5}\text{NbO}_3$ (NBT-6BT-3KNN) ceramics, bilayer composites and trilayer “sandwich” composites based on these two pure lead-free materials. The electromechanical properties of these materials were measured by using two setups. One is designed for checking the electric field-induced strain and polarization, the other is assembled for monitoring the deformation of piezoceramics under uniaxial compression.

For the PZT samples, the deformation induced by a pure bipolar electric field and a pure compressive stress were monitored, respectively. Simultaneously, the polarization can be obtained during the electric field and compressive loadings. The digital image correlation (DIC) method was employed to monitor the deformation under larger signal electric field and stress. Both the longitudinal and transverse strains were calculated from imaging a bulk sample under a ± 2 kV/mm electric field. Compared with linear variable displacement transducer (LVDT) data, the results from this correlation method were validated. The checking of strain distribution on the surface of the sample reveals that electric field-induced deformation of bulk ceramic without any mechanical constraints is highly homogenous at the macroscopic scale.

A mechanical compressive was loaded at the PZT bulk specimens with an aspect ratio of 3:1. Because of the friction at both the top and bottom surfaces of the PZT ceramic specimen, the deformation of the sample under a large uniaxial compressive stress usually shows a barrel shape which was proved by the results of the strain distribution. This mechanical compressive loading test provides the experimental justifications for the selection of an aspect ratio of 3:1 for the specimen, where only the central cubic region of a specimen represents the desired purely uniaxial stress state.

Both the NBT-7BT and NBT-6BT-3KNN ceramics were loaded by the cyclic electric fields and constant electric fields. Due to the properties of nonergodic relaxor and ergodic relaxor in NBT-7BT and NBT-6BT-3KNN, respectively, the polarization-electric field (P - E) loop and strain-electric field (S - E) loop measured from the two ceramics show obvious differences. With the purpose of obtaining a better understanding of the nonergodic and ergodic behaviors in the two relaxors, the creep in these two ceramics induced by a constant electric field was measured. A so-called “two-stage” cascade phenomenon can be obtained from an unpoled NBT-7BT specimen when the electric field is higher than a certain value and held there for a long time. However, this effect cannot be observed on the NBT-6BT-3KNN specimens. The time-dependent electromechanical behavior shows that creep reduces gradually and reaches saturation eventually.

The DIC method was also used for monitoring the electric field-induced deformations of NBT-6BT-3KNN/NBT-7BT bilayer and NBT-6BT-3KNN/NBT-7BT/NBT-6BT-3KNN trilayer composites. By means of selecting the regions of interest (ROIs) located on each layer and calculating the strains there, the strain distribution can be achieved. All these results were listed in a comparison of bipolar longitudinal strain and polarization loops among the two pure components, bilayer composites and trilayer composites. Although the internal stresses induced by the variation in sintering rates between the layers are missing, the stress states in each layer were estimated roughly by using the strain data. Especially, these

data of strain distributions provide a bridge to build a model considering both the polarization coupling and strain coupling to obtain a better understanding of this electromechanical behavior.

Contents

Kurzfassung	i
Abstract	iii
Contents	v
List of figures	vii
List of tables	x
Symbols and abbreviations used in this work	xi
1 Introduction and motivation	1
1.1 Ferroelectric materials.....	2
1.1.1 Ferroelectricity in ceramics.....	2
1.1.2 Piezoelectricity in ferroelectric ceramics	5
1.2 Lead-based piezoceramics.....	8
1.2.1 Ferroelectric and relaxor ferroelectric in lead-based piezoceramics	8
1.2.2 Lead zirconate titanate (PZT) applied on actuators.....	9
1.3 Lead-free piezoceramics	11
1.3.1 Three base-systems: Barium Titanate (BT), Potassium Sodium Niobate (KNN) and Sodium Bismuth Titanate (NBT).....	12
1.3.2 NBT-BT binary solid solution	13
1.3.3 NBT-BT-KNN ternary solid solution	14
1.3.4 Electric field-induced ergodic and nonergodic behavior in NBT-based ceramics	15
1.3.5 Improvements on lead-free ceramics for actuator applications.....	17
2 Digital image correlation (DIC) method	20
2.1 Motivation	20
2.2 Fundamentals	21
3 Specimens, experimental setups and methods	23
3.1 PIC151 soft PZT, NBT-7BT and NBT-6BT-3KNN	23
3.2 Experimental setups for the investigations.....	24
3.3 Implementation of DIC method in this work	25
3.4 Error analysis on the strain measured from DIC method	27
3.4.1 Errors from the DIC codes and the setup	27
3.4.2 Noise caused by the motion of insulating liquid	28
4 Deformation behavior on PZT samples	30
4.1 Experiments under electric field loadings	30
4.1.1 Experimental procedures.....	30
4.1.2 Validation of the DIC method.....	31
4.1.3 Strain measured from DIC displacement gauge.....	33

4.1.4	Spatial distribution of the strain components	34
4.2	Experiments under mechanical compressive stress loadings.....	36
4.2.1	Experimental procedures.....	36
4.2.2	Strain measurement on single region of interest	37
4.2.3	Strain measurement on multi-regions of interest.....	38
4.2.4	Spatial distribution of the strain components	41
4.3	Summary	44
5	Experiments on NBT-7BT under electric field loadings	45
5.1	Polarization and strain responses under bipolar loadings	45
5.2	Electromechanical responses under a constant electric field.....	47
5.2.1	Experimental procedures.....	47
5.2.2	Results and discussions	48
5.3	Summary	54
6	Experiments on NBT-6BT-3KNN under electric field loadings	55
6.1	Polarization and strain responses under bipolar loadings	55
6.2	Electromechanical responses under a constant electric field.....	56
6.2.1	Experimental procedures.....	57
6.2.2	Results and discussion.....	57
6.3	Summary	65
7	Experiments on NBT-7BT/NBT-6BT-3KNN composites under electric field loadings.....	66
7.1	Introduction	66
7.2	Experimental procedures	67
7.3	Electromechanical behavior on the two end member materials	67
7.4	Experiments on bilayer composite	69
7.4.1	Initial state selected for DIC tracing.....	69
7.4.2	Polarization and strains in bilayer	70
7.5	Experiments on trilayer composite.....	76
7.5.1	Initial state of trilayer selected for DIC tracing.....	76
7.5.2	Polarization and strains in trilayer.....	77
7.6	Summary	79
8	Summary of this thesis	80
	References.....	82
	Acknowledgements.....	94
	Curriculum Vitae	95

List of figures

Figure 1.1:	Classification of dielectrics.....	1
Figure 1.2:	Interrelationship of piezoelectrics and subgroups on the basis of symmetry (after Ref. [9]).	2
Figure 1.3:	Crystal structure of BaTiO ₃ . Left: Unit cell of BaTiO ₃ in the paraelectric phase. The symmetry of cubic shape does not allow for a spontaneous polarization. Right: Unit cell of BaTiO ₃ in the ferroelectric phase. The vector of spontaneous polarization P_{spont} is oriented in the direction of the displaced titanium ion (after Ref. [13]).	3
Figure 1.4:	At the paraelectric ferroelectric phase transition, six different directions for the central titanium ion to be displaced in a tetragonal structure, resulting in six different spontaneous polarization vectors (after Ref. [13])......	4
Figure 1.5:	Evolution of domain orientation under a poling process (after Ref. [16]).	4
Figure 1.6:	Polarization-electric field (P-E) loops of PIC 151 commercial PZT ceramics. ① to ⑦ indicate domain states schematically (after Ref. [13])......	6
Figure 1.7:	Strain-electric field (S-E) butterfly curves of PIC 151 commercial PZT ceramics. ① to ⑦ indicate domain states schematically (after Ref. [13])......	6
Figure 1.8:	A mechanical stress σ of sufficient magnitude induced domain switching (after Ref. [13]).	7
Figure 1.9:	Compressive stress induced: (a) depolarization curve and (b) longitudinal strain (after Ref. [22, 23]).	8
Figure 1.10:	Comparison of ferroelectrics and relaxor ferroelectrics in terms of polarization (left), and relative permittivity (right) (after Ref. [25]).	9
Figure 1.11:	Electric field-induced strains (black curves, longitudinal strains; red curves, transverse strains) at room temperature of (a) pure BT, (b) pure KNN, and (c) pure NBT with the associated volume change (blue curves), measured during bipolar poling cycle at 50 mHz (after Ref. [54]).	12
Figure 1.12:	Temperature dependent P-E loops of NBT-6BT ceramic (after Ref. [77]).	13
Figure 1.13:	Temperature dependent S-E loops of NBT-6BT ceramic (after Ref. [77])......	14
Figure 1.14:	Bipolar strain hysteresis of NBT-BT-KNN system near the composition 0.94NBT-0.06BT (after Ref. [54])......	14
Figure 1.15:	The nature of the electric field-induced phase transition observed in NBT-6BT (left) and NBT-6BT-2KNN (right). FE, NR and ER denote ferroelectric, non-ergodic relaxor and ergodic relaxor phase, respectively (after Ref. [54]).	15
Figure 1.16:	The large signal piezoelectric coefficient as a function of depolarization temperature for KNN-based [7, 56, 104-106], BCZT [6, 107-110], NBT-based [56, 77, 88, 111, 112], NBT-based Incipient piezoelectrics [75, 86, 113-117] and PZT [56, 118, 119]. It is should be noticed that the maximum electric field is not always the same level for each data point (after Ref. [53]).	17
Figure 3.1:	Experimental setup for measuring electric field-induced strains	24
Figure 3.2:	Experimental setup used for compression test.....	25

Figure 3.3:	Two ROIs marked by selected the red crosses ready for DIC tracing.	26
Figure 3.4:	Three ROIs selected for calculating the corresponded strains.	28
Figure 3.5:	Longitudinal strains calculated from three ROIs on one surface: (a) results containing obvious noises; (b) results obtained from the same setup after some modifications.. ...	29
Figure 4.1:	The physical size of the sample and the selected watching window under the lens.	30
Figure 4.2:	Polarization hysteresis loops induced by cyclic electric field loadings.	31
Figure 4.3:	Reference images and regions of interest for DIC tracing (unit in coordinates is pixel).31	
Figure 4.4:	Strain-electric field curves measured by DIC method and LVDT.	32
Figure 4.5:	Longitudinal strains measured from diverse ROIs.	33
Figure 4.6:	Distributions of transverse and longitudinal strains: (a) contour plot of transverse strain measured at 0.87 kV/mm; (b) contour plot of transverse strain measured at 2 kV/mm; (c) contour plot of longitudinal strain measured at 0.87 kV/mm; (d) contour plot of longitudinal strain measured at 2 kV/mm.	34
Figure 4.7:	Transverse strain measured from diverse ROIs of Figure 3.4.	35
Figure 4.8:	Observation window of DIC and the reference image with the assigned coordination system.	36
Figure 4.9:	Three cycles of responses of compressive stress: (a) mechanical depolarization curve; (b) longitudinal and transverse strain versus stress.	37
Figure 4.10:	Selected ROIs on the surface of sample for calculating longitudinal strains.	38
Figure 4.11:	Stress-strain curves measured from R1 and R2.	39
Figure 4.12:	Selected ROIs on the surface of sample for calculating transverse strains.	39
Figure 4.13:	Stress-strain curves obtained from various ROIs.	40
Figure 4.14:	Contour plots of transverse and shear strains at 0 MPa. The plot in the upper shows the prescribed stress loading history. The red point denotes at which state of the loading history the corresponding image was taken.	42
Figure 4.15:	Contour plots of transverse and shear strains at -400 MPa.	43
Figure 4.16:	Contour plots of transverse and shear strains with the stress unloaded at 0 MPa.	43
Figure 4.17:	Schematic representations of the deformation states: (a) initial state without any compressive load; (b), (d) and (d) three hypotheses of as-deformed states.	44
Figure 5.1:	Loading history for one cycle of electric field loading.	45
Figure 5.2:	Polarization and strain hysteresis loops induced by cyclic electric field loading: (a) polarization hysteresis loops; (b) longitudinal strain curves.	46
Figure 5.3:	Two loading histories applied to the NBT-7BT specimens.	47
Figure 5.4:	Longitudinal strain and polarization as a function of time: (a) measured strains; (b) measured charge per specimen surface area including charges from leakage; (c) polarization under various static electric fields.	48
Figure 5.5:	Two portions of the strain response measured at 1.8 kV/mm.	50
Figure 5.6:	Comparison of the magnitudes of creep responses under various constant electric fields.51	
Figure 5.7:	Longitudinal strains under three times of the constant electric field loadings of 1.1 kV/mm and under a constant electric field of 1.15 kV/mm with 3600 s holding time. .	52
Figure 5.8:	Measured d_{33} after various constant electric field loadings.	52
Figure 5.9:	Longitudinal strain (a) and polarization (b) as a function of time measured on poled specimens.	53

Figure 6.1:	Polarization and strain hysteresis loops of NBT-6BT-3KNN induced by cyclic electric field loading: (a) polarization hysteresis loops; (b) longitudinal strain curves.	56
Figure 6.2:	Two loading histories applied to the specimens of NBT-BT-3KNN.....	57
Figure 6.3:	Longitudinal strain and polarization as a function of time: (a) measured strains; (b) measured charge per specimen surface area including charges from leakage; (c) polarization as a function of static electric fields.	59
Figure 6.4:	The creep behavior as a function of time: (a) two parts of the measured strain at 3 kV/mm; (b) measured creep strains with their fitting curves; (c) creep polarizations with their fitting curves.	60
Figure 6.5:	Polarization measured under constant electric fields controlled at both the loading and unloading periods: (a) polarization responses as a function of static and dynamic electric field loadings; (b) electric field and time dependent polarization responses.	63
Figure 6.6:	Strain measured under constant electric fields controlled at both the loading and unloading periods: (a) static and dynamic electric field and time dependent strain responses; (b) strain responses under constant electric fields plotted as a function of time.	64
Figure 7.1:	Polarization curves measured from NBT-7BT and NBT-6BT-3KNN ceramics independently.....	67
Figure 7.2:	Longitudinal and transverse strains measured from NBT-7BT and NBT-6BT-3KNN ceramics under cyclic electric field loadings.	68
Figure 7.3:	Volume changes of the two specimens.	69
Figure 7.4:	Reference images of bilayer composites: (a) digital image of specimen without artificial patterns; (b) specimen with sprayed black and white patterns; (c) selected ROIs on the surfaces of specimen.	70
Figure 7.5:	Polarization measured from the bilayer composite.	71
Figure 7.6:	Strains measured from the same composite: (a) longitudinal strains obtained from the corresponded ROIs on the surface of the specimen; (b) transverse strains obtained from the corresponded ROIs.	72
Figure 7.7:	Volume changes measured from the bilayer composite.	73
Figure 7.8:	Contour plots of longitudinal strains measured under the first half cycle of a bipolar loading.	74
Figure 7.9:	Contour plots of longitudinal strains measured at various states of electric field.	75
Figure 7.10:	Reference images of trilayer structures: (a) digital image of trilayer without artificial patterns, (b) selected ROIs on the surfaces of trilayer with sprayed black and white patterns.	76
Figure 7.11:	Polarization measured from the bilayer and trilayer composites.	77
Figure 7.12:	Strains measured from the trilayer composite: (a) longitudinal strains obtained from the corresponded ROIs on the surface of the specimen; (b) transverse strains obtained from the corresponded ROIs on the surface of the specimen.	78

List of tables

Table 1.1: Effects of typical additives on properties PZT. Ionic radii in nanometer are given in parentheses [16, 22, 49] 11

Table 3.1: Magnitude of errors in displacement and strain estimated from standard images (downloaded from Society for Experimental Mechanics)..... 27

Table 3.2: Magnitude of errors in displacement and strain estimated from a PZT specimen (a sample used in this work at static state)..... 28

Table 6.1: Volume resistivity under various static electric fields..... 61

Table 6.2: The parameters obtained from the fitted creeping curves..... 62

Table 7.1: Comparison of bipolar longitudinal strain and polarization loops 79

Symbols and abbreviations used in this work

A	Magnitudes of the creep response
a	Volume fraction of one component in a composite
AFE	Antiferroelectric
AFM	Atomic force microscopy
ASTM	American society for testing and materials
B	Fitting coefficient to describe the difficulty of a creep response to reach saturation
BCZT	$(\text{Ba}, \text{Ca})(\text{Ti}, \text{Zr})\text{O}_3$
BNT-2.5Nb	$((\text{Bi}_{1/2}(\text{Na}_{0.84}\text{K}_{0.16})_{1/2})_{0.96}\text{Sr}_{0.04})(\text{Ti}_{1-x}\text{Nb}_x)\text{O}_3$
BNT-BT-AN	$(\text{Bi}_{1/2}\text{Na}_{1/2})\text{TiO}_3\text{-BaTiO}_3\text{-AgNbO}_3$
BS	British standards
BT	BaTiO_3
CC	Correlation coefficient
d_{33}	Small-signal piezoelectric coefficient
d_{33}^*	Large-signal piezoelectric coefficient
DIC	Digital image correlation
E	Constant electric field
E_c	Coercive field
EDX	Energy dispersive X-ray spectroscopy
E_{pol}	Poling field
ϵ_r	Dielectric constant
ER	Ergodic relaxor
FE	Ferroelectric
HRTEM	High resolution transmission electron microscopy

KBT-BT-8NBT	$0.2(\text{K}_{0.5}\text{Bi}_{0.5}\text{TiO}_3\text{-BaTiO}_3)\text{-}0.8\text{Na}_{0.5}\text{Bi}_{0.5}\text{TiO}_3$
KNN	$\text{K}_{0.5}\text{Na}_{0.5}\text{NbO}_3$
k_{33}	Electromechanical coupling factor
LVDT	Linear variable displacement transducer
m	Slope of a linear fit
MPB	Morphotropic phase boundary
NBT or BNT	$(\text{Na}_{1/2}\text{Bi}_{1/2})\text{TiO}_3$ or $(\text{Bi}_{1/2}\text{Na}_{1/2})\text{TiO}_3$
NBT-6BT-3KNN	$0.91(\text{Na}_{1/2}\text{Bi}_{1/2})\text{TiO}_3\text{-}0.06\text{BaTiO}_3\text{-}0.03\text{K}_{0.5}\text{Na}_{0.5}\text{NbO}_3$
NBT-7BT	$0.93(\text{Na}_{1/2}\text{Bi}_{1/2})\text{TiO}_3\text{-}0.07\text{BaTiO}_3$
NBT-25ST	$0.75(\text{Na}_{1/2}\text{Bi}_{1/2})\text{TiO}_3\text{-}0.25\text{SrTiO}_3$
NR	Non-ergodic relaxor
OM	Optical microscope
ρ	Volume resistivity
P	Polarization
P_c	Creep polarization
PE	Paraelectric
P - E loop	Polarization-electric field loop
PFM	Piezoresponse force microscopy
P_l	Charge per specimen surface area caused by leakage current
PLZT	Lead lanthanum zirconate titanate
P_m	Measured charge per specimen surface area
PMN	Lead magnesium niobate, $\text{Pb}(\text{Mg}_{1/3}\text{Nb}_{2/3})\text{O}_3$
PNR	Polar nanoregion
PPB	Polymorphic phase boundary
P_r	Remnant polarization
P_{spont}	Spontaneous polarization
PSZT	Lead stannate zirconate titanate
PT	Lead titanate

PZ	Lead zirconate
PZN	Lead zinc niobate
PZT	Lead zirconate Titanate, $\text{PbZr}_x\text{Ti}_{(1-x)}\text{O}_3$
Q_m	Mechanical quality factor
RE	Relaxor
ROI	Region of interest
S_c	Creep strain
S - E loop	Strain-electric field loop
SEM	Scanning electron microscope
S_{\max}/E_{\max}	The ratio of maximum strain to maximum external electric field, $d_{33}^* = S_{\max}/E_{\max}$
SPS	Spark plasma sintering
t	Time
T^*	Intermediate temperature
T_B	Burns temperature
T_c	Curie temperature
T_d	Depolarization temperature
T_m	Temperature of the maximum dielectric permittivity
TEM	Transmission electron microscope
T_f	Freezing temperature
T_{F-R}	Ferroelectric-to-relaxor transition temperature
XRD	X-ray diffraction
ZNCC	Zero-normalized cross-correlation

1 Introduction and motivation

With the developing of the society and economy, more concerning is focused on the energy and environmental issues. In order to solve those problems, innovative and high-performance materials are required. Efforts to develop new environmentally friendly materials with capabilities of transforming energy have not ever been stopped. Piezoelectric materials offering excellent performances of instantaneous conversion between mechanical and electrical energy have attracted lots of interests. Owing to this feature, these materials can be used for some parts, such as in high-pressure injection of fuel to improve the fuel efficiency of an engine, energy harvest applications and stepper motors [1-3]. Besides, smart structures are another group of applications. Actuators and sensors are the main products in the those smart structures which are manufactured mostly from $\text{PbZr}_x\text{Ti}_{(1-x)}\text{O}_3$ (PZT). However, due to the lead content, the environmental concerns are raising. Lead-free materials with some properties closely matching those of PZT were fabricated to be good candidates for replacing PZT in some fields [4-7], but it is still a challenge to find a single material or a class of materials to be the alternate of the PZT completely [8]. Therefore, it is still necessary to perform investigations on both the PZT and newly developed lead-free ferroelectrics. For the actuator applications, the deformation along with polarization in ferroelectrics is needed to get a better understanding of the electromechanical behavior on these materials.

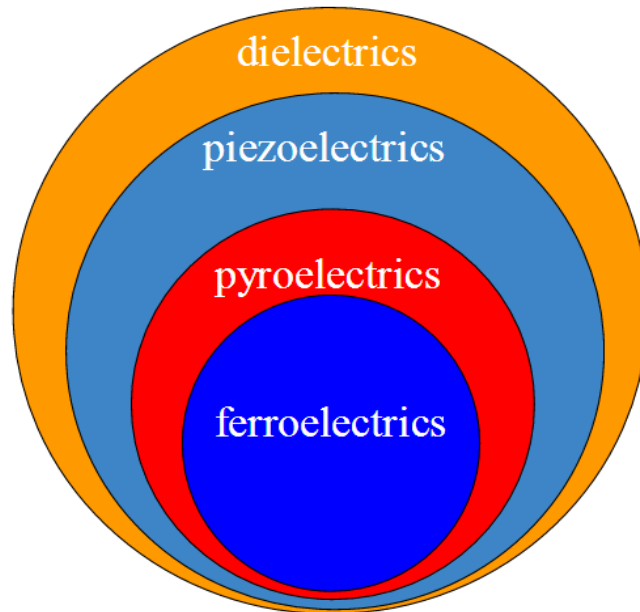


Figure 1.1: Classification of dielectrics.

In this work, soft-PZT, $0.93(\text{Na}_{1/2}\text{Bi}_{1/2})\text{TiO}_3\text{-}0.07\text{BaTiO}_3$ (NBT-7BT) and $0.91(\text{Na}_{1/2}\text{Bi}_{1/2})\text{TiO}_3\text{-}0.06\text{BaTiO}_3\text{-}0.03\text{K}_{0.5}\text{Na}_{0.5}\text{NbO}_3$ (NBT-6BT-3KNN or NBT-BT-3KNN) are used as the research objects. Digital image correlation (DIC) is the primary method used to monitor the deformations in these ceramics caused by electric fields and stresses. The introduction on the DIC method can be found in the following chapter. This chapter here focuses on the piezoelectric materials exhibit both the piezoelectricity and ferroelectricity (illustrated by Figure 1.1).

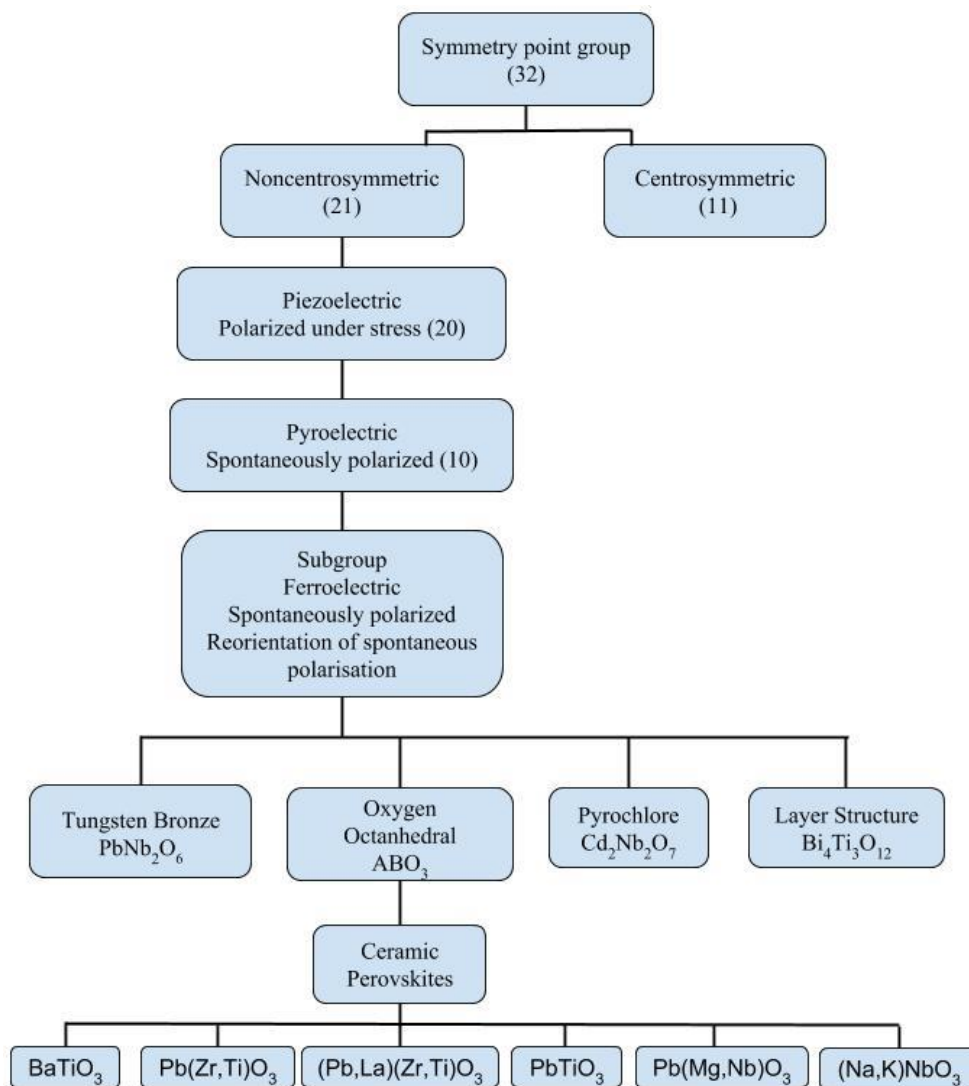


Figure 1.2: Interrelationship of piezoelectrics and subgroups on the basis of symmetry (after Ref. [9]).

1.1 Ferroelectric materials

The ferroelectric it was firstly discovered in 1921 with a single crystal structure [10]. Subsequently, polycrystalline ceramics with similar properties were reported around two decades later [11, 12]. Since then, a continuous succession of new materials and related technology has been developed. Ferroelectric materials here denote the materials possessing ferroelectricity.

1.1.1 Ferroelectricity in ceramics

Ferroelectrics are polar materials that possess at least two equilibrium orientations of the spontaneous polarization vector in the absence of an external electric, and in which the spontaneous polarization vector may be switched between those orientations by an electric field. According to that, the spontaneous dipoles in this type of materials are reversible by an external electric field loading with some magnitude below the breakdown field of the material. To label a material as a ferroelectric, two conditions are

necessary: (1) the existence of spontaneous polarization and (2) a demonstrated reorienting of the polarization [9].

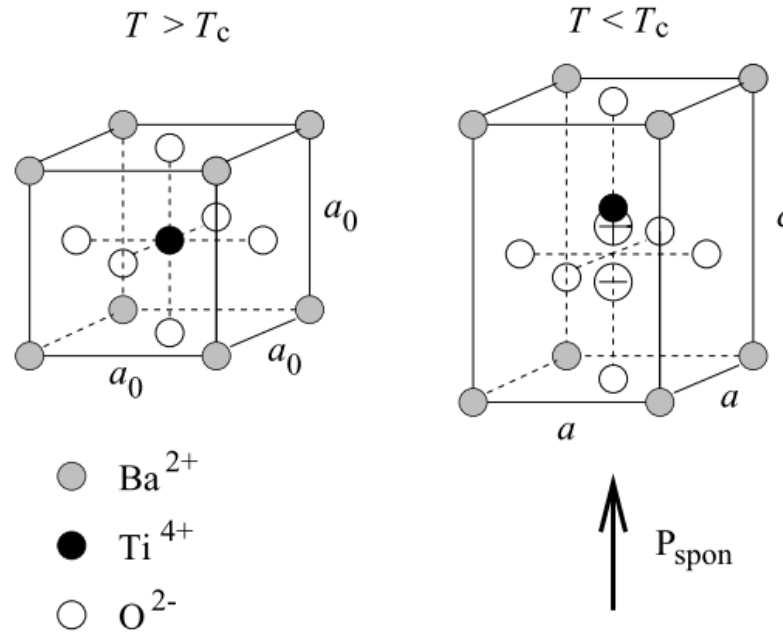


Figure 1.3: Crystal structure of BaTiO₃. Left: Unit cell of BaTiO₃ in the paraelectric phase. The symmetry of cubic shape does not allow for a spontaneous polarization. Right: Unit cell of BaTiO₃ in the ferroelectric phase. The vector of spontaneous polarization P_{spon} is oriented in the direction of the displaced titanium ion (after Ref. [13]).

Figure 1.2 shows the interrelationship of piezoelectric and subgroups on the basis of symmetry. It can be seen that all the ferroelectrics can present piezoelectricity, but not vice versa. Namely, not all the piezoelectrics belong to the group of ferroelectrics. By investigating on BaTiO₃ (BT) ceramics since 1940s [11, 12, 14], the understanding of the nature of ferroelectrics has made huge progresses. The BT ceramic is a prototype ferroelectric material with ABO₃ perovskite structure which provides a good example to explain the spontaneous polarization caused by polar structure.

BaTiO₃ ceramic is cubic when the temperature is higher than a certain degree (which is called Curie temperature, T_c). In this state, the Ba²⁺ are on the A-sites, the Ti⁴⁺ is on the B-site, and O²⁻ are located at the face centers which are shown by Figure 1.3 [13]. Since the center of both positive and negative charges coincide, BaTiO₃ is paraelectric at temperatures beyond the transition temperature $T_c=128$ °C [15]. The unit cell is deformed at a temperature below T_c . An electric dipole is formed due to the separation of positive and negative charge centers, and the dipole moment per unit volume is the spontaneous polarization (P_{spon}) [16].

Homogenous areas with the same P_{spon} orientation are presented as domains. Domain walls separate these regions with different orientations of P_{spon} . There are two types of domain wall in a tetragonal phase ferroelectrics, 180° and 90° domain walls, according to six possible P_{spon} vectors (shown in Figure 1.4). For a ferroelectric state with other symmetry structures of the unit cells, there are additional possible orientations of P_{spon} . Such as in the rhombohedral phase, eight possible orientations of P_{spon} could form 180°, 71° and 109° domain walls [9].

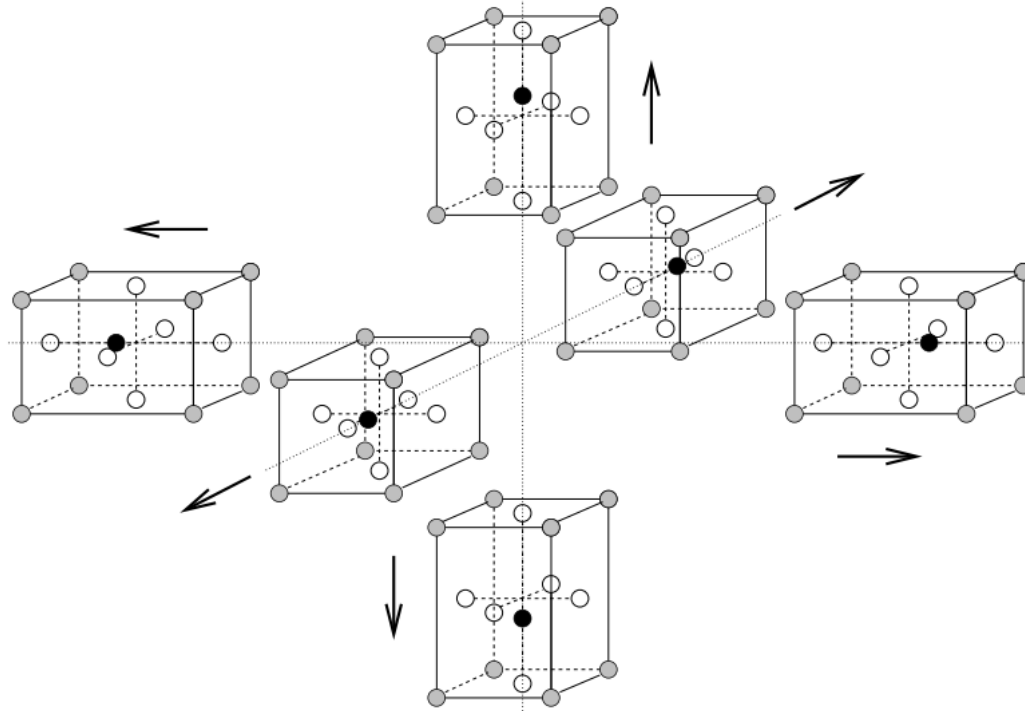


Figure 1.4: At the paraelectric ferroelectric phase transition, six different directions for the central titanium ion to be displaced in a tetragonal structure, resulting in six different spontaneous polarization vectors (after Ref. [13]).

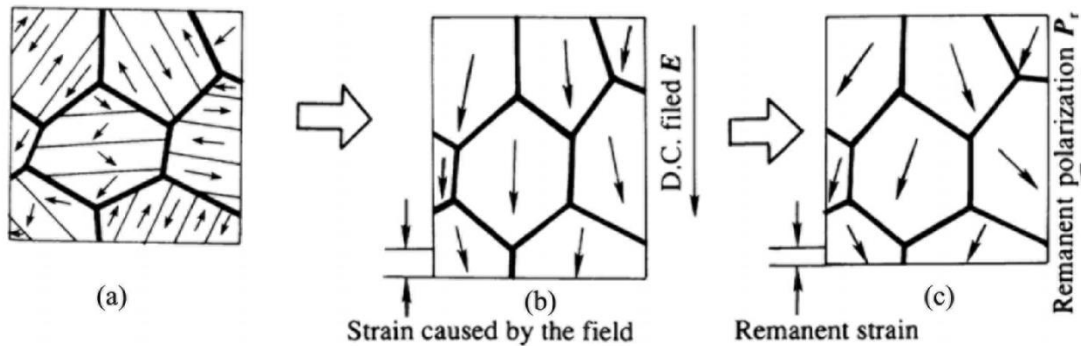


Figure 1.5: Evolution of domain orientation under a poling process (after Ref. [16]).

With the temperature cooling from a sintering temperature (higher than T_c) to the room temperature (below T_c), BaTiO_3 ceramic is a polycrystal with grains and grain boundaries. These grains are split into numerous domains with randomly distributed P_{spont} directions spread in the ceramic material. Therefore, no macroscopic residual polarization is present in this state, unless a poling process is applied under a certain electric field. The Figure 1.5 shows the schematic illustration of the domain orientation and poling process. In the initial state (illustrated in Figure 1.5 (a)), each grain contains domains with randomly distributed P_{spont} . When a sufficient electric field is applied, the initial state can be transformed into a polar state with the domain orientation almost parallel with the external electric field. The polar state is demonstrated in Figure 1.5 (b) where the electric field-induced strain can be observed. The external electric field should be higher than a critical field which is the coercive field (E_c) so that both the 180° and non- 180° domain walls can be reoriented. Remnant polarization (P_r) can be evaluated after removal of the external

electric field which is illuminated in Figure 1.5 (c). Owing to the internal stresses between the grains, some domains turn back to the initial state partly [17]. Therefore, the value of P_r is usually lower than the polarization measured at the maximum electric field used for poling.

Poling process could orient the domains within the grains producing a ceramic material with optimum alignment possessing both ferroelectric and piezoelectric properties. It is identified as the key feature for turning an inert ceramic into an electromechanically active material with a multitude uses [9].

1.1.2 Piezoelectricity in ferroelectric ceramics

As mentioned at the beginning of this chapter, ferroelectric materials are a subgroup of piezoelectric materials. The lead-based and lead-free ceramics used in this work possess both the properties of piezoelectricity and ferroelectricity. Therefore, only piezoelectricity in ferroelectric ceramics is introduced here.

Piezoelectricity is the electric responses under a mechanical pressure. It is defined as electric polarization produced by mechanical load in crystals belonging to certain classes, the polarization being proportional to the load and changing sign with it [18]. This is known as the direct piezoelectric effect. In addition, the converse piezoelectric effect is another side of piezoelectric effect associated with the deformation caused by an external electric field. The direct effect can be understood as a generator which generates electrical changes under a mechanical stress. The converse effect can be compared to a motor to transform the electric stimulation into mechanical movement.

These two effects are described by two basic equations [19, 20]:

$$D_i = d_{ijk}^T T_{jk} + \varepsilon_{ij}^T E_j \quad (\text{Equation 1.1})$$

$$S_{ij} = s_{ijkl}^E T_{kl} + d_{ijk} E_k \quad (\text{Equation 1.2})$$

where D is the dielectric displacement, d is the piezoelectric coefficient, ε is the dielectric constant. E means electric field, S the strain, s the materials compliance, and T is the mechanical stress. The superscripts indicate a constant state. For the ε^T , the mechanical stress is a constant. For the case of s^E , electric field is held constant.

In this thesis, all the experiments were conducted under uniaxial loadings (both the electric field and compressive loadings). Therefore, the external loads are defined in the 3-axis, and the dielectric displacement and strain are measured as:

$$D_3 = d_{33}^T T_3 + \varepsilon_{33}^T E_3 \quad (\text{Equation 1.3})$$

$$S_3 = s_{33}^E T_3 + d_{33} E_3 \quad (\text{Equation 1.4})$$

For most of the piezoceramics, poling is necessary to be able to use their piezoelectric effect which was mentioned previously. However, the non-linear phenomena during this process were not considered. To introduce both the direct and converse piezoelectric effects into the true applications, the non-linear behavior of the dielectric displacement (or polarization when $\varepsilon^T E$ is neglected) or strain caused by domain switching under a large signal stimulation (large electric field or mechanical compressive loadings) should be examined.

1.1.2.1 Ferroelectric domain switching

Electric field induced domain switching is a ferroelectric behavior. A large signal bipolar electric field loading could give rise to a ferroelectric hysteresis loop which is taken as a validation of a ferroelectric material. The typical polarization-electric field (P - E) loops induced by cyclic electric field are illustrated in Figure 1.6 with the number from ① to ⑦ to indicate the domain states. In addition, Figure 1.7 shows the longitudinal strain-electric field (S - E) curves which correspond the domain states shown in Figure 1.6 and Figure 1.7.

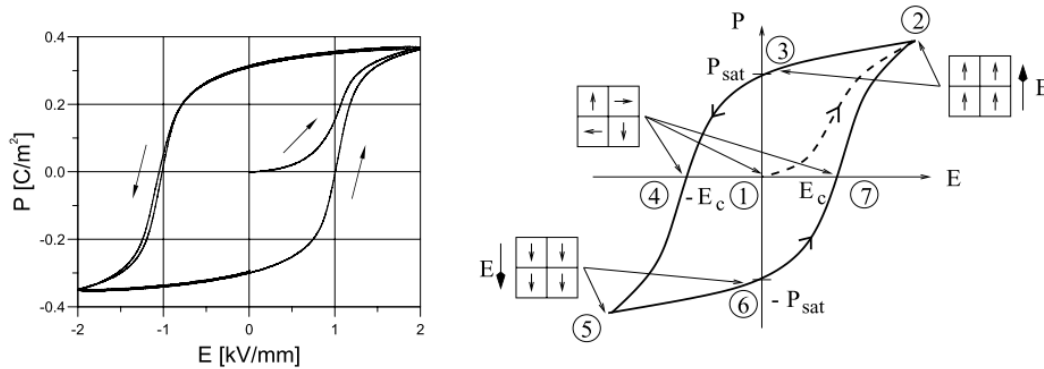


Figure 1.6: Polarization-electric field (P - E) loops of PIC 151 commercial PZT ceramics. ① to ⑦ indicate domain states schematically (after Ref. [13]).

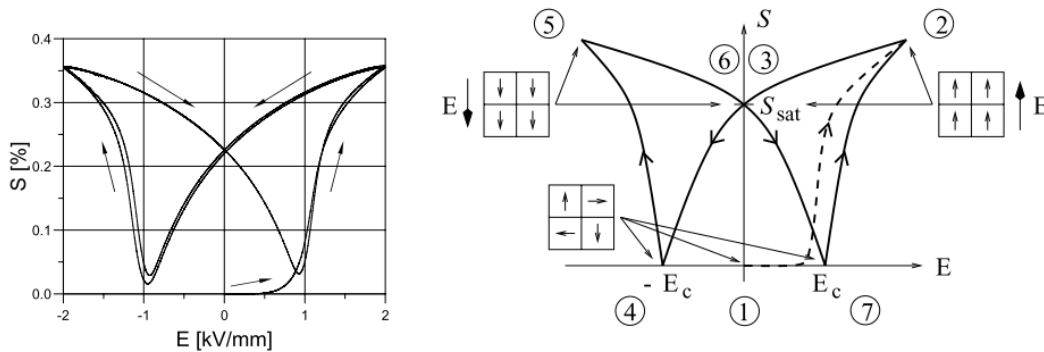


Figure 1.7: Strain-electric field (S - E) butterfly curves of PIC 151 commercial PZT ceramics. ① to ⑦ indicate domain states schematically (after Ref. [13]).

Number ① indicates the initial state of PIC 151 ceramic with domains in this thermally depoled state being randomly distributed in the ceramic. With an increment of the electric field to the coercive field E_c , domains are gradually aligned to the external electric field. When the electric field loading is higher than E_c , the domain switching process is completed with the states indicated by ②. With the electric field unloaded from the maximum value to zero (from state ② to ③), some domains turn back to the initial state partly which was mentioned previously. However, most of the poled domain structures are preserved. The following half cycle of the electric field is controlled at the negative direction. At state ④, the electric field reaches negative coercive field ($-E_c$) with the zero polarization and lowest degree of domain orders during the electric loadings. While the electric field increases from state ④ to ⑤, domains switch to the direction parallel to the negative electric field. The unloading process from ⑤ to ⑥ is similar to the state ② to ③ but the preserved domain structures are paralleled with the direction of the

negative electric field. This is the first cycle of loading on the ceramic, while the following loading will not repeat the path from ① to ② but follow the path of ⑥-⑦-② which shows the symmetry of negative electric loading. The details of domain switching processes under cyclic electric field can be found in some other reports [13, 21, 22].

1.1.2.2 Ferroelastic domain switching

In addition to the external electric fields, a mechanical stress loading can also induce domain switching which is called ferroelastic domain switching. Figure 1.8 shows the schematic demonstration of ferroelastic domain switching where tensile or compressive stress can only induce non-180° domain switching.

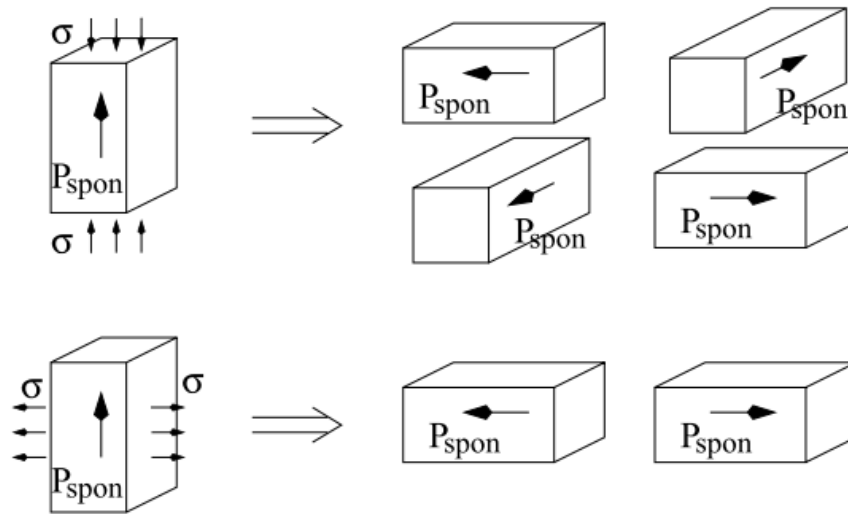


Figure 1.8: A mechanical stress σ of sufficient magnitude induced domain switching (after Ref. [13]).

Figure 1.9 illustrates the depolarization and longitudinal strain curves under a compressive stress for pre-poled PIC 151 PZT ceramics. The discussion on these experimental results can be found in the thesis from D. Zhou [22]. The detailed description of stress-induced domain switching was reported by a review paper from M. Kamlah [13]. The poled state with domains aligned with the direction of the poling electric field is indicated by number ①. Therefore, remnant polarization and longitudinal strain can be read there. At a small value of compressive stress load, the stress-strain curve is nearly linear elastic. Once the mechanical load is higher than a certain value, which is the coercive stress, domain switching is initiated. The polarization vectors in the ceramic distribute randomly in a plane which is perpendicular to the direction of stress loading gradually. This gradually domain switching follows the increment of compressive stress load, so that the non-linearly climbing curve appears. Most of the domains under a sufficient stress can be orientated during this mechanical depolarization process understood by a mechanical stress-induced disarranging of dipoles. It is believed that the ferroelastic domain switching is completed at the state ② due to the sufficiently high stress. During the unloading stage from state ② to state ③, the polarization response does not change much which indicates the electric state relies on the stress state little after the depolarization process. Therefore, the changes of strain state from ② to state ③ is mainly caused by the elastic response.

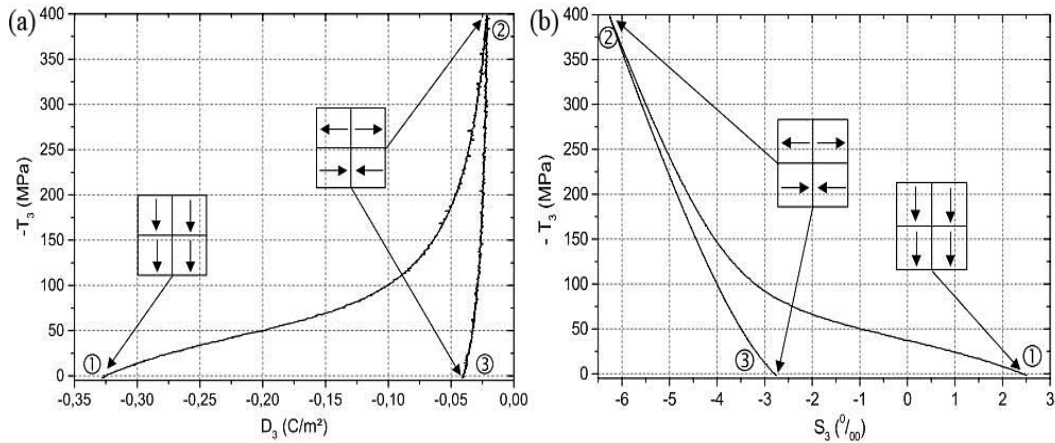


Figure 1.9: Compressive stress induced: (a) depolarization curve and (b) longitudinal strain (after Ref. [22, 23]).

1.2 Lead-based piezoceramics

As mentioned previously, BaTiO_3 (BT) is the first piezoceramic developed for transducer uses in 1940s. After the birth of ABO_3 type of piezoceramics, they are widely used for transducer and actuator applications. However, the application of BaTiO_3 in recent years has shifted away from transducers to an almost exclusive use as high-dielectric-constant capacitors [9].

Compared with the BT ceramic, lead-based piezomaterials were found to be more suitable for transducer and actuator applications. They are the dominant materials in the market for the recent decades owing to their large electromechanical coupling coefficient, high Curie temperature and etc. Various types of piezoceramics focusing on different usages were developed, such as lead lanthanum zirconate titanate (PLZT), lead magnesium niobate (PMN), lead titanate (PT), lead zinc niobate (PZN), lead stannate zirconate titanate (PSZT), lead zirconate (PZ), and so on. Among these lead-based materials, lead zirconate titanate (PZT) solid solution family is the most widely used for a long time. In addition to the properties of large electromechanical coupling coefficient and high T_c mentioned above, PZT also (1) possesses a wide range of dielectric constants; (2) can be poled easily; (3) is relatively easy to sinter at low temperatures; and (4) form solid solutions with many different constituents to tailor a wide range of properties [9].

1.2.1 Ferroelectric and relaxor ferroelectric in lead-based piezoceramics

Relaxor (RE) ferroelectric material is an important subgroup of ferroelectric (FE) materials. They are also dielectrics, crystallizing ABO_3 perovskite structure usually. Although several newly developed lead-free RE ceramic families were reported [8, 24], RE ceramics used in the practical applications successfully are still lead-based materials.

Single crystal $\text{Pb}(\text{Mg}_{1/3}\text{Nb}_{2/3})\text{O}_3$ (PMN) was the first studied RE material in the early 1960s [26], then the PZ-PT-PMN ternary system was investigated [27]. Further work on preparing PMN-based RE ceramics with high strain response (0.1%) were reported in the early 1980s [28, 29]. Since then, many types of lead-based relaxors have been developed and improved for transducer and capacitor applications due to the excellent piezoelectric and dielectric properties [30].

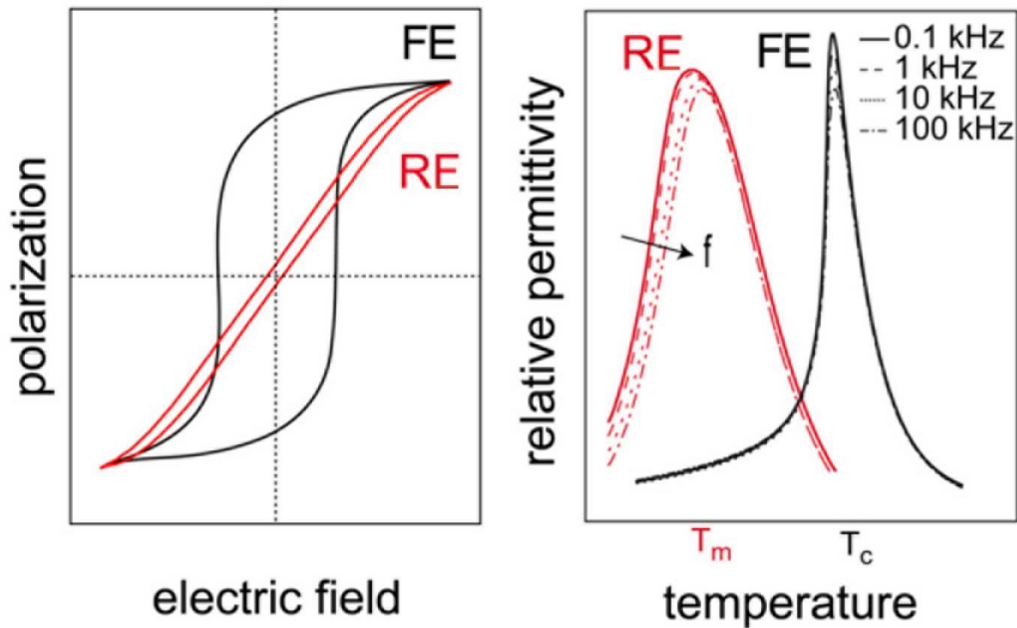


Figure 1.10: Comparison of ferroelectrics and relaxor ferroelectrics in terms of polarization (left), and relative permittivity (right) (after Ref. [25]).

Figure 1.10 illustrates the comparison between ferroelectrics and relaxor ferroelectrics in terms of polarization and relative permittivity. In contrast to the typical P - E hysteresis loop measured from conventional FE, the P - E loop of RE may remain slim with little remnant polarization and a small “coercive field” [31]. In the right side of Figure 1.10, the normal FE shows a sharp, well defined para-to-ferroelectric phase transition at the Curie temperature T_c . In contrast, RE possesses a broad and frequency (f) dispersive maximum of the dielectric permittivity (ϵ) as a function of temperature. T_m is indicated as the temperature of the maximum dielectric permittivity which is frequency dependent. This diffusive characteristic of the dielectric permittivity is one of the features of RE behavior.

The transition of microstructure of RE induced by temperature has been investigated to understand the mechanism of the RE behavior, which is summarized by some review articles [25, 32-34]. From a paraelectric (PE) state at a relatively high temperature, RE undergoes a sequence of structural transformations on cooling. Burns temperature (T_B) is well above the T_m where the maximum dielectric permittivity can be obtained. At T_B , dynamic polar clusters nucleate [35]. At the intermediate temperature T^* , polar nanoregions (PNRs) with slower dynamics are formed from these polar clusters [36, 37]. As the temperature cools below T_m , the PNRs can evolve into normal ferroelectric domains with a very weak ferroic distortion of the unit cell or the PNRs can become static at the Vogel-Fulcher freezing temperature (T_f) [32, 38]. Although the existence of PNRs has been validated by experimental methods [39-41], the reason for the existence of PNRs in RE is still under discussion.

1.2.2 Lead zirconate titanate (PZT) applied on actuators

RE ferroelectrics such as PMN-based single crystals with excellent dielectric and piezoelectric properties are ideal materials for actuator application [42]. However, both PMN-based single crystals and ceramics are somewhat difficult to prepare compared with the conventional PZT ceramics which are widely used despite the fact that REs show about four to ten times larger the d_{33} coefficients. In addition, there are still some disadvantages on these REs, such as relatively low T_c and low E_c which cause a loss of piezoelectric

performance easily compared with PZT [30]. For the PZT material, it has been the dominant piezoceramic for decades and used widely in the areas of piezoelectric fuel injection, motors, printing machines, piezoelectrically controlled thread guides, micro-positioning systems, displacement sensor and many others [43-45]. In this section, only one of these applications, namely, PZT used for piezoelectric actuators will be focused on.

1.2.2.1 Properties required for piezoceramic actuators

Piezoceramic actuators require high strain output with high force generally. The details in this application are given in the following. These requirements of system properties on the PZT material are listed here because it is still the most widely used material in this application. In fact, most of these required properties are also applicable to other materials, such as lead-free piezoelectric ceramics.

(1) d_{33} value. There are two types of d_{33} . The value of d_{33} under a small signal exhibits the degree of intrinsic piezoresponse, which is used to evaluate the capability for non-resonance sensing and energy harvesting application. For actuator application, the large signal piezoelectric coefficient (d_{33}^* , S_{\max}/E_{\max}) is a more important factor to quantify the obtainable strain because actuators are designed for maximum strain under maximum coaxial electric field usually. (2) Low hysteresis under unipolar electric field. Owing to the existence of extrinsic response, the strain response under large signal cyclic electric fields shows nonlinear behavior. For the actuator used in a high-precision positioning system, strong hysteresis should be avoided. (3) Capability of against the external compressive stress. This capability should be considered because strain needs to be provided against a certain mechanical load in many actuator applications. For instance, a small compressive stress of 10-20 MPa is always required to minimize the tendency to cracking at electrode edges. Therefore, the blocking force is used to assess this mechanical capability of an actuator. This force is defined as the uniaxial force on an actuator, which can be applied to exactly compensate for the electric field-induced extension [8]. (4) Temperature dependence. Piezoelectric actuators are required to keep the operational capability in a range of temperature with less temperature dependence. Therefore, investigations on temperature dependence of the properties are important. (5) Cycle dependence, which includes electrical cycles, thermal cycles and mechanical load cycles. The actuators long-term stability is of paramount importance to ensure reliable device operation [46]. Consequently, all these factors influencing the properties of the actuators should be taken into account.

1.2.2.2 PZT ceramics

PZT is the abbreviation for the solid solution of lead zirconate titanate $x\text{PbZrO}_3-(1-x)\text{PbTiO}_3$ ($0 < x < 1$) binary system. Its chemical formula is $\text{Pb}(\text{Zr}_{1-x}\text{Ti}_x)\text{O}_3$. Commonly, this material is prepared with a composition close to the morphotropic phase boundary (MPB; a phase boundary, where a change of composition only changes the phase) around $x=0.48$ [8], where properties such as dielectric permittivity, coupling factor and piezoelectric coefficient reach the maximums [19, 44]. It should be noticed that, in addition to PZT, many useful piezoelectric materials display a similar transition region in their composition phase diagrams, as known MPB [47]. As a result, modern piezoelectric materials for technological applications are usually complex, engineered, solid solutions, which are designed to keep composition close to “MPB” to obtain the high-performances. This idea is not limited to enhance the piezoelectricity of lead-based materials but also has been extended to lead-free piezoelectric ceramics [48].

Some attractive features of PZT ceramics to achieve the application of actuators were summarized by Rödel *et al.* [8] as following. (1) It possesses a proper coercive field of about 1 kV/mm and a remnant polarization of about $35 \mu\text{C}/\text{cm}^2$. Therefore, the poling field is a much lower than the dielectric breakdown strength. (2) Relatively high strain responses (0.1%-0.2%) at a unipolar electric field range from 0 to 2-3 kV/mm. To generate such high fields on a typical stack actuator with layer thickness of 80 μm , a

potential of about 200 V is sufficient. (3) A large signal piezoelectric coefficient as large as 779 pm/V has been reported for doped PZT [50]. (4) High Curie temperature of 300-400 °C. A *in situ* hot-stage experiment shows that some nanodomains in PZT can still be observed even at 300 °C [51]. Besides, PZT with high T_c can also provide reliable strain response up to 175 °C with little temperature dependence [52]. (5) Various properties can be achieved by doping additives. The effects of additives on properties of PZT are listed in Table 1.1, where three types of additives are summarized.

Table 1.1: Effects of typical additives on properties PZT. Ionic radii in nanometer are given in parentheses [16, 22, 49]

Additives	Effects
Isovalent additives: Ba^{2+} (0.134) or Sr^{2+} (0.112) for Pb^{2+} (0.132) Sn^{4+} (0.071) for Zr^{4+} (0.079) or Ti^{4+} (0.068)	Lower Curie point Higher permittivity
Soft dopants (donors): La^{3+} (0.122), Nd^{3+} (0.115), Sb^{3+} (0.090), Bi^{3+} (0.114) or Th^{4+} (0.110) for Pb^{2+} (0.132) Nb^{5+} (0.069), Ta^{5+} (0.068), Sb^{5+} (0.063) or W^{6+} (0.065) for Ti^{4+} (0.068) or Zr^{4+} (0.079)	Make the material “soft”: Higher permittivity Higher K_p Much lower Q_m Resistivity about 10^3 higher
Hard dopants (acceptors): K^+ (0.133) or Na^+ (0.094) for Pb^{2+} (0.132) Fe^{3+} (0.067), Al^{3+} (0.057), Sc^{3+} (0.083), In^{3+} (0.092) or Cr^{3+} (0.064) for Ti^{4+} (0.068) or Zr^{4+} (0.079)	Make the material “hard”: Lower permittivity Lower dielectric loss Lower K_p Much higher Q_m

1.3 Lead-free piezoceramics

In this section, information is based on several review papers by Rödel *et al.* [8, 53], Jo *et al.* [54], Aksel and Jones [55], and Shrout and Zhang [56].

The lead-based piezoceramics have been successfully used in various applications. However, typical lead-based piezoceramic such as PZT ceramic contains more than 60 weight percent lead, which has been used in lots of electronic devices with attendant problems of recycling and waste disposal after their usage. Environmental concerns over their lead content could disappear with the advent of a new ceramic that is lead-free [57]. Lead-free ceramics have been reported to offer comparable properties to that of PZT in some fields, making them viable candidates for various applications [56]. To date, finding a single lead-free material or a family of lead-free solid solutions to replace PZT ceramics completely is still a hard

work. The following introduction in this section is focused on the lead-free piezoceramics related the experimental work in this thesis. These lead-free ceramics can be categorized into three groups according to the compositions: one component system, binary solid solution and ternary solid solution.

1.3.1 Three base-systems: Barium Titanate (BT), Potassium Sodium Niobate (KNN) and Sodium Bismuth Titanate (NBT)

In spite of the majority of choices in the periodic table of elements, not many systems other than three base-systems, i.e., BaTiO_3 (BT), $\text{Na}_{1/2}\text{Bi}_{1/2}\text{TiO}_3$ (NBT) and $(\text{K}_{0.5}\text{Na}_{0.5})\text{NbO}_3$ (KNN) have been deemed competitive [8, 54].

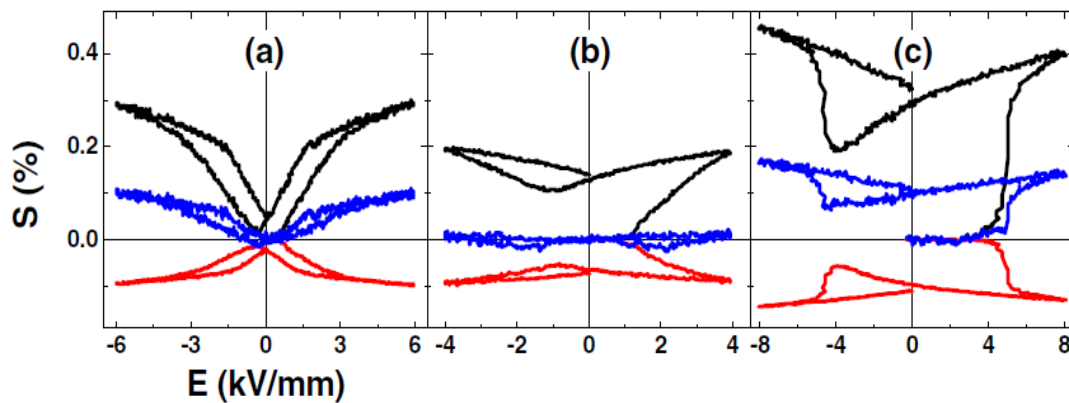


Figure 1.11: Electric field-induced strains (black curves, longitudinal strains; red curves, transverse strains) at room temperature of (a) pure BT, (b) pure KNN, and (c) pure NBT with the associated volume change (blue curves), measured during bipolar poling cycle at 50 mHz (after Ref. [54]).

Barium Titanate - BaTiO_3 (BT) is one of the representative lead-free materials. It serves as a model system for more fundamental investigations [58, 59]. In Figure 1.11(a), BT shows a large strain with a relatively small hysteresis. The large signal d_{33}^* or normalized strain $S_{\text{max}}/E_{\text{max}}$ (the ratio of maximum strain S_{max} to maximum external electric field E_{max}) is as large as 594 pm/V when an electric field of 2.6 kV/mm is applied, indicating why enhanced piezoelectric properties can be obtained in its derivative compositions [6]. Its relatively low T_c limits the practical application. However, it has been used in other solid solutions to form an MPB where the electric properties get enhanced.

Sodium Potassium Niobate - $\text{K}_{0.5}\text{Na}_{0.5}\text{NbO}_3$ (KNN) is a composition (50:50) of a complete solid solution of NaNbO_3 and KNbO_3 . It exhibits a composition with two orthorhombic phases around MPB where NaNbO_3 is antiferroelectric (AFE) and KNbO_3 is ferroelectric (FE) [60, 61]. Sintering is one of the most challenging steps in processing KNN ceramics owing to the high volatility of the alkaline at the temperature around solidus line [62]. The KNN ceramic prepared by conventional methods only exhibits a d_{33} around 90 pC/N [63], which is lower than the dense ceramic with d_{33} of 148 pC/N processed by spark plasma sintering (SPS) method [64]. In Figure 1.11(b), the KNN ceramic shows a relatively small poling strain of $\sim 0.19\%$ at 4 kV/mm. For the normalized strain $S_{\text{max}}/E_{\text{max}}$ under unipolar loading, the value of that reaches only 150 pm/V which limits the applications of pure KNN ceramic.

Sodium Bismuth Titanate - $\text{Na}_{1/2}\text{Bi}_{1/2}\text{TiO}_3$ (NBT) was first reported by Smolenskii *et al.* in 1960s [65]. It is also written as $\text{Bi}_{1/2}\text{Na}_{1/2}\text{TiO}_3$ (BNT) by many reports [4, 48, 66]. In this thesis, NBT rather than BNT is used to follow the order of electronegativity of the elements.

Similar to the pure KNN, NBT was not received many attention until recent decades when lead-free piezomaterials are considered to be a replacement of PZT. In 1990s, some initial properties were provided by some measurements [67-69]. Jones and Thomas reported that NBT possesses the rhombohedral $R3c$ space group at room temperature and changes to tetragonal and subsequently cubic during heating [70]. A systematic investigation on NBT ceramic was given by Hiruma *et al.* [71] where its electrical properties and thermal depoling process were reported. However, some main drawbacks were also found which are high coercive field and high conductivity. In addition, the depolarization temperature of 187 °C is much lower than the T_c of 325 °C [71]. Figure 1.11(c) demonstrates the S - E curve where the strain is $\sim 0.4\%$ at 8 kV/mm. Eliminating the large remnant strain of $\sim 0.23\%$, the value of S_{\max}/E_{\max} in the unipolar electric field loading is only ~ 213 pm/V. The coercive field in Figure 1.11(c) of about 4 kV/mm indicates that this material needs a large driving field if it would be used as an actuator.

1.3.2 NBT-BT binary solid solution

BT was added into NBT to form a new solid solution $(1-x)(\text{Na}_{1/2}\text{Bi}_{1/2})\text{TiO}_3$ - $x\text{BaTiO}_3$ (NBT-BT) which was reported first in 1991 [48]. In that paper, an MPB was found at 6-7% BT between NBT (rhombohedral) and BT (tetragonal) phases. The MPB is known to be one of the key features in enhancing electro-mechanical properties of piezoelectrics. Therefore, the $0.94(\text{Na}_{1/2}\text{Bi}_{1/2})\text{TiO}_3$ - 0.06BaTiO_3 (NBT-6BT) and $0.93(\text{Na}_{1/2}\text{Bi}_{1/2})\text{TiO}_3$ - 0.07BaTiO_3 (NBT-7BT) in the NBT-BT system raised lots of attention [72-74]. NBT-6BT exhibits enhanced properties compared to pure NBT, such as a higher d_{33} (125 pC/N), electro-mechanical coupling factor ($k_{33} > 50\%$), along with a high bending strength (~ 200 MPa) [48]. The S_{\max}/E_{\max} reaches ~ 700 pm/V at the electric field of 6 kV/mm [75] (observed in the first half cycle of bipolar electric field loadings). Dittmer *et al.* [76] reported the blocking stress of NBT-6BT is -39 MPa and -102 MPa measured at room temperature and 125 °C, respectively. All those properties make the NBT-BT a promising candidate for lead-free actuation applications.

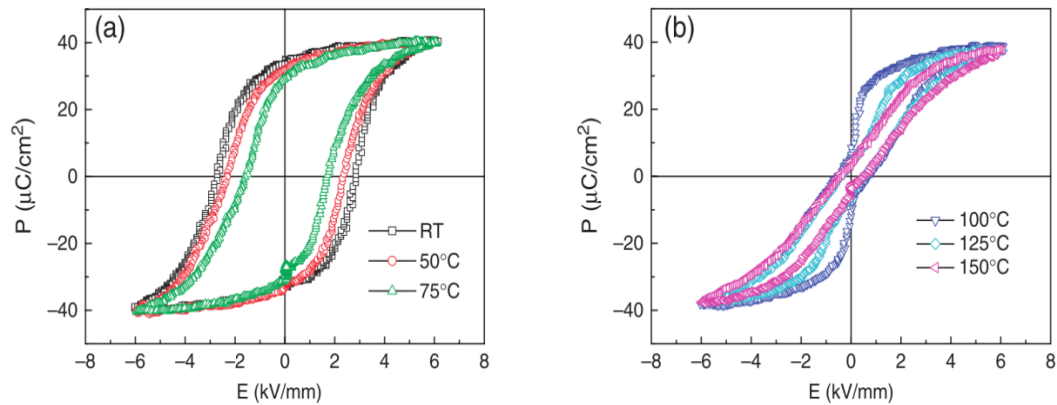


Figure 1.12: Temperature dependent P - E loops of NBT-6BT ceramic (after Ref. [77]).

In order to figure out the correlation between the structure and the electrical properties, efforts have been focused on the structural evolution. The structure of the NBT-BT system depending on composition and temperature was shown by several phase diagrams [78-80]. In the virgin state at room temperature, $(1-x)\text{NBT}$ - $x\text{BT}$ is in the tetragonal $P4mm$ ferroelectric phase (FE) when $x \geq 0.1$. As x decreases, NBT-BT is in the tetragonal $P4bm$ relaxor phase (RE) for $0.05 \leq x \leq 0.11$, and in the rhombohedral $R3c$ FE phase for $x \leq 0.06$. However, the most noticeable drawback of this system at the MPB ($x=0.06\sim 0.07$) is the relatively low T_c around 120 °C. In addition, depolarization happens at ~ 100 °C which is much lower than T_m

(~300 °C) [81-83]. This thermal depolarization could limit this material to be used at a higher working temperature. Zhang *et al.* investigated the temperature-dependent electrical properties of NBT-6BT [77]. As shown in Figure 1.12 and Figure 1.13, typical *P-E* loops and butterfly bipolar *S-E* curves can be observed below 100 °C. These were attributed to the rhombohedral-tetragonal MPB composition showing dominant ferroelectric order. When the temperature reaches 100 °C or even higher, pinched *P-E* loops and sprout-shaped *S-E* curves were found. It was interpreted as a temperature-induced transition from ferroelectric (FE) state to antiferroelectric (AFE) state [77], which is understood as the FE state was transformed to relaxor (RE) state recently [84].

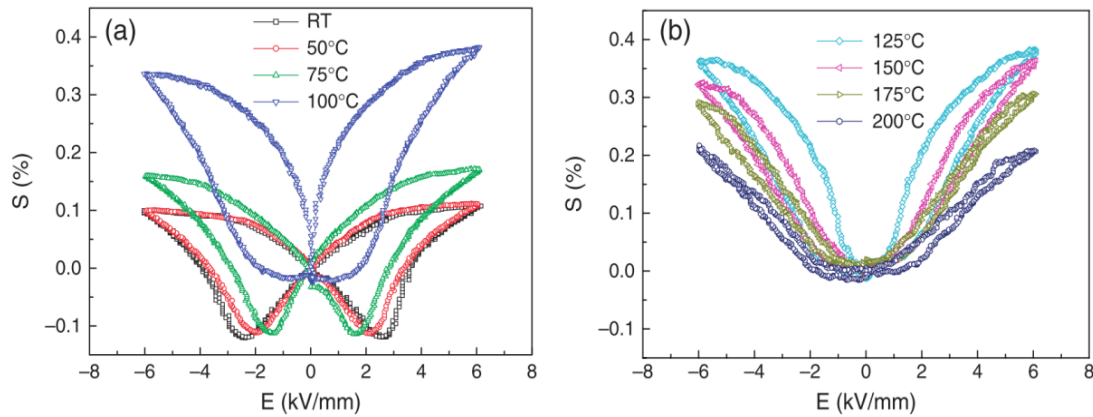


Figure 1.13: Temperature dependent *S-E* loops of NBT-6BT ceramic (after Ref. [77]).

1.3.3 NBT-BT-KNN ternary solid solution

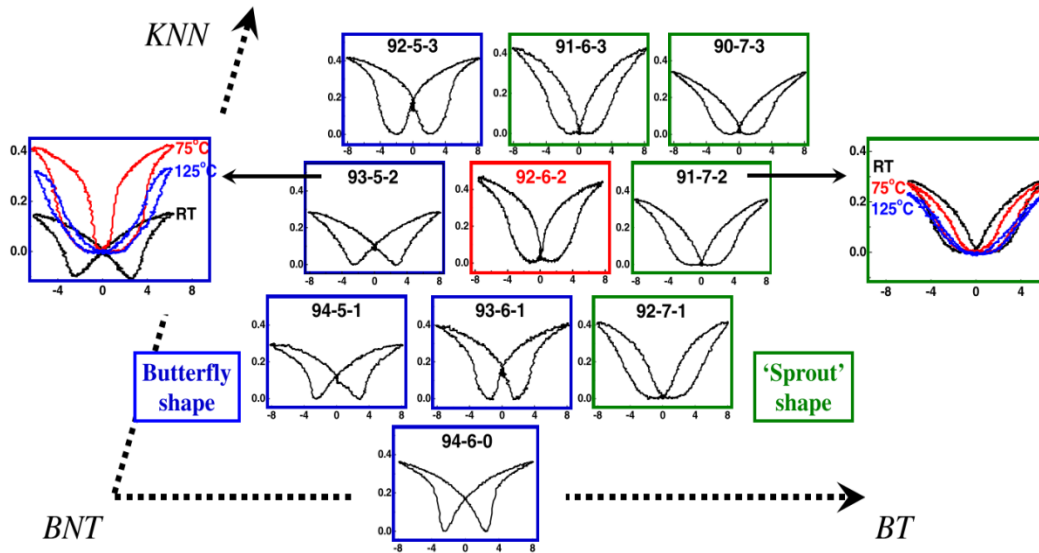


Figure 1.14: Bipolar strain hysteresis of NBT-BT-KNN system near the composition 0.94NBT-0.06BT (after Ref. [54]).

As the NBT-BT binary system described above still has some drawbacks, a more complex lead-free solid solution family has been developed through modifying NBT-BT by KNN. $(0.94-x)(\text{Na}_{1/2}\text{Bi}_{1/2})\text{TiO}_3-0.06\text{BaTiO}_3-x\text{K}_{0.5}\text{Na}_{0.5}\text{NbO}_3$ exhibiting giant electric field-induced strain was reported by Zhang *et al.*

[85]. In that report, 0.92NBT-0.06BT-0.02KNN (NBT-6BT-2KNN) showed a very large S_{\max}/E_{\max} of 560 pm/V ($\sim 0.45\%$ at 8 kV/mm), which was the largest electric field-induced strain ever reported for polycrystalline lead-free ceramics [85]. The subsequent investigations indicated that the electromechanical behavior of the $(1-x-y)\text{Na}_{1/2}\text{Bi}_{1/2}\text{TiO}_3-x\text{BaTiO}_3-y\text{K}_{0.5}\text{Na}_{0.5}\text{NbO}_3$ ($0.05 \leq x \leq 0.07$ and $0.01 \leq y \leq 0.03$) system at room temperature depends both on composition [75] and temperature [86]. Taking into account these experimental data, a phase diagram can be obtained [87]. In Figure 1.14, the maximum electric field-induced strain was observed at $x=0.06$ and $y=0.02$ (NBT-6BT-2KNN) where butterfly-shaped S - E loops indicative of dominant ferroelectric order change to sprout-shaped curves. Dittmer *et al.* reported that by varying the KNN-content in NBT-6BT from 0 to 18 mol.% the macroscopic large-field properties are drastically altered from a ferroelectric characteristic to a relaxor behavior [4]. As shown in Figure 1.14 (left and right figures), the temperature-dependent hysteresis loops of the selected compositions also demonstrate that the phase transition can be induced by changing temperatures in a given composition.

1.3.4 Electric field-induced ergodic and nonergodic behavior in NBT-based ceramics

Phase transitions depending on composition and temperature were introduced briefly in the previous two sections. Furthermore, external electric field is another factor to induce a phase transition in the NBT-BT and NBT-BT-KNN systems.

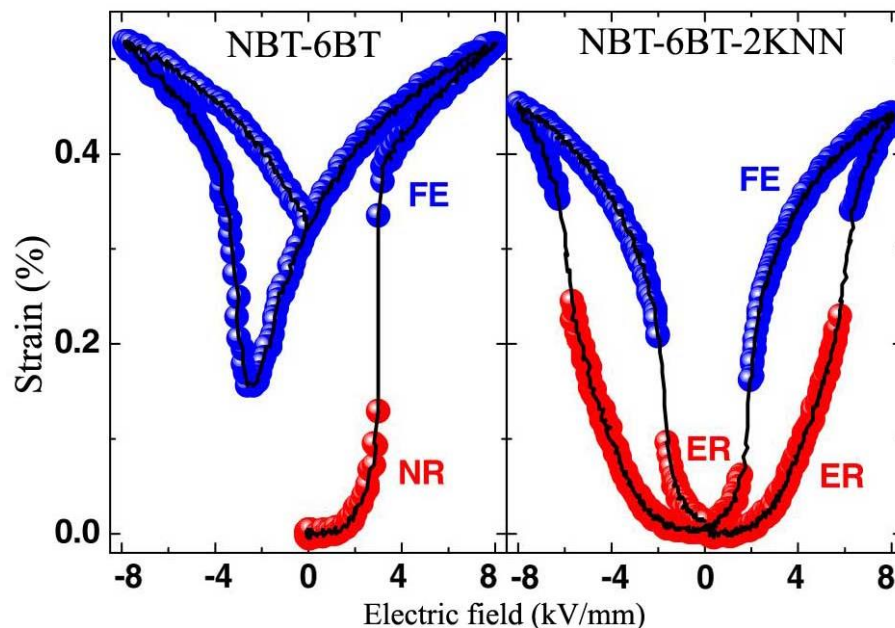


Figure 1.15: The nature of the electric field-induced phase transition observed in NBT-6BT (left) and NBT-6BT-2KNN (right). FE, NR and ER denote ferroelectric, non-ergodic relaxor and ergodic relaxor phase, respectively (after Ref. [54]).

Figure 1.15 demonstrates the nature of the electric field-induced phase transition in two representative ceramics: NBT-6BT and NBT-6BT-2KNN. W. Jo *et al.* summarized that both the two materials had been conventionally considered as normal ferroelectric phases, but actually they are both relaxors as long as no external electric field is applied [54]. This argument was supported by a series of experiments under varying temperatures [88-91]. Several review articles provide the contemporary understanding of relaxor ferroelectrics [25, 32, 33, 92]. According to the current contributions, there are two different states of

relaxors: one transforms from RE into FE irreversibly (non-ergodic relaxor, NR) and the other one does reversibly (ergodic relaxor, ER). In Figure 1.15, NBT-6BT transforms from NR into FE irreversibly upon a sufficiently large loading of electric field [93]. This transition cannot be reversed by removing the external electric field easily unless by temperature high enough (higher than depolarization temperature) to break the long-range ferroelectric phase. Both T_d (depolarization temperature) and T_{F-R} (ferroelectric-to-relaxor transition temperature) can be reduced by adding KNN into the NBT-BT system. Therefore, the electric field-induced phase transition is a reversible behavior at room temperature when the T_{F-R} is slightly below room temperature [91]. NBT-6BT-2KNN transformed from ER into FE reversibly under a sufficient electric field as shown in the right figure of Figure 1.15.

This electric field-induced phase transition influences the electromechanical properties of a lead-free ceramic strongly, resulting in much attention on the investigation of the structural changes. For the NBT-BT binary system, the conventional phase diagrams cannot provide the information of electric field-induced structural changes, so *in situ* techniques were employed to monitor the phase evolution under an electric field load recently. High energy X-ray scattering experiments indicate that, the electric field-induced strain of $0.93(\text{Na}_{1/2}\text{Bi}_{1/2})\text{TiO}_3\text{-}0.07\text{BaTiO}_3$ (NBT-7BT) polycrystalline ceramic is the result of the phase transformation from a pseudocubic to a tetragonal symmetry [94]. However, the X-ray diffraction experiment did not provide enough resolution to explore the structure around the MPB composition ($x=0.06\sim 0.07$). An *in situ* synchrotron diffraction experiment was conducted by W. Jo *et al.* [72]. The MPB between a rhombohedral and a tetragonal phase evolved into a morphotropic phase region under an electric field. In this region, the phase composition in NBT-BT changes from the unpoled to the poled state. In the unpoled state, the transition happens from the space group $R3c$ to $R3m$ ($x=0.05$) and from $R3m$ to $P4mm$ ($x=0.11$). The maximum permittivity is obtained in the single-phase $R3m$ compositions between NBT-5BT and NBT-11BT. While in the poled material (at 6 kV/mm), a clear maximum in the piezoelectric coefficient occurs at BNT-7BT. Unlike X-ray or neutron diffraction which obtains average structural information on materials, *in situ* transmission electron microscopy (TEM) can provide precise resolution to visualize the real-time domain morphology changes under an electric field [80]. By using this method, C. Ma *et al.* [95] proposed an electric field vs. composition phase diagram for the NBT-BT system. For unpoled NBT-7BT, $P4bm$ RE nanodomains irreversibly transform partially to $P4mm$ FE lamellar domains as the electric field is loaded from 0 to 2.5 kV/mm. With further increasing of the electric field, the RE phase vanishes but the new $P4mm$ -to- $R3c$ (FE to FE) transition can be observed. M. Hinterstein *et al.* [96] reported that NBT-7BT has a pseudocubic structure with almost no observable lattice distortion in the unpoled state. Under the influence of an applied electric field (4 kV/mm), the initial pseudocubic structure transforms to a phase coexistence of a weak rhombohedral distortion and a strong tetragonal distortion.

For the NBT-BT-KNN ternary solid solutions, the large strain is understood to be due to a reversible electric field-induced transformation between a macroscopic non-polar state (ER phase) and a macroscopic polar state (FE) [97]. In the non-polar state at room temperature, NBT-6BT-3KNN is lacking a long-range ferroelectric order. High resolution transmission electron microscopy (HRTEM) studies have shown a lack of ferroelectric domains in this state, marked by a “grainy contrast” [98-100]. Following the application of an external electric field there is the development of domains, understood to be a long-range ferroelectric order. In-situ high energy synchrotron diffraction studies have revealed a corresponding transition from a pseudo-cubic phase to tetragonal, rhombohedral, or mixed tetragonal/rhombohedral phase depending on composition [101, 102]. Piezoresponse force microscopy (PFM) was used to provide nanoscale electromechanical behavior of NBT-BT-KNN ceramics [4]. This investigation reveals that the addition of KNN (from 0 to 18 mol.%) increases the threshold field required to induce long range order and decreases the stability thereof. For NBT-6BT-3KNN, the field-induced domains relax completely, which is also reflected in zero macroscopic remanence. Eventually, no long range order can be induced for the content of KNN being higher than 3 mol.%.

1.3.5 Improvements on lead-free ceramics for actuator applications

As mentioned at the beginning of this thesis, lead-free piezoceramics have appeared adequate in specific but narrow applications. They are not yet suited to replace PZT on a broader basis [8]. To enhance the electromechanical response, two main strategies are adopted commonly: composition engineering and structure engineering [103]. The former includes: searching for morphotropic phase boundary (MPB), polymorphic phase boundary (PPB, a boundary occurring as a consequence of a change in thermodynamic variables and at constant chemical composition [103]), tricritical point and doping. Structure engineering can be achieved by grain engineering, domain engineering, texturing and designing heterogeneous materials. In this section, the introduction focuses on developing new solid solutions and ceramic/ceramic composites for actuator uses briefly (especially on NBT-based materials), instead of following the details of those two strategies listed above.

1.3.5.1 Developing new solid solutions

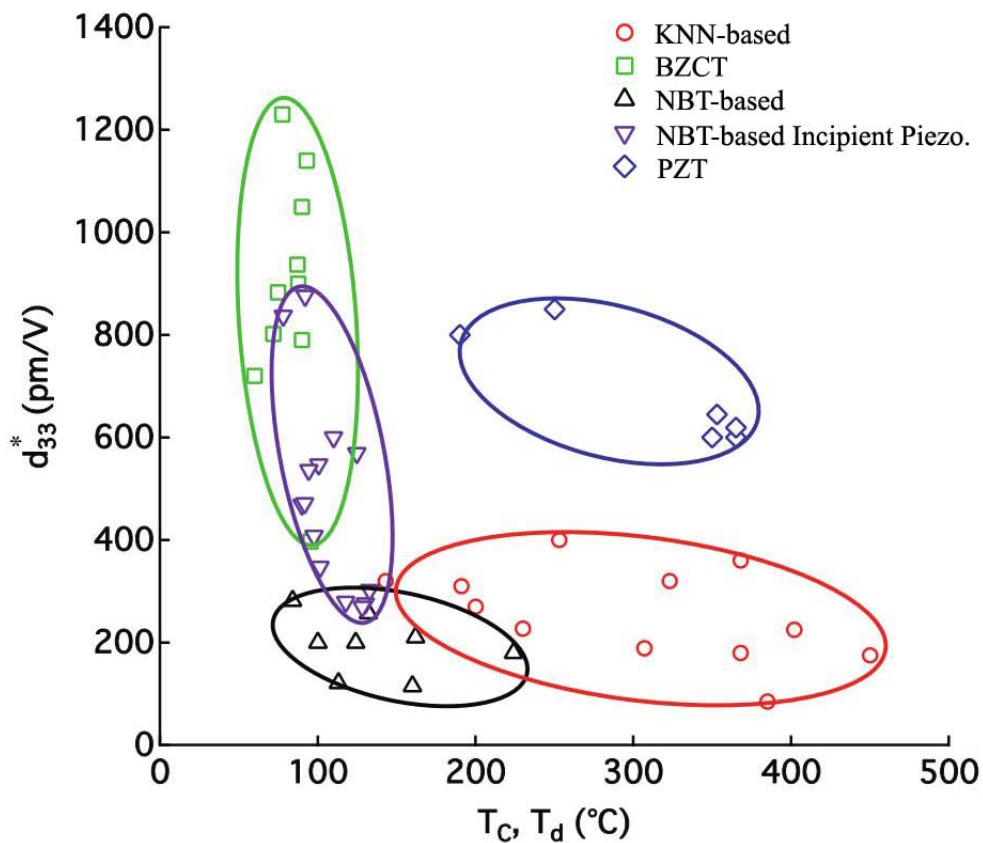


Figure 1.16: The large signal piezoelectric coefficient as a function of depolarization temperature for KNN-based [7, 56, 104-106], BCZT [6, 107-110], NBT-based [56, 77, 88, 111, 112], NBT-based Incipient piezoelectrics [75, 86, 113-117] and PZT [56, 118, 119]. It should be noticed that the maximum electric field is not always the same level for each data point (after Ref. [53]).

For the actuator application, the large signal piezoelectric coefficient (d_{33}^*) under various temperatures is particularly useful in characterizing the actuating performance of piezoelectric ceramics. Therefore, numerous efforts have been made in developing new lead-free solid solutions with high values of d_{33}^* . Figure 1.16 demonstrates the large signal piezoelectric coefficient of several representative ceramics as a

function of Curie temperature or depolarization temperature: KNN-based, (Ba,Ca)(Ti,Zr)O₃ (BCZT), NBT-based, NBT-based incipient piezoelectrics and PZT. Jo *et al.* [54] and Dittmer *et al.* [120] explained the term “incipient piezoelectrics” which is the class of materials with initially small piezoelectricity beginning to develop under the application of external electric field.

The passion of developing KNN-based lead-free ceramics was fueled by a publication by Saito *et al.* in 2004 [7]. This work found a mixture of morphotropic and polymorphic phase transition region in KNN-based family with d_{33} values close to PZT in the textured ceramics. Following this work, the KNN-based system was widely investigated by other works [63, 104-106] (also see KNN-based piezoelectrics in Figure 1.16). This system is not only featured by its relatively large d_{33} , but also its thermal stability [121, 122]. In Figure 1.16, the KNN-based piezoelectrics show the highest T_d among these five systems, making this family of materials be adapted for high temperature applications.

Ba(Zr_{0.2}Ti_{0.8})O_{3-x}(Ba_{0.7}Ca_{0.3})TiO₃ (BZT-xBCT or BCZT) piezoceramics were reported by Liu and Ren firstly [6]. At the optimal composition around the MPB, this ceramic shows a surprisingly large d_{33} (~620 pC/N) at room temperature. The d_{33}^* values of BCZT solid solutions are provided by Figure 1.16 [6, 107-110]. This system exhibits excellent electromechanical properties which can be used for actuators with usage temperature below 100 °C [53].

In addition to the pure NBT and NBT-BT introduced previously, different dopants were added on the A site of the ABO₃ structure to form various solid solutions. Li⁺ and K⁺ can be co-doped on the Na⁺ site [123, 124]. La³⁺ [125, 126] and Mn³⁺ [127] were also doped to increase the value of d_{33} . By adding ZnO particles into NBT-6BT to form new NBT-6BT: xZnO composites, the thermal stability of these ceramics can be improved significantly [128]. The large signal piezoelectric coefficients as a function of depolarization temperature for both NBT-based [56, 77, 88, 111, 112] and NBT-based incipient piezoelectrics [75, 86, 113-117] are plotted in Figure 1.16.

Beside the materials plotted in Figure 1.16, a non-textured NBT-based lead-free ceramic system ((Bi_{1/2}(Na_{0.84}K_{0.16})_{1/2})_{0.96}Sr_{0.04})(Ti_{1-x}Nb_x)O₃ with complicated compositions was reported by Liu and Tan [129]. When $x=0.025$ (abbreviated as BNT-2.5Nb), this ceramic exhibits giant electric field-induced strain (0.70%) and d_{33}^* (1400 pm/V). The highly textured 0.2(K_{0.5}Bi_{0.5}TiO₃-BaTiO₃)-0.8Na_{0.5}Bi_{0.5}TiO₃ (KBT-BT-NBT) ceramic exhibits both low hysteresis and high temperature stability was reported by D. Maurya *et al.* [130]. It was not marked in Figure 1.16, neither.

1.3.5.2 Designing composite structures

The NBT-based ternary and ternary incipient piezoelectrics have been found to exhibit large electric field-induced strains which were mentioned above. However, these large strains are usually accompanied by a requirement of high poling fields and large strain hysteresis [131]. The design of a relaxor/ferroelectric (RE/FE) composite provides a highly effective way to resolve both the challenges [5].

Shrout *et al.* prepared a PZT-based antiferroelectric/ferroelectric (AFE/FE) composite structure starting this approach to enhancing the electromechanical properties of piezoelectrics [132]. In subsequent works, RE was used to replace the AFE layer obtaining a ceramic-ceramic composite which combined both the advantages of each layer: a large coupling factor from FE and a good thermal stability from RE. The existence of FE in the AFE/FE composite reduced the electric field required to drive the phase transition from the AFE to the FE [133] which can be attributed to internal electric fields simulated by a series capacitor model [134]. This approach is not limited to lead-based piezoelectrics. It can be transferred to other materials to obtain some desired properties, such as dielectric permittivity [135], piezoelectric and pyroelectric properties [136], dielectric tunability [137], etc.. These properties can be achieved by adjusting composition, dopant concentration, and volume fraction of each layer [138].

Owing to their unique core (FE or ergodic RE phase)-shell (non-ergodic RE or paraelectric phase) structure, some KNN-based [139] and NBT-based [140] ceramics exhibit giant strain responses under an electric field loading. These ceramics with core-shell micro structure provided an understanding of the electromechanical behavior in the ceramic/ceramic composite. In this core-shell structure, the FE core facilitates transition of the paraelectric shell into a FE under an external electric field resulting in a reduction of required poling field. Combining the concepts of ceramic/ceramic composite and core-shell structure, Lee *et al* [141] designed a nonergodic RE/FE composite system validating these concepts. Groh *et al.* investigated the NBT-BT-KNN/NBT bilayer composite systematically [5, 84, 142]. In these works, temperature and frequency-dependent properties of this bilayer structure were checked. Besides, an optimized volume fraction of each layer each was found where the electric field-induced strain gets enhanced and reaches the maximum value. The interface of the NBT-7BT and $0.75(\text{Na}_{1/2}\text{Bi}_{1/2})\text{TiO}_3$ - 0.25SrTiO_3 (NBT-25ST) bilayer was investigated by using scanning electron microscope (SEM) and energy dispersive X-ray spectroscopy (EDX) [138]. In this work, the interface region between the two layers was found approximately 10 μm in width. Zhang *et al.* extended the concept of bilayer composites to multilayer structures [143]. Two types of composites with alternating RE and FE layers were prepared, one with the layers parallel and the other with the layers perpendicular to the electrode surfaces. It is found that in addition to polarization coupling, the strain coupling effect also plays a critical role in the reduction of the RE-FE phase transition field.

2 Digital image correlation (DIC) method

Deformation behavior is one of the key issues needs to understand before the materials are used for manufacturing any piezoelectric actuators. In order to investigate the deformation behavior, the powerful technique of digital image correlation (DIC) is introduced here for measuring the strains induced by both electric field and mechanical loading.

2.1 Motivation

DIC method was developed by M. A. Sutton *et al.* in the 1980s [144], when it was called two-dimensional DIC (2D-DIC). It is a non-contact and non-destructive method, was designed to monitor surface deformation of materials [145]. This method is built on comparing two digital images, which are captured from the states before and after the deformation, respectively. The images can be obtained from an optical microscope (OM) [146, 147], a scanning electron microscope (SEM) [148, 149], and even from atomic force microscopy (AFM) [150]. This leads to a wide range of the measurement sensitivity and resolution of DIC depending on the magnification of the observing tools. In particular, it can be used to realize microscale to nanoscale deformation measurement. Compared with other non-contact optical techniques such as the interferometric optical method [151], DIC method does not require any laser source or other expensive devices. Only a digital camera with a suitable lens is needed in order to image an object. A white light source or natural light is required for illumination in both laboratory and field applications, respectively.

Compared with the DIC method, strain gauge is a typical measurement device which touches the surfaces of samples directly [152]. Upon deformation, the gauge bonded on a surface will record the strain of the sample. But the information collected from the area of a surface where the strain gauge is bonded only contains strain in a single direction, may it be either longitudinal or transverse. To measure both, another gauge is needed [153]. This method, on the one hand, gives an average value of the area the strain gauge is attached to, but, on the other hand, only of this area. Besides that, strain gauges have to be glued solidly on the surfaces of the samples. This procedure needs to be repeated for each specimen, raising issues with respect to the reproducibility of the gluing. Another direct measurement device for deformation is a linear variable displacement transducer (LVDT) [52, 154]. When it is in contact with a surface of the sample, the motion of the LVDT sensor tip will be recorded while the deformation happens. For one thing, in many cases surfaces of interest are not accessible for placing a LVDT on them. For another, only the deformation in direction of the axis of the LVDT is recorded which, in addition, will be affected by a possible rigid body motion of the sample. Finally, the displacement of a surface cannot tell us any information about the homogeneity of the strains in a sample.

Due to the disadvantages of the traditional paths mentioned above, DIC method has attracted many attentions since it was developed. This method is not just designed for measuring longitudinal and transverse strains, but also can be applied for measuring shear strain [155]. Furthermore, full-field strain distribution can be obtained by using this providing more information about the deformation. Therefore, it has been used extensively for different types of loading: compression [156], tensile loading [157], bending [158], thermal shock [159, 160], etc., and various materials: metals [148], plastics [161], ceramics [158] and so on.

However, strain measurement by the DIC method in piezoceramics under a large electric field loading is still hard to be performed because the extra insulating protection from arcing increases the difficulty for capturing a group of digital images with high quality. To work with strain gauges, kapton thin films were chosen for preventing arcing [162], but this is not suitable for the DIC method. The reason is that such a film also interferes with the observation between the camera and surface of sample. A liquid bath can also be used [153], however, the container should be designed to enable for illumination by the light source and observation by the camera. Malakooti and Sodano introduced the DIC method into measuring longitudinal and transverse strain coefficients of PZT-5H wafers with a thickness of 0.267 mm [147], and their testing was carried out under a 1.2 kV where there was no need for extra protection against arcing. Because of the danger of arcing, the presented set up cannot be used for larger sample sizes where higher voltages have to be applied to arrive at the same electric field strengths. It also has to be mentioned that the strain field on the surface of the specimen was missing in that work. For some lead-free ceramic/ceramic composites or complicated structures [138, 143], the full-field strain distribution is great helpful to understand the mechanical behavior in each component which can be used to develop new structures.

2.2 Fundamentals

The 2D-DIC technique compares two digital images captured from the same surface. Such an image provides the gray level of each pixel. This method is based on the principle of gray level conservation of square matrices of pixels between images. It means before and after deformation, the pixels of a certain square matrix keep their value of gray level. The reason why square matrices of pixels, rather than an individual pixel are selected for matching is that square matrices of pixels comprise a wider variation in gray level and, thus, will distinguish themselves more clearly from other matrices. Therefore, they can be identified in the subsequent images with more certainty [163].

Here, a “subset” is a square matrix of pixels where the gray level is obtained and its conserved gray level defines its feature for tracing its position between two images. The images of the surface are meshed into subsets, each of them including $(2N+1)$ by $(2N+1)$ pixels, where N is an integer. The specified position (x, y) of the center pixel of a subset is the initial condition to find the corresponding location (x', y') in the image of the deformed state. Consequently, the displacements u and v can be obtained from $u=x-x'$ and $v=y-y'$, respectively. To differentiate the subsets from each other, the surface should contain enough randomly distributed speckle patterns to provide sufficient random values of gray level for tracking the subset. The pattern can be provided by artificial speckles or natural texture. In this work, two types of specimens were employed. The natural texture on the surface of lead-based sample provides sufficient identification marks to be traced directly, but the artificial speckles are required on the surfaces of the lead-free samples. The method to create artificial speckles will be given in the next chapter. A correlation function is used to find the corresponding subset with a maximum correlation coefficient in the image of the deformed state. Commonly, the correlation function is the zero-normalized cross-correlation (ZNCC) [164], which can be written as

$$C(x', y') = \frac{\sum_{i=-N}^N \sum_{j=-N}^N [f(x_i, y_j) - \bar{f}][g(x_i, y_j) - \bar{g}]}{\sqrt{\sum_{i=-N}^N \sum_{j=-N}^N [f(x_i, y_j) - \bar{f}]^2} \sqrt{\sum_{i=-N}^N \sum_{j=-N}^N [g(x_i, y_j) - \bar{g}]^2}} \quad . \quad (\text{Equation 2.1})$$

In this function, $C(x', y')$ covers the range $[0, 1]$, and $f(x, y)$ and $g(x', y')$ is the gray level of the subset in the reference image and the image of deformed state, respectively. Furthermore, \bar{f} and \bar{g} are given as:

$$\bar{f} = \frac{1}{(2N+1)^2} \sum_{i=-N}^N \sum_{j=-N}^N f(x_i, y_j), \quad (\text{Equation 2.2})$$

$$\bar{g} = \frac{1}{(2N+1)^2} \sum_{i=-N}^N \sum_{j=-N}^N g(x_i, y_j). \quad (\text{Equation 2.3})$$

The correlation work is defined in a search region instead of the whole digital image to reduce the workload. The search region is the area of the surface which is evaluated in order to identify the center position of the subset after deformation. After computing the values of $C(x', y')$ in the whole search region, the center position of the subset with the maximum value of $C(x', y')$ will be treated as the corresponding location (x', y') . It should be mentioned that the ZNCC function used here is one of many correlation criteria which is chosen depending on the illumination conditions or sensitivity to noise [164-166]. As can be seen from the three equations above, the precision is limited to full pixel size. Sub-pixel interpolation schemes have been developed to increase accuracy of displacements, and the detailed algorithms of these interpolation schemes can be found in other reports [167, 168]. Among those algorithms, a curve-fitting method was adopted in this thesis. The position (x', y') with a maximum correlation coefficient (CC) (obtained by calculating the integer pixels) and its nearest eight positions (presented in integer pixels too) are interpolated using a second order polynomial to find the new position (x'', y'') with the new maximum CC'. Then the new displacements u' and v' in sub-pixels can be obtained from $u'=x-x''$ and $v'=y-y''$, respectively [169].

3 Specimens, experimental setups and methods

3.1 PIC151 soft PZT, NBT-7BT and NBT-6BT-3KNN

In this work, three groups of solid solutions and two types of ceramic/ceramic composites were chosen for the investigations.

The soft PZT material with easy domain motion is a great candidate to demonstrate the polarization and strain responses under stimulations. In addition, the properties of soft PZT materials are available owing to many reports that have been focused on this material. These published experimental data can be used to compare and validate the results measured from the work in this thesis. Therefore, the first experiments of this work (both the electric field and mechanical compressive loadings) were applied on the commercial soft PZT (PIC151, PI Ceramic, Lederhose, Germany). Samples were cut to rectangular blocks of 5×5×15mm by the manufacturer, with silver electrodes burned into the upper and bottom 5×5mm surfaces. The large aspect ratio of 3:1 was selected not only to mechanical loading also to analyze the deformation in various portions on the surface of a sample.

The reasons why this commercial material was selected are listed here. First, the properties of this material are available. Many reports based on this material have been published so that there are enough references can be used to validate the results measured from this work. Second, commercial material keeps the same properties for all the samples compared with the properties of “lab-made” material may show a variation among different samples. Therefore, the results measured from commercial PZT are expected to show a good repeatability if the experimental conditions are identical. At last, the soft PZT specimens provide natural speckle patterns with a good contrast. There is no need to paint any artificial patterns on the surface which could induce arcing during the extremely high electric potential (± 30 kV).

0.93Na_{1/2}Bi_{1/2}TiO₃-0.07BaTiO₃ (NBT-7BT) is a lead-free solid solution with the content of 93 mol.% NBT and 7 mol.% BT. 0.91Na_{1/2}Bi_{1/2}TiO₃-0.06BaTiO₃-0.03K_{0.5}Na_{0.5}NbO₃ (NBT-6BT-3KNN or NBT-BT-3KNN) was prepared by adding 3 mol.% of KNN into NBT-6BT. These two types of powder were prepared through the solid oxide synthesis, separately. The raw materials of Bi₂O₃ (99.975% purity), BaCO₃ (99.8% purity), K₂CO₃ (99.0% purity), Na₂CO₃ (99.5% purity), TiO₂ (99.6% purity), and Nb₂O₅ (99.9% purity) (all Alfa Aesar GmbH & Co. KG, Karlsruhe, Germany) were mixed according to their stoichiometric formula and ball-milled in ethanol for 24 h. The dried slurries were calcined for 2 h at 700°C, followed by 3 h at 800°C. Then the calcined powder was ball-milled for 24 h [138].

These two groups of powder were used to prepare four types of specimens: (1) pure NBT-7BT ceramic [72], (2) pure NBT-6BT-3KNN ceramic [75], (3) NBT-7BT/NBT-6BT-3KNN bilayer composites [84] and (4) NBT-7BT/NBT-6BT-3KNN/NBT-7BT trilayer composites. The bilayer was a 50/50 composite by weight of equal amounts of the two end members. The trilayer was 33% NBT-7BT in the center, with NBT-6BT-3KNN in equal amounts on the top and bottom of the composite. NBT-7BT and NBT-6BT-3KNN samples were cut to rectangular blocks of 4.7×4.7×6.3 mm and 4.25×4.25×2.7 mm, respectively. Bilayers and trilayers were prepared to the same size of 4.25×4.25×4.45 mm with silver electrodes brushed onto the upper and bottom 4.25×4.25 mm surfaces. All these lead-free specimens were provided by Mrs A. Ayrikyan who is pursuing her PhD in the group of Prof. K.G. Webber at the university of Erlangen-Nürnberg.

Before the strain measurement by using the DIC method, the quality of speckles on an observation surface was checked first. The average value of correlation coefficient (CC) is required to be larger than 0.95 (based on the experience in this work) to ensure a good tracing during the experiments. Once this value is less than 0.95, artificial speckles are needed to be sprayed onto the observation surface in addition to the natural texture on the same surface. An air brush (AT-Airbrush Pistole Kit, AT-AK-02, Agora-Tec, Germany) was employed to do the painting. The size of a droplet of the paint (Model Air, Black, Acrylicos Vallejo, Spain) can be controlled by the air brush to create patterns suitable for the DIC tracking. After that, the CC value was checked once more to determine whether painting was required again or not. The loop of painting and CC value checking could be repeated several times until the quality of patterns meets the requirement.

3.2 Experimental setups for the investigations

Figure 3.1 shows a sketch of the setup, which was developed for measuring the strain and polarization under high-voltage conditions. A modified Sawyer–Tower circuit combined with an electrometer (6514, Keithley Instruments, Cleveland, USA) was used to monitor the voltage variation of a capacitor that was connected in series with the specimen in order to measure the polarization of the ceramic. The electric-field-induced strains are measured by means of a LVDT sensor (Type W1T3, HBM, Darmstadt, Germany) as well as a digital camera.

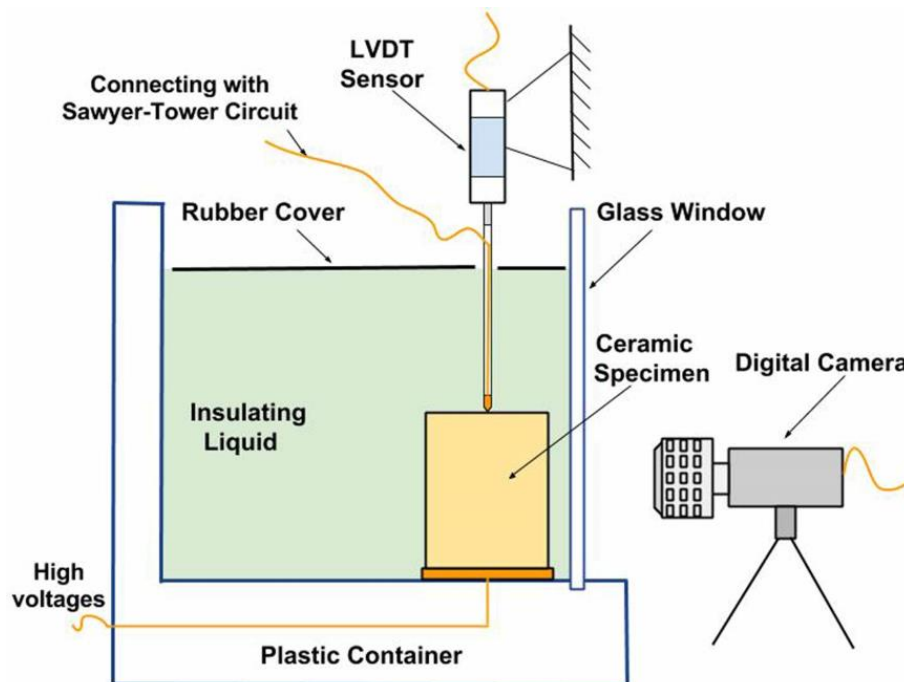


Figure 3.1: Experimental setup for measuring electric field-induced strains.

The silicone oil bath (AB118663, abcr GmbH, Karlsruhe, Germany) container provides excellent protection from arcing which may be caused by the electric potential with the maximum values of ± 30 kV. The loading of electric fields was generated by a bipolar high-voltage power supply (HCB 15-30000, F.u.G., Rosenheim, Germany).

In addition to a digital camera mentioned above, the whole DIC system was equipped by a glass window, a light source (Halogen optic lamp, Osram, Augsburg, Germany), a digital camera with the maximum resolution of 2208×3000 pixels (PL-B782F, Pixelink, Ottawa, Canada), and two lens with

fixed magnifications ($1\times$ and $2\times$, MVO-TML telecentric measuring lens, Edmund Optics Inc., Germany). The glass window provides a direct view at the specimen for the camera to capture images, and the telecentric lens is helpful to ignore the slight out-of-plane motion. For these two lenses, the $2\times$ lens provides a higher resolution ($1.75\ \mu\text{m}/\text{pixel}$) while the $1\times$ lens ($3.5\ \mu\text{m}/\text{pixel}$) is suitable for observing a larger surface on a sample.

Figure 3.2 shows the setup for measuring the deformation and polarization under a compressive load. A special alignment fixture was designed. Using this fixture, the compressive force acts in line with the axis of the specimen and consequently, superposed bending is avoided. The compressive stress was applied using a servohydraulic load frame (Model 1361, Instron, Canton, USA). During the loading and unloading, a Sawyer–Tower circuit combined with an electrometer (6517A, Keithley Instruments, Cleveland, USA) was employed to monitor polarization charges. The strains were obtained from the DIC system using the observation of $1\times$ lens.

During both the electric field and mechanical compressive loadings, two digital images were captured per second to monitor the deformation of a specimen. All the experimental setups were controlled and the data were acquired by a computer running LABVIEW 2009. After completing the experiment, the MATLAB R2011b software [169, 170] were used to analyze the images captured during the loadings.

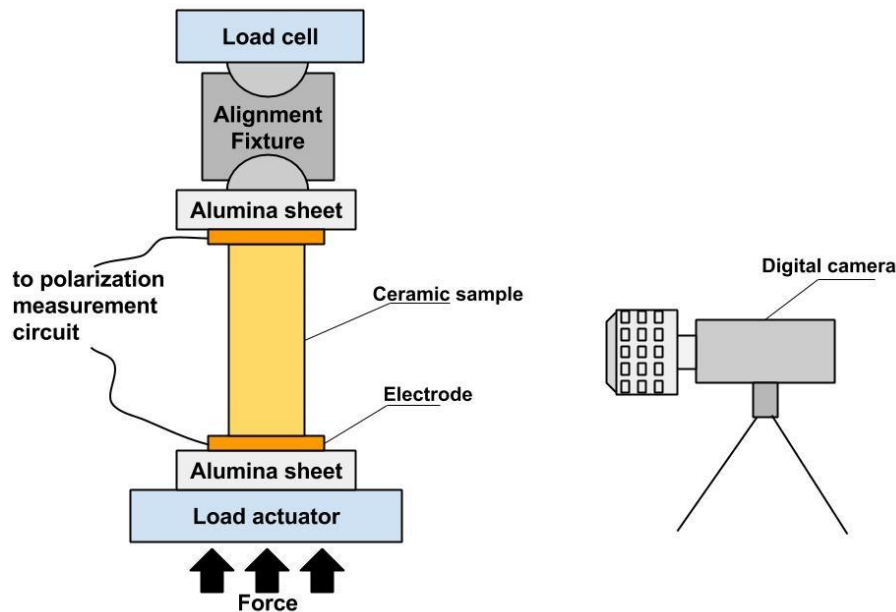


Figure 3.2: Experimental setup used for compression test.

3.3 Implementation of DIC method in this work

A series of digital images captured during the experiments are the raw data which contain the whole information of the deformation. Therefore, suitable software is required to deal with those as-captured images and extract the useful information from there.

In the digital images the origin of the coordinate system for locating pixels will always be the upper left corner, as indicated in Figure 3.3. From the origin, the transverse orientation is pointing in x -direction, and the longitudinal orientation is in y -direction. Using these coordinates, every single pixel is assigned a precise position. The red crosses represent the targets for tracing, i.e. the centers of the subsets to be traced. Consequently the area of the images covered by the red crosses will be the corresponding region of interest (ROI) for evaluating the strains. The number of red crosses is decided by the step size

(determining the density of tracing targets). For example, the step size in Figure 3.3 is 50×50 pixels which means that the distance between a red cross and its nearest neighbor is 50 pixels in both width and length directions. The basic principle of using DIC to realize image comparing and subset correlating were introduced in section 2.2. After the procedures of comparing images and matching the subsets, the new position in the images of the deformed state and the displacement of each center pixel of the traced subsets can be obtained.

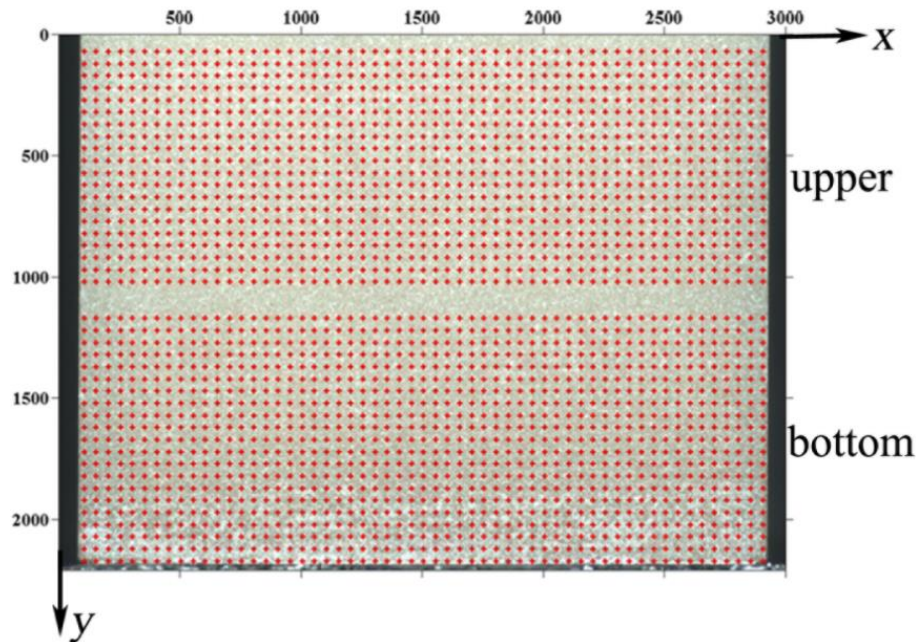


Figure 3.3: Two ROIs marked by selected the red crosses ready for DIC tracing.

In a selected ROI, the longitudinal displacement v of all subsets versus corresponding vertical position y can be plotted so that a linear fitting operation can be applied afterwards. The value of longitudinal strain in y -direction of the corresponding region equals the slope of that fitting line. The accuracy of strain obtained by using this algorithm is influenced by the fitting range strongly. This influence will be discussed in the following section. With the same operation, but using the values of u and x instead of v and y , the strain in x -direction (transverse strain) can be obtained, too. This method for calculating strains gives an average or a general strain corresponding to the selected ROI. If, for example, one wants to examine the homogeneity of deformation, several appropriate ROIs where the strains can be obtained independently are needed. These ROIs locating on the surface of a specimen work similarly to employing couples of strain gauges at the corresponding areas simultaneously. More details can be found at the website of the freely available code for this method programmed by C. Eberl and his colleagues [170]. Here, it is named code I.

In many tasks of experimental solid mechanics, the spatial distribution of the strain components of the whole surface is of interest. In this case, the strain distributions are calculated from finite element shape functions used to interpolate the displacements. This method can provide more “local” strain information by drawing a contour plot of strains. An open source code to achieve this was developed by E. Jones (in this paper it is named code II) [169]. Commercial software is also available to obtain the distribution of strain [171], but in this work, only the two open source codes using Matlab as calculating engine mentioned before were adopted. Further details on the 2D-DIC method can be found in several review articles [163, 172].

3.4 Error analysis on the strain measured from DIC method

3.4.1 Errors from the DIC codes and the setup

In order to evaluate both the two DIC codes used in this work, the example images named “2D Test Image Sets, Sample 3” were downloaded from the website of “Digital Image Correlation Challenge” in the Society for Experimental Mechanics [173]. “2D Test Image Sets, Sample 3” is a group of 12 images provides rigid translation by 0.1 pixel increment up to 1 pixel. A subset size of 20 pixels was selected to do these evaluations. Loading these standard images into the calculating engines (code I and II), the errors can be estimated by comparing the calculated results and the specified values provided by the authors of the standard images.

For the code I from C. Eberl *et al.*, the error in displacement is about 0.007 pixel. In this code, the slope of linear fit of the displacement versus position allows to get the value of longitudinal or transverse strain, so the error of strain depends on the range of fitting area. For instance, to calculate longitudinal strain, the fitting range covers 400 pixels (from y -position 50 to y -position 450). Then the magnitude of the error in longitudinal strain of this ROI will be $\sim 10^{-6}$, which means $\sim 10^{-4}\%$. When the ROI is a tiny region covering only 50 pixels in y -direction, the magnitude of the error in average strain could reach $\sim 10^{-2}\%$. Using the fitting method on displacement u and x -position, the error in transverse strain can be estimated too.

The accuracy of the code II from E. Jones was evaluated by taking the same standard images. Fortunately, the author who programed this code also gave a report on the error analysis. The results in details can be found in a file named “DIC Challenge – Summary of Results”[169]. With the step size of 5 pixels, this report lists the errors in displacement and strain which are 0.005 pixel and 0.015%, respectively. In this code, before calculating the strain, a Gaussian distribution of weights with 11 control points and 3 smoothing passes are used to smooth the displacement. Then, the method of displacement interpolation over 16 nodes, bi-cubic finite elements were taken to calculate the strains.

The noise coming from the setup is another part that influences the accuracy of the measurement. Such as the cleanliness of the glass window, illumination condition, the focusing accuracy of the lenses, etc. To simplify the work of analyzing, those influence factors will not be discussed each by each. Only a group of images captured from a PZT sample standing in the setup (Figure 3.1) plays the role of the analysis object. Similar to the standard images provided by the “DIC Challenge”, the surface of PZT provides good speckles with enough contrast. The average value of the correlation coefficient was checked to make sure this value was larger than 0.98, which means the correlation work was completed well to meet the requirement. Owing to no loads or operation, the displacement and strain were supposed to be 0, but the calculated displacement shows the magnitude of the noise to be in average of $\sim 10^{-2}$ pixel. Table 3.1 and Table 3.2 list the summary of the error results.

Table 3.1: Magnitude of errors in displacement and strain estimated from standard images (downloaded from Society for Experimental Mechanics).

	Magnitude of error in displacement (pixels)	Magnitude of error in strain (%)
Code I	7.0×10^{-3}	$\sim 10^{-4}$ (fitting range: 400 by 400 pixels) $\sim 10^{-2}$ (fitting range: 50 by 50 pixels)
Code II	5.0×10^{-3}	1.5×10^{-2}

Table 3.2: Magnitude of errors in displacement and strain estimated from a PZT specimen (a sample used in this work at static state).

	Magnitude of error in displacement (pixels)	Magnitude of error in longitudinal strain (%)
Code I	6.5×10^{-2}	$\sim 10^{-4}$ (fitting range: 1800 pixels in y-position) $\sim 10^{-3}$ (fitting range: 500 pixels in y-position)
Code II	6.0×10^{-2}	7.0×10^{-2}

3.4.2 Noise caused by the motion of insulating liquid

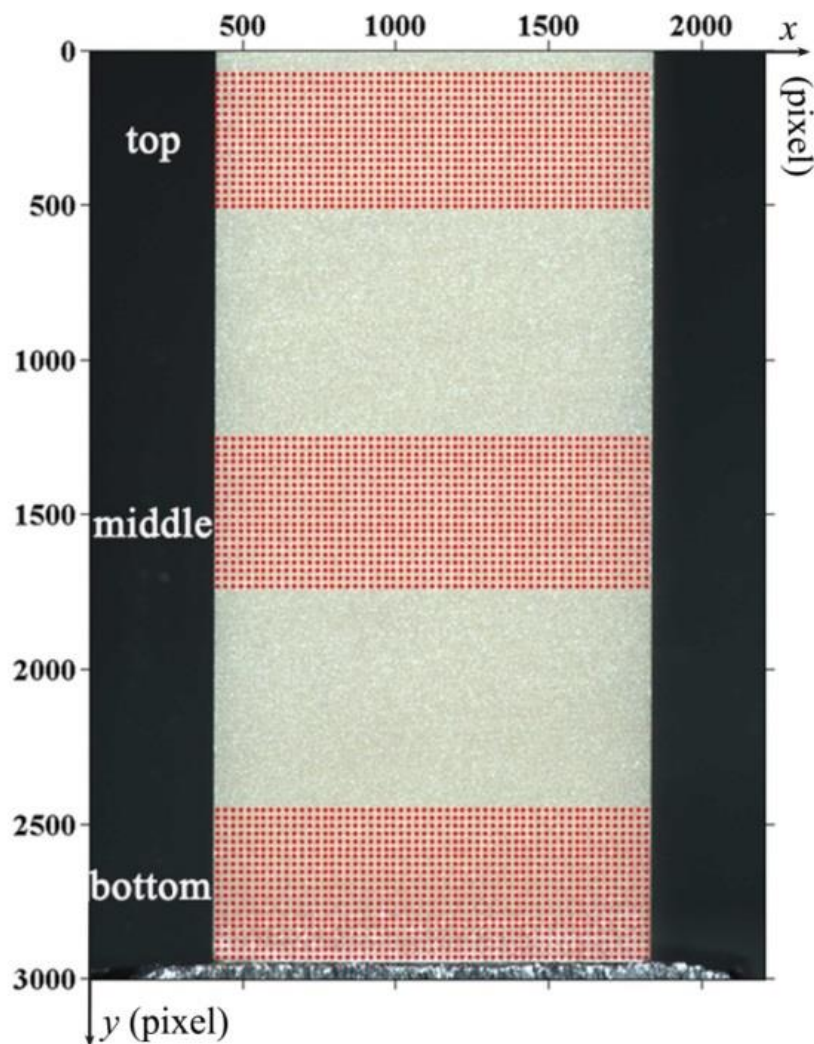


Figure 3.4: Three ROIs selected for calculating the corresponded strains.

In the experiments of electric field loadings, the electric field causes a motion of insulating liquid which influences the accuracy of the strain measurement strongly. Therefore, the discussion on a PZT specimen with zero loading in last section is not enough.

Figure 3.4 shows three ROIs selected for calculating strains and the results are plotted in Figure 3.5. In those three ROIs, each covers 500 pixels along y-direction. Based on the result in Table 3.2, the error in strain is $\sim 10^{-3}$ %. However, Figure 3.5(a) presents lots of noise in the results larger than $\sim 10^{-3}$ % obvi-

ously. Although the insulating liquid is kept as clean as possible, a high voltage still leads to some degree of motion. Consequently, the interface between the air and liquid is not kept still, but reflection and refraction happen there which change the illumination conditions on the PZT surface during the quasi-static loading at high voltages. The evidence is shown in Figure 3.5(a) where the result from the top region (close to the interface between the air and liquid) contains more noise than the result from the bottom region (the illumination condition is more stable). It is expected that, more liquid lifting the liquid level far away from the top region of the specimen is helpful.

In addition to filling more liquid into the container, some other solutions can be used in order to minimize this liquid motion-induced noise. In Figure 3.1, a piece of black rubber is placed between the air and the liquid to cut off the light path. Meanwhile, the specimen is placed as close as possible to the glass window instead of the center of the container which also can be seen in Figure 3.1. After taking those modifications, the experiment was repeated again and the results are revealed in Figure 3.5(b). Compared with the results in Figure 3.5(a), the three curves measured after taking the three solutions demonstrate a high agreement with each other and most importantly, the noise is minimized.

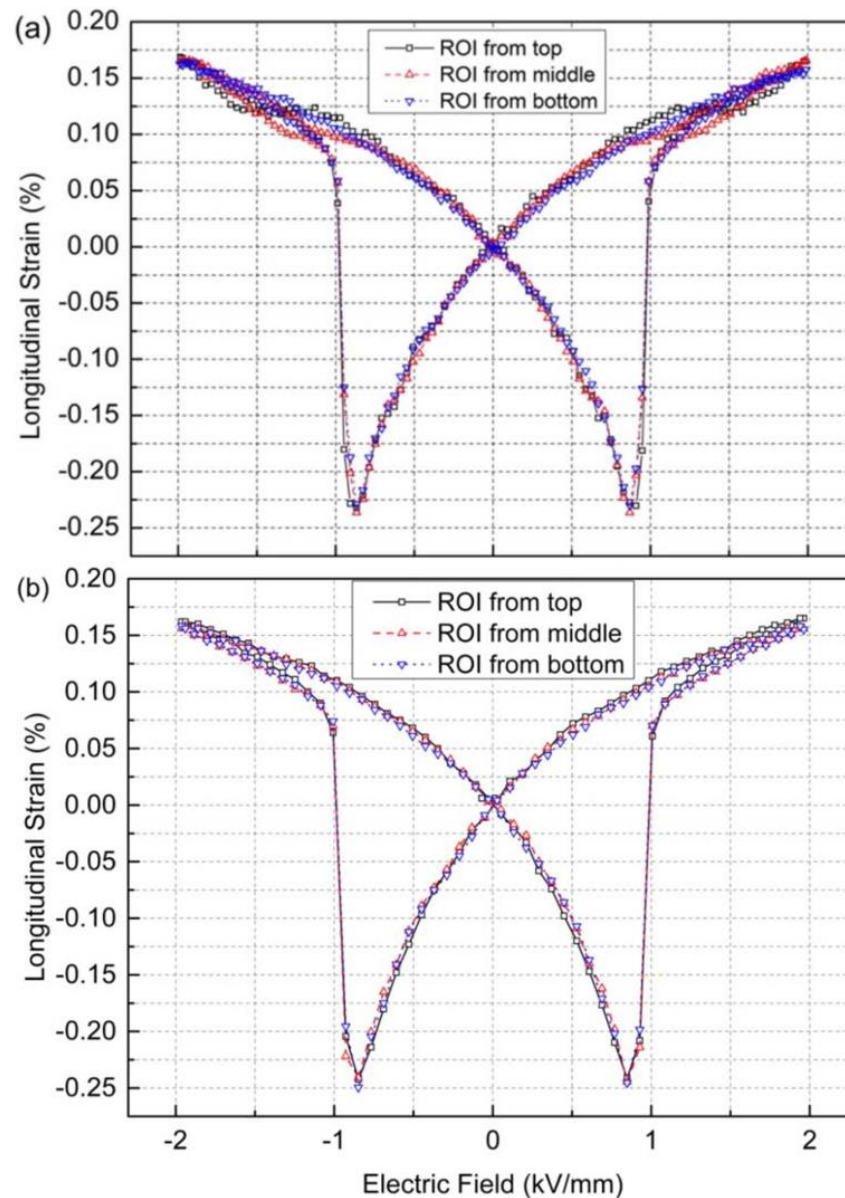


Figure 3.5: Longitudinal strains calculated from three ROIs on one surface: (a) results containing obvious noises; (b) results obtained from the same setup after some modifications.

4 Deformation behavior on PZT samples

4.1 Experiments under electric field loadings

The work in this chapter was aimed in the first place to determine the feasibility of using the DIC system to measure the electric field-induced strain rather than finding new knowledge on the PZT material. So there are not many discussions on the properties of the material but the introductions on this setup to achieve the measurement are provided [174]. The commercial soft PZT (shown in Figure 4.1) was picked to perform this investigation. The introduction of this sample and the reason why this material was chosen haven been given in section 3.1.

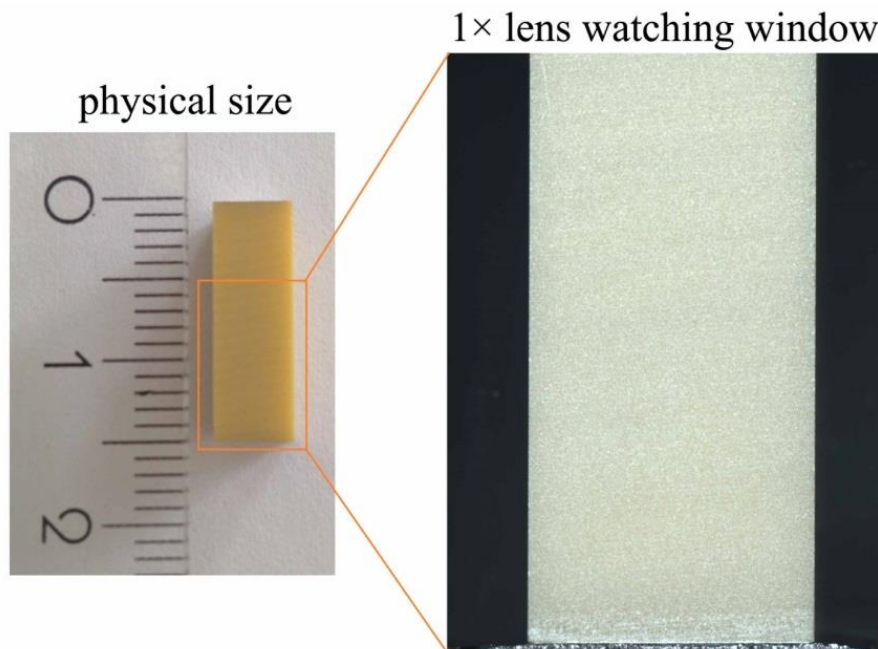


Figure 4.1: The physical size of the sample and the selected watching window under the lens.

4.1.1 Experimental procedures

The setup for this work has been shown in Figure 3.1 and the introduction of the measurement has been given by Chapter 3, too. In section 4.1, all the tests were completed by using triangle waveform cyclic electric field loadings with amplitude of ± 2 kV/mm and a loading rate of 0.08 kV/mm per second (0.01Hz). The camera with the 1x lens captured 2 images per second to record the deformation of the object when the loading was applied.

4.1.2 Validation of the DIC method

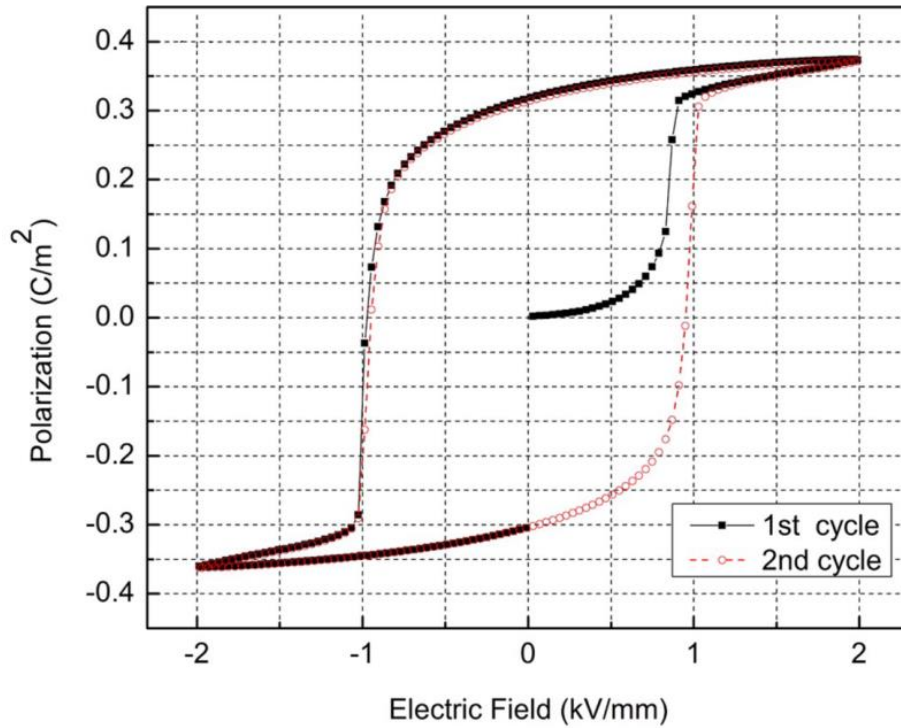


Figure 4.2: Polarization hysteresis loops induced by cyclic electric field loadings.

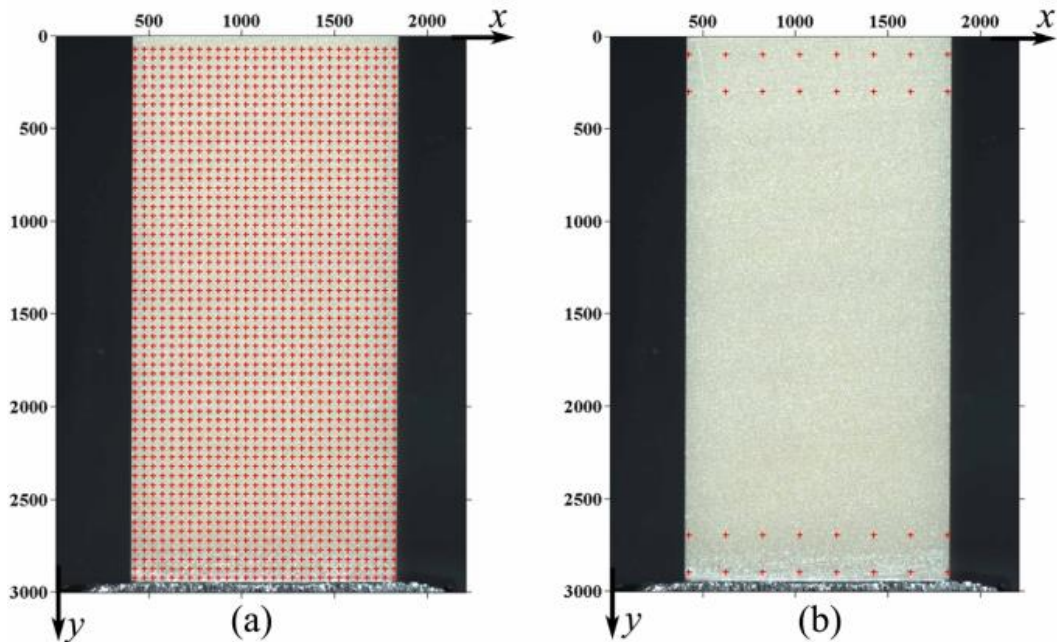


Figure 4.3: Reference images and regions of interest for DIC tracing (unit in coordinates is pixel).

Figure 4.2 shows the typical polarization hysteresis curves. Before the electric field loading, the PZT specimens are in an unpoled state. Therefore, the domains are randomly distributed in the ceramic and, thus, spontaneous polarization and strain of all domains result in vanishing macroscopic remnant polarization and strain, initially. As the magnitude of the electric field is increased beyond a certain

threshold value, usually characterized by the so-called coercive field strength, the domains are gradually aligned to the loading direction. The initial random domain state is never attained again during the loading history. This explains the difference between the first half cycle of loading and subsequent loading cycles and this hysteresis behavior has been reported in other publications [21, 175].

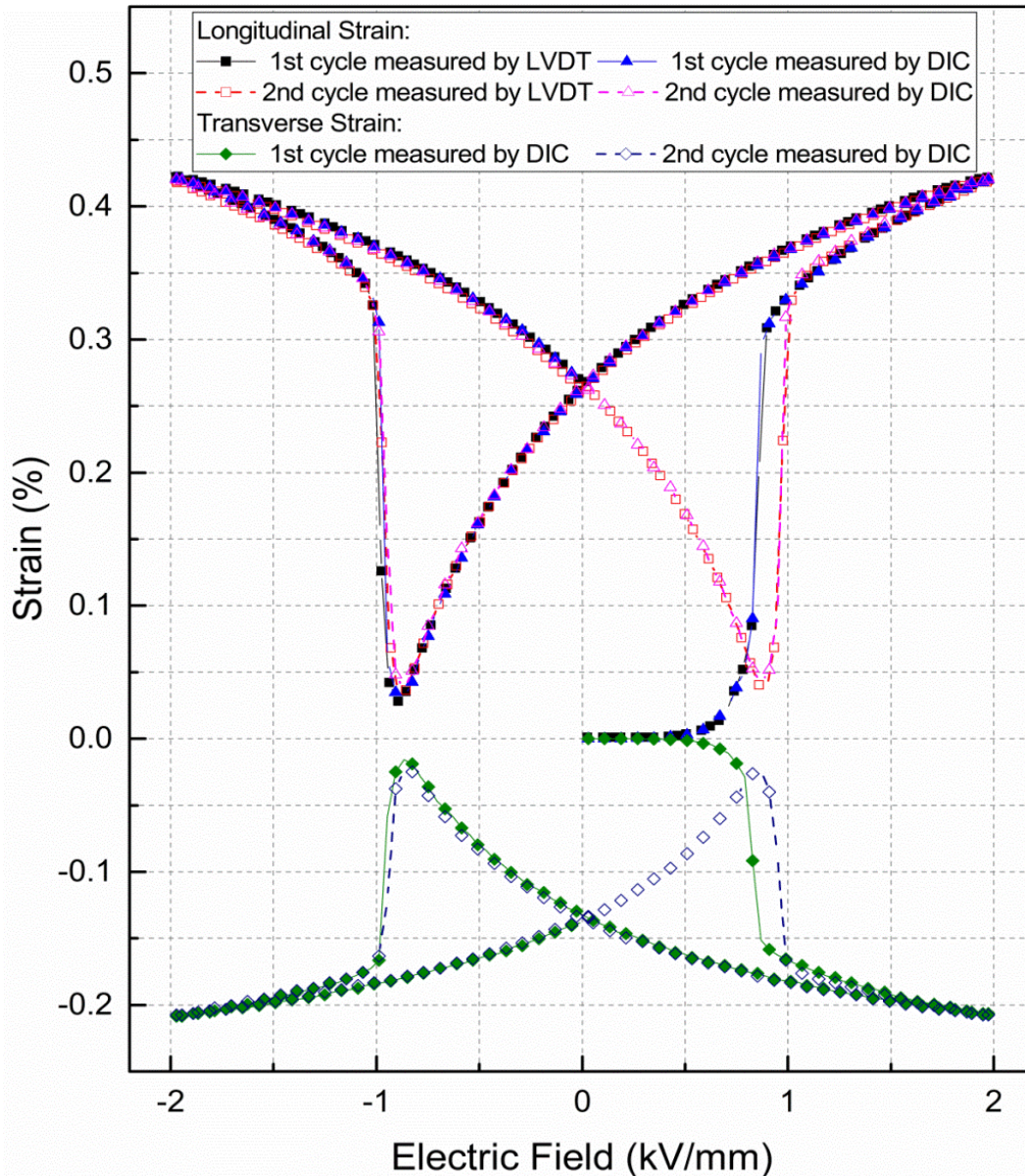


Figure 4.4: Strain-electric field curves measured by DIC method and LVDT.

Figure 4.3 shows two different selected ROIs from the same surface on one sample. The subset size of 15×15 pixels was selected for all the DIC evaluations and the step size is 50 pixels and 25 pixels for Figure 4.3(a) and Figure 4.3(b), respectively. The ROI marked in Figure 4.3(a) contains hundreds of centers of tracing targets (red crosses) covering the whole observed surface. The ROI in Figure 4.3(b) is covered by dozens of red crosses only. It is still a complete ROI aiming to check the general strain along the longitudinal direction although these centers of tracing targets were placed around the top and bottom regions. The results calculated from these two ROIs will be demonstrated in the following discussion.

To validate the DIC method, a ROI was selected as shown in Figure 4.3(a), and both, longitudinal and transverse strains were calculated. Simultaneously, the LVDT sensor was used to measure the longitudinal strain. The comparison of the *S-E* butterfly curves measured by employing the two methods is plotted in Figure 4.4. The butterfly loop obtained from the LVDT data shows a good agreement with the longitudinal strain measured by using DIC method. Although there are tiny differences between the results from the two methods, the accuracy of the DIC measurement still can be confirmed. Due to the working principle of DIC, the displacement along both, y and x , directions can be obtained at the same time, and the transverse strains are also plotted in Figure 4.4. Using the same ROI in a single experiment, diverse types of strains can be calculated.

4.1.3 Strain measured from DIC displacement gauge

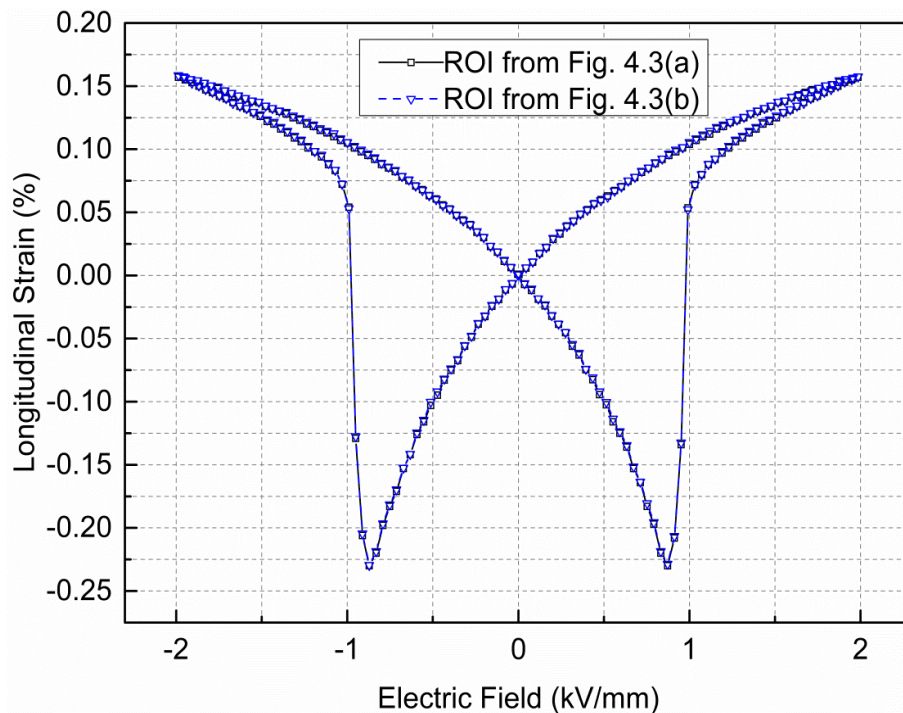


Figure 4.5: Longitudinal strains measured from diverse ROIs.

Unlike the LVDT or a strain gauge, the DIC method cannot get the displacement or the strain information immediately. They must be calculated from a series of images in a post processing step. The processing of the images takes time depending on the workload. Thus, optimization by selecting ROIs to relieve processing demands is necessary. In order to simulate a LVDT-measurement by means of the DIC method, only the regions close to the top and the bottom of the sample are included in one ROI. The bottom region plays a role of a reference, and the top region catches the longitudinal displacement of the upper surface. As shown in Figure 4.3(b), only 32 targets compose the ROI which covers two small parts on the viewed surface and, consequently, the computation time was much shorter compared to the selection in Figure 4.3(a). This quick checking method is known as DIC displacement gauge checking.

200 images were captured to describe one loading loop. The processing time of the ROIs in Figure 4.3(a) and Figure 4.3(b) were about 50 min and 5 min, respectively. Figure 4.5 reveals the longitudinal strain curves from the measurements corresponding to Figure 4.3, which match each other perfectly. From these results it can be seen that by selection of the ROI optimized for the purposes of a certain

measurement, the computation time for tracing markers can be reduced significantly without loss of accuracy.

4.1.4 Spatial distribution of the strain components

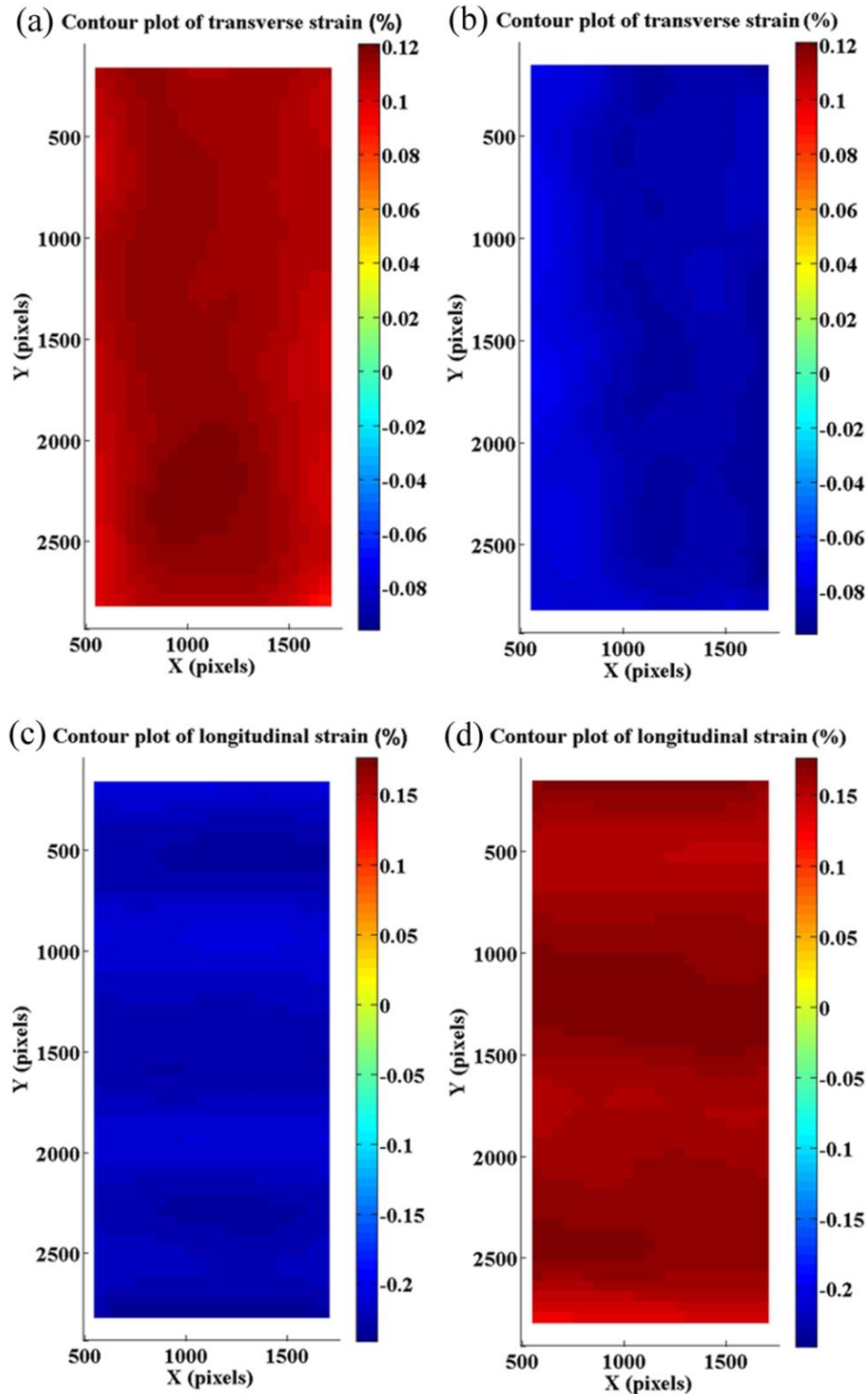


Figure 4.6: Distributions of transverse and longitudinal strains: (a) contour plot of transverse strain measured at 0.87 kV/mm; (b) contour plot of transverse strain measured at 2 kV/mm; (c) contour plot of longitudinal strain measured at 0.87 kV/mm; (d) contour plot of longitudinal strain measured at 2 kV/mm.

The spatial distribution of the strain components of the whole surface was obtained. It has a great potential on monitoring the deformation of piezoceramics under electric field loads, especially for understanding the mechanical behavior of some complex composites or multilayer structures [138, 143]. Here, a specimen of the pure component of PZT was used to discuss the homogeneity of deformation. The same group of images to calculate the overall strain to obtain Figure 4.4 was taken again to compute the distribution of the strain.

Figure 4.6 shows the distributions of transverse and longitudinal strains under an electric field of 0.87 kV/mm around the coercive field and at the maximum loading of 2 kV/mm, respectively. It should be mentioned that, the resolution of the lens is limited to 3.5 $\mu\text{m}/\text{pixel}$, and the step size was set to 25 by 25 pixels in this experiment. Under this observation and calculating scale, Figure 4.6 provides a macroscopic strain field on a surface of the specimen in fact, rather than a microscopic strain which depends on the micro structure of the material. Although the word “distribution of strain” is used here and in the following discussion, the scale of obtaining the strain should be noticed.

Owing to using a pure component of PZT, it is expected that the strain is homogeneously distributed under the electric field loadings. The evidence is provided by Figure 4.6, although the measured strain distributions show some random noise causing tiny differences in various parts. In general, force on the sample may induce a constraint, but in Figure 4.6 there is no inhomogeneity of strains visible in either transverse or longitudinal directions even at the bottom. Result from that, the strain is not affected by any mechanical constraints.

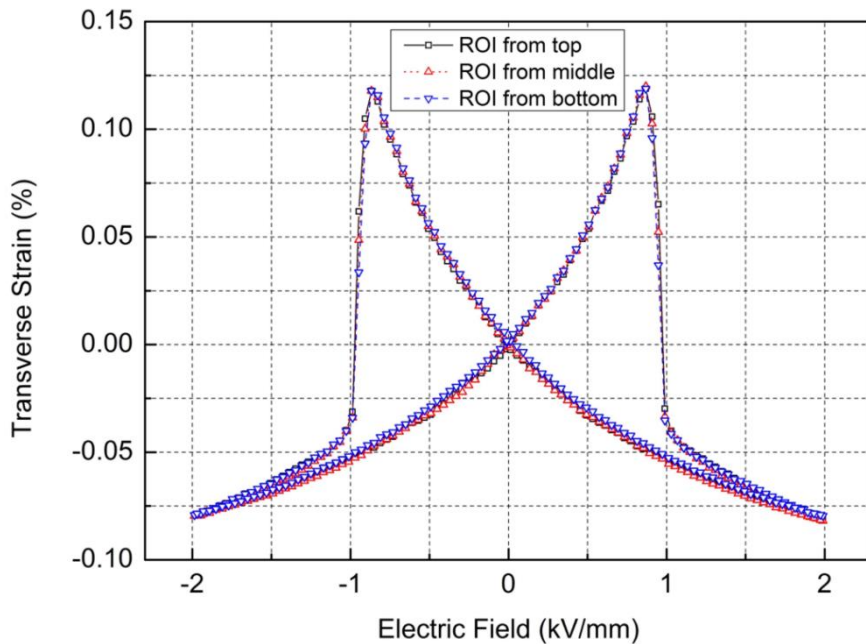


Figure 4.7: Transverse strain measured from diverse ROIs of Figure 3.4.

The strain distributions in Figure 4.6 only provide two states of the whole electric field loading history. To further investigate the entire loading, one watching window was separated into three sub-regions as shown in Figure 3.4 and the longitudinal and transverse strains calculated by code I were plotted in Figure 3.5(b) and Figure 4.7, respectively. In these figures, one can find that the values of strain from the correspondingly selected ROIs match each other very well. So, together with the results in Figure 4.6, it can be concluded that the ceramic sample experiences a highly homogeneous deformation on a macro scale during the entire electric field loading.

4.2 Experiments under mechanical compressive stress loadings

The PZT material is not only often subject to electric loadings but also to large compressive forces which should be considered for device design. In order to assess the reliability of a piezoceramic component, it is important to estimate its mechanical stress-strain relationship quantitatively. Simulation and modelling methods were developed to describe the nonlinearity caused by domain switching processes under strong compressive stress [176, 177]. Reliable stress-strain experimental data are needed to build and verify those models, which makes the measurement of strains play a significant part in developing them. Therefore, experiments under pure compressive stresses were performed [178]. Following the previous section, the DIC method was employed to investigate the homogeneity of the deformation in a slender bulk specimen under mechanical compression here.

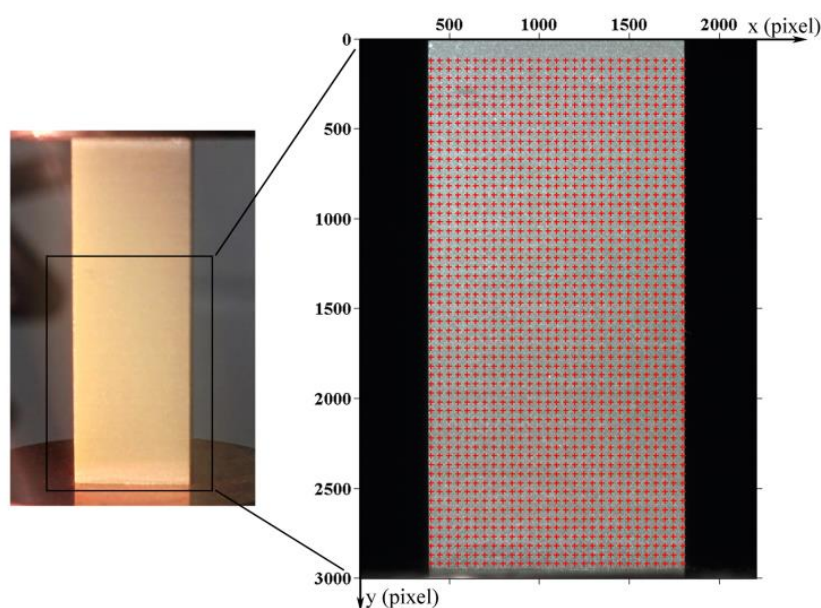


Figure 4.8: Observation window of DIC and the reference image with the assigned coordination system.

4.2.1 Experimental procedures

The same type of PZT material was chosen in this investigation. The sample with a size of 5 by 5 by 15 mm was not necessary in the previous section 4.1 to conduct the bipolar electric field loadings. The large height of 15 mm requires an extremely high potential of 30 kV to create a suitable electric field of 2 kV/mm. It demands highly careful operation during the experiments to avoid any accident. However, a sufficiently large surface with the size of 5 by 15 mm is provided due to the large aspect ratio of 3:1. This aspect ratio brings advantages into this compression investigation. It is convenient to analyze the deformation from three portions of the sample (top, center and bottom regions) and figure out from which region the true stress-strain experimental data can be obtained.

The setup used to perform this investigation has been introduced in Chapter 3 (Figure 3.2). Before the compressive loading, the sample was poled under triangle waveform cyclic electric field loadings for 10 cycles, with the amplitude of ± 2 kV/mm and a loading rate of 0.08 kV/mm per second (0.01 Hz). Then the compressive loading and unloading rate was controlled at 5 MPa/s with the loading range

from 0 to -400 MPa (0.625 mHz), and 3 cycles were applied. During the compression test, 2 digital images were captured per second to monitor the deformation of the specimen.

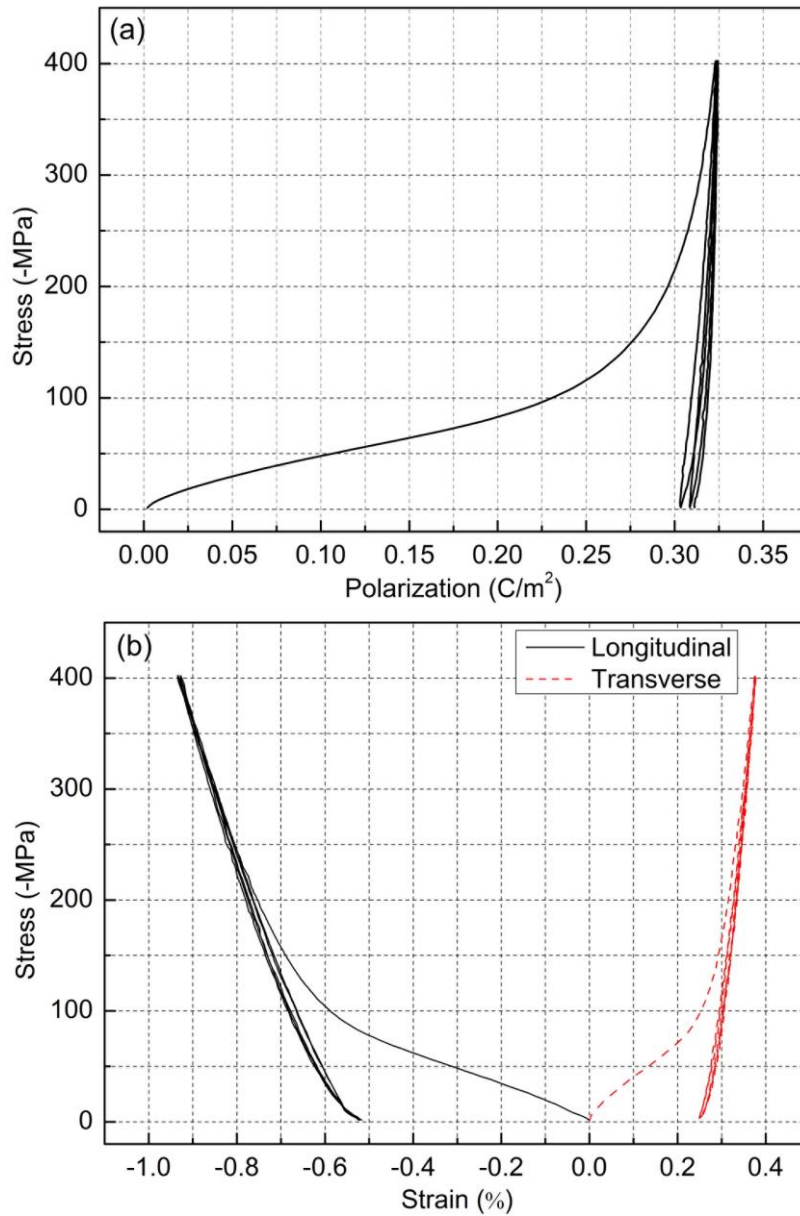


Figure 4.9: Three cycles of responses of compressive stress: (a) mechanical depolarization curve; (b) longitudinal and transverse strain versus stress.

4.2.2 Strain measurement on single region of interest

In Figure 4.8, it can be seen that the observation window covers two thirds of the whole 5×15 mm surface area at its central and bottom portion. Due to symmetry of the specimen, the upper part beyond the observation window is not considered here. As an advantage of the DIC method, both the longitudinal and transverse strains can be gained from evaluating correspondingly selected ROIs easily. It was mentioned in the former chapters that the red crosses represent markers chosen for tracing which are the center pixels of target subsets, and the parts of the images covered by those red markers will play the role of the ROI.

Figure 4.9 shows the results of depolarization and strain curves under cyclic compressive loadings. Before the compressive loading, the pre-poled state was selected as the reference, thus the starting value of the depolarization and strain curves was set as zero. These curves are very close to other published results on PZT ceramics [179, 180], and the nonlinear behavior of pre-poled PZT can be attributed to stress induced ferroelastic domain switching mechanisms [23]. As a special feature, the DIC method can be used to calculate both the longitudinal and transverse strains from the same ROI. In Figure 4.9(b), these two stress-strain curves come from the same ROI selected as shown in Figure 4.8 where both the central and bottom portions are contained. These curves present the general or average strain results, which cannot provide further details on the distribution of strain within the corresponding ROI.

4.2.3 Strain measurement on multi-regions of interest

The uniaxial compression testing of brittle materials is difficult given the requirement that the loading be applied symmetrically such that no superposed bending occurs. The ROI regions 1 (R1) and 2 (R2) marked in Figure 4.10 were selected to examine whether there was any superposed bending effect. It can be seen that R1 and R2 are located close to the left and right edges of the specimen. In Figure 4.11, the longitudinal stress-strain curves of R1 and R2 can be found. Although there are slight differences of the longitudinal strain curves between the left and right edges, the capability of the setup to avoid superposed bending was still confirmed to a sufficient degree. Because only bending along one axis is checked in Figure 4.10, to make sure no bending happened along the other axis, the same operation was repeated several times by capturing other surfaces and the results matched those in Figure 4.11 very well.

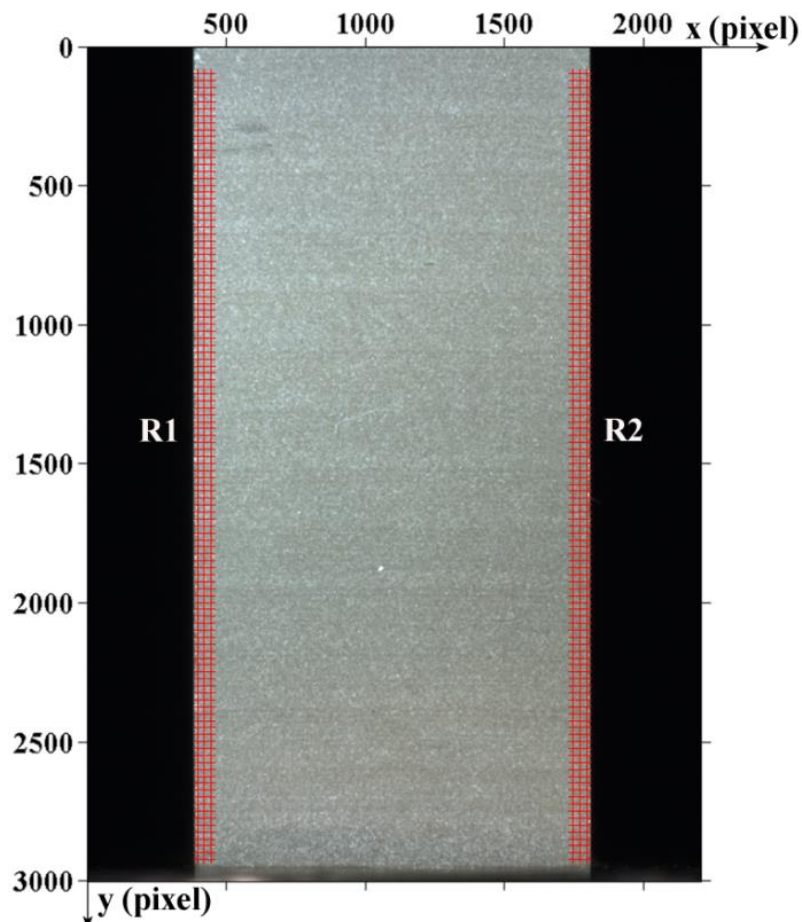


Figure 4.10: Selected ROIs on the surface of sample for calculating longitudinal strains.

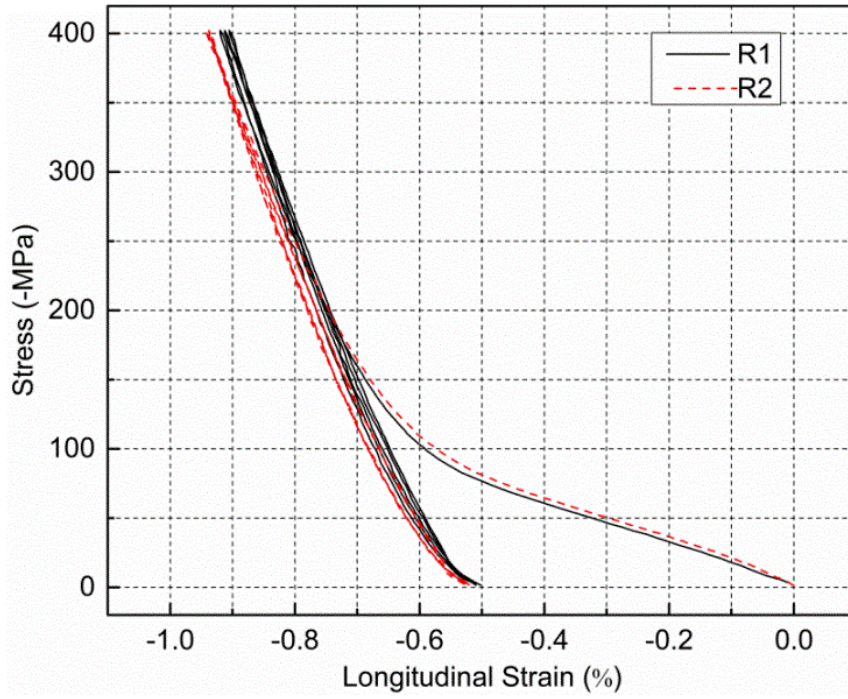


Figure 4.11: Stress-strain curves measured from R1 and R2.

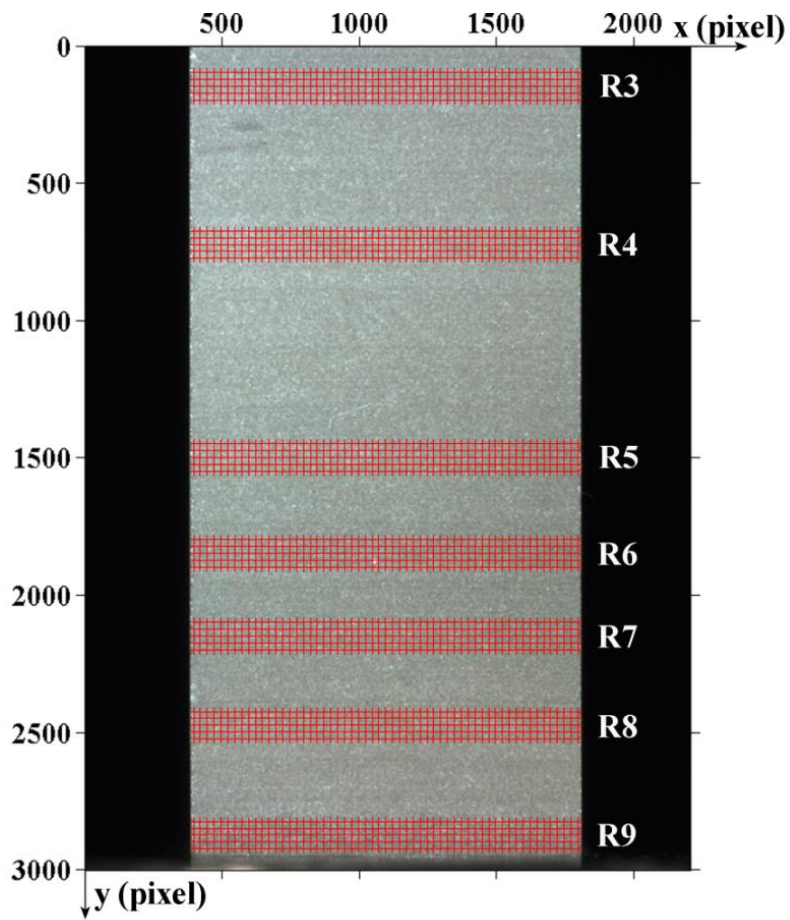


Figure 4.12: Selected ROIs on the surface of sample for calculating transverse strains.

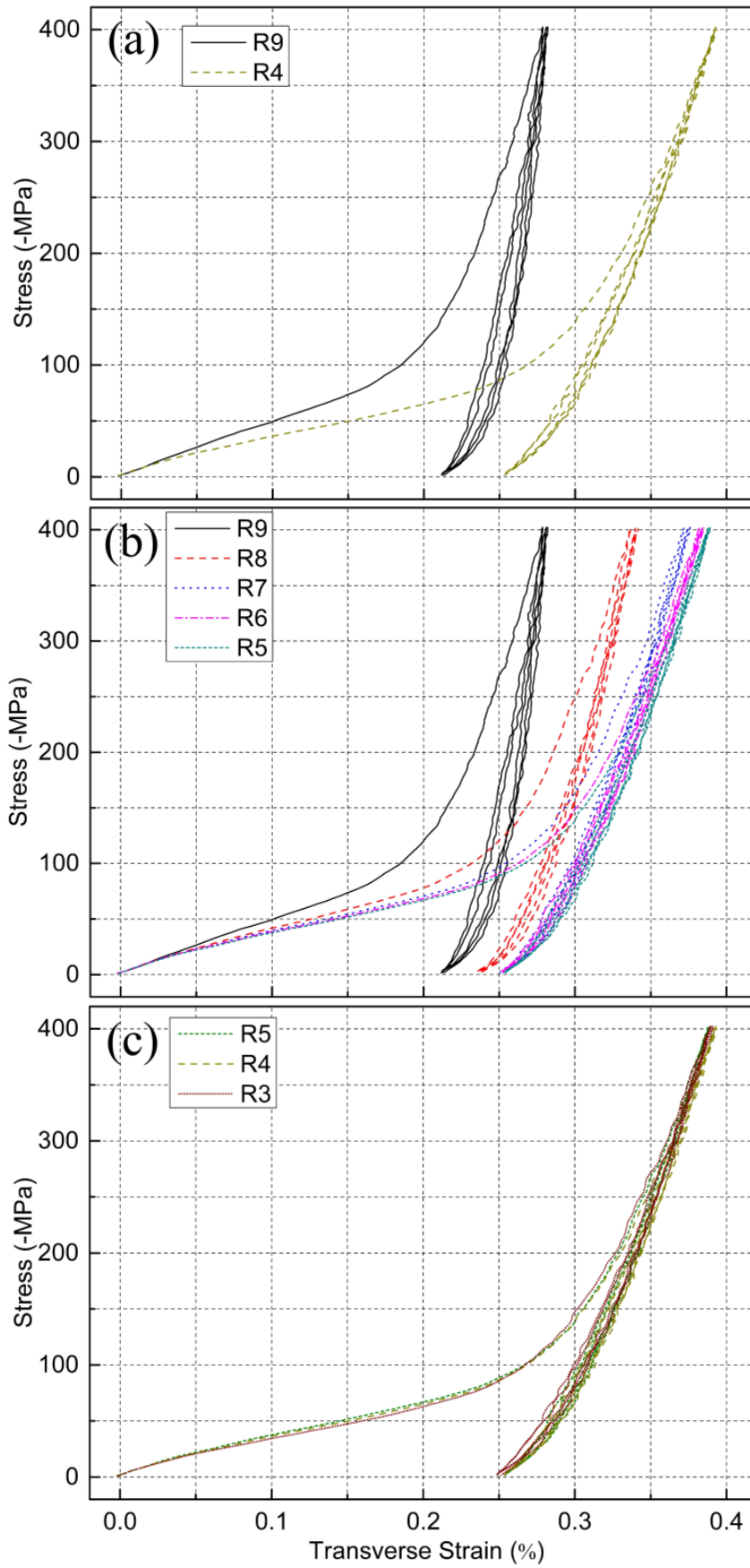


Figure 4.13: Stress-strain curves obtained from various ROIs.

Figure 4.12 demonstrates regions R3 through R9 chosen to monitor the extension and shrinkage along the transverse, i.e. x-direction. R4 is situated in the central part of the whole ceramic body (Figure 4.12 and Figure 4.8). R3 and R5 are placed symmetrically about R4, and they three are still in the central cubic region of the whole sample, approximately. From R6 to R9, the positions get closer to the bottom edge, gradually, so the transverse strains can be obtained at different positions along the y-direction. The comparisons of the strain results calculated from the various ROIs are shown in Figure 4.13.

Figure 4.13(a) demonstrates the transverse strains from the bottom part (R9) and central part (R4) of the ceramic sample. A large difference can be found between the two curves. Due to friction between the ceramic specimen and metal platform, the bottom part of the sample is clamped in the horizontal direction during the loading so that the transverse strain response at the bottom of the sample is much smaller than in the part far away from the bottom. To further investigate this effect caused by the friction constraint, more ROIs were selected on the same surface. It is obvious that, in Figure 4.13(b), the farther the ROI is away from the bottom edge, the larger transverse strain response can be measured. In other words, the deformation from R6 to R9 corresponding to the bottom third of the sample shows an inhomogeneity under the compression testing. However, the inhomogeneity of the deformation does not spread over the entire sample. In Figure 4.13(c), the stress-strain curves for R3, R4 and R5 match each other very well, with little difference among them. The ROIs of R3 to R5 are located around the central cubic region of the sample. Therefore, this region underwent homogenous deformation, and the uniaxial stress-strain results from this part of the specimen are the desired data to develop constitutive models. Due to the symmetry of the uniaxial stress and the geometric shape of the sample, the deformation behavior of the region close to the top edge would be similar to the bottom part.

4.2.4 Spatial distribution of the strain components

Checking the strains in various ROIs by using code I to obtain a strain field on a surface is not the most efficient way. In this section, the strains are calculated by interpolating displacements using finite element shape function [179] which was introduced in section 3.3 on the code II. Although a large subset size (150 by 150 pixels) and step size (50 by 50 pixels) are used here, the spatial distributions of the strain components of the whole surface are still more local than computing an average strain in the ROIs marked in Figure 4.12. The distributions of both the transverse and shear strains are depicted in Figure 4.14, Figure 4.15 and Figure 4.16. Meanwhile, the time instants during the external compressive loading are marked to show at which stress state the strains are obtained.

Figure 4.14 shows the contour plots of transverse and shear strains at 0 MPa (initial state). Despite of the noise in the plots, both show 0% of strain. By comparing the results from Figure 4.14 and Figure 4.16, it can be found that the values of shear strain are almost zero up to an error of $\sim 10^{-2}\%$, while a remnant transverse strain on the order of 0.2% ($\sim 10^{-2}\%$ error) can be observed after the first cycle of loading and unloading. Owing to the mechanical restriction by friction, it is obvious to see in Figure 4.15 that the transverse strain at the bottom is much smaller than that in the upper part of the image which shows the central part of the specimen. This matches the results in Figure 4.13 well. The shear strain presents positive and negative values. However, in view of the error magnitude of $\sim 10^{-2}\%$, the values measured here are suitable for a qualitative discussion, only. The existence of both the positive and negative shear strains in the left and right bottom corners, respectively, in Figure 4.15 is fully consistent with the former discussion on the transverse strains in the context of Figure 4.13. These shear strains occur in the transition zone between the area of constrained transverse strains at the bottom and fully unconstrained transverse strains in the center of the specimen. The absence of shear strains in the center of the specimen confirms the presence of perfectly uniaxial stress and strain state there. It is also interesting to note that, up to measurement accuracy, no shear strains are observed in Figure 4.16 even at the bottom of the specimen. This leads to the conclusion that the remnant strain state shows almost no barreling, while the barreling effect is constituted by elastic strains, in the first

place. This can also be confirmed by comparing in Figure 4.13(a) the transverse strain values at maximum stress to those in the unloaded state, where the difference between R4 and R9 is much larger in the former case than in the latter.

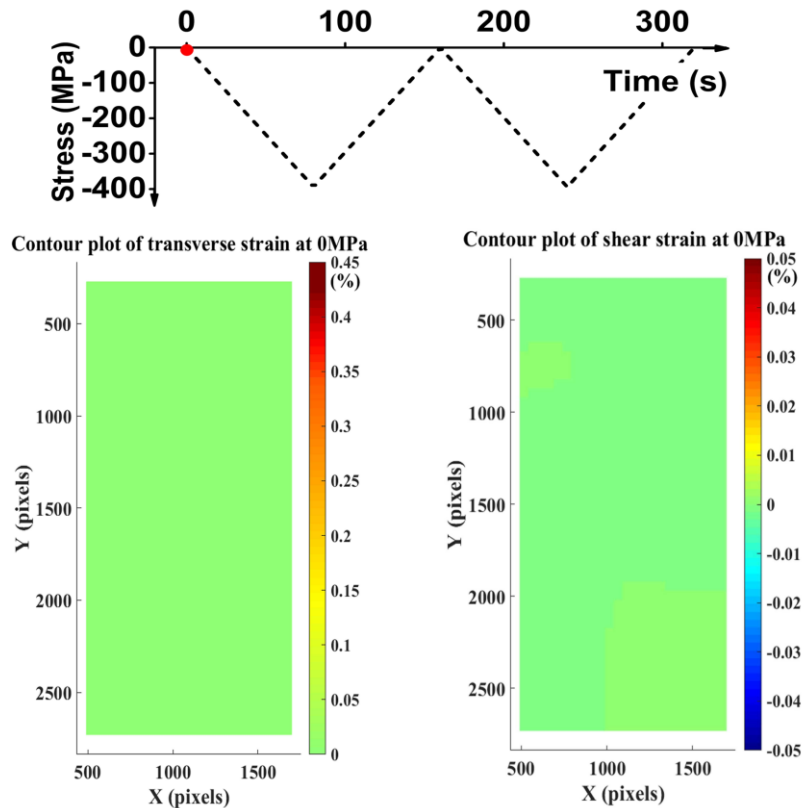


Figure 4.14: Contour plots of transverse and shear strains at 0 MPa. The plot in the upper shows the prescribed stress loading history. The red point denotes at which state of the loading history the corresponding image was taken.

Figure 4.17 demonstrates the schematic representation of the deformation states. Three as-deformed states are plotted, only the last state in Figure 4.17(d) matches the former discussions. However, this figure doesn't represent the exact as-deformed shape but provides a simplified view. The inhomogeneity phenomenon is common in mechanical compressive testing owing to the existing of friction at the interfaces. By using the DIC method, the experiment shows direct evidence for the so-called barreling behavior of PZT ceramics under uniaxial compressive load. The inhomogeneity of deformation close to mechanically loaded surfaces should not be neglected. There are two standards for conducting compression tests on ceramic specimens: C1424-15 from ASTM (American Society for Testing and Materials) [180] and BS (British Standards) EN 658-2:2002 [181]. Both of them provide recommendations on the geometry of specimens for compressive tests. Bone-shaped specimens are recommended because a sample with this shape ensures that the center part represents a purely uniaxial stress state. In these standards, the ratio between the "calibrated length" (the part of the test specimen which has uniform and minimum cross-section area) and "square section side length" (width of calibrated length) is around 2:1, but the ratio between the total length and square section side length is close to 3:1. In addition, the locations for gluing strain gauges are given, too. However, it is not always possible to process the specimens into the bone shape, especially for laboratory-made specimens. For brick shaped samples, the aspect ratio of the specimen and the area where the strains are measured should carefully be considered in order to obtain a true uniaxial stress-strain curve.

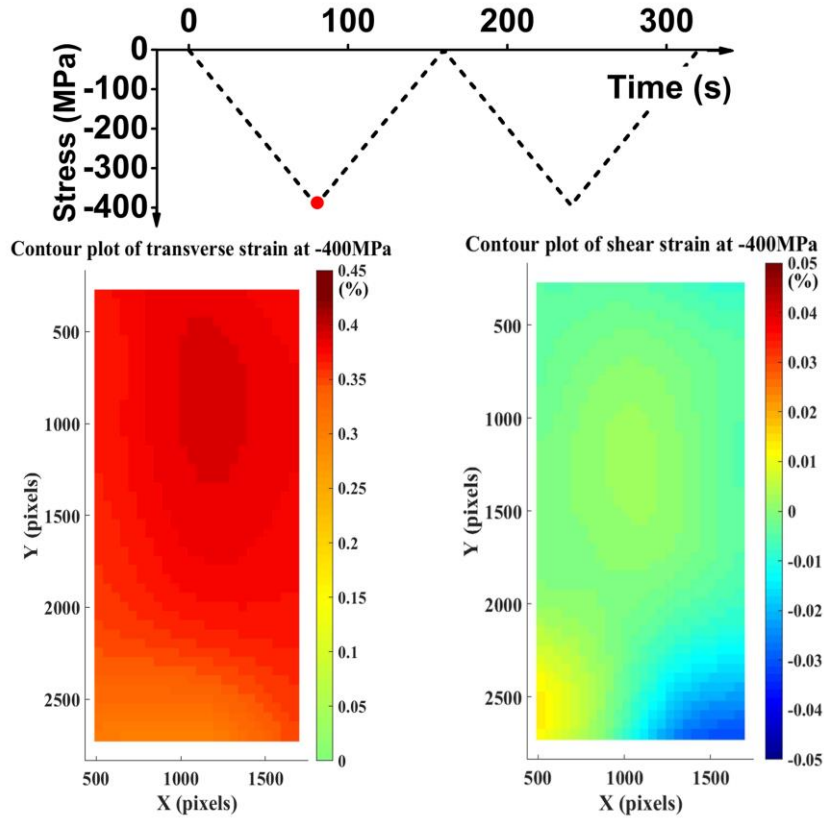


Figure 4.15: Contour plots of transverse and shear strains at -400 MPa.

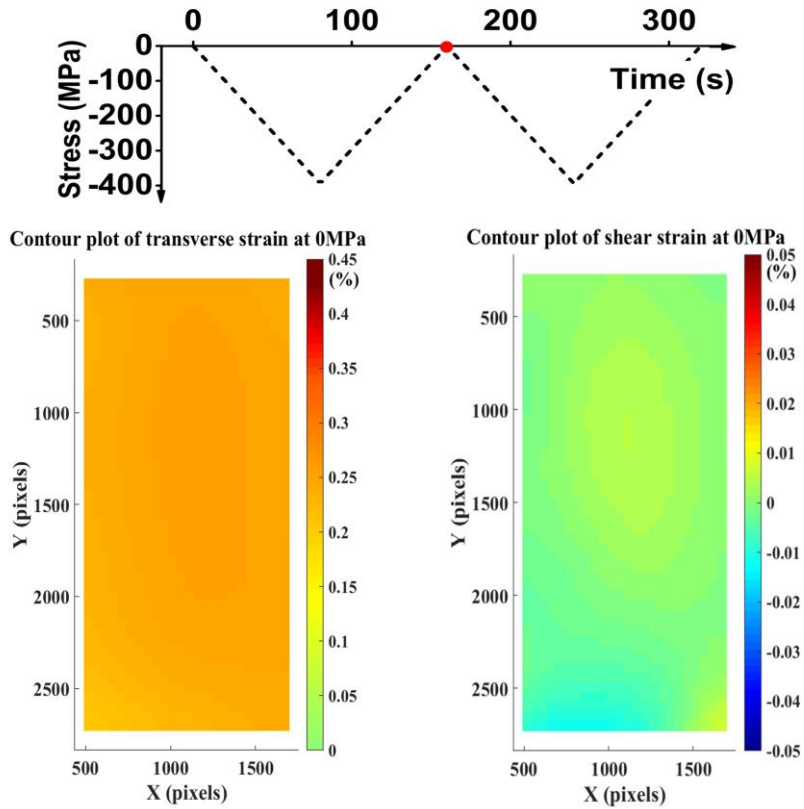


Figure 4.16: Contour plots of transverse and shear strains with the stress unloaded at 0 MPa.

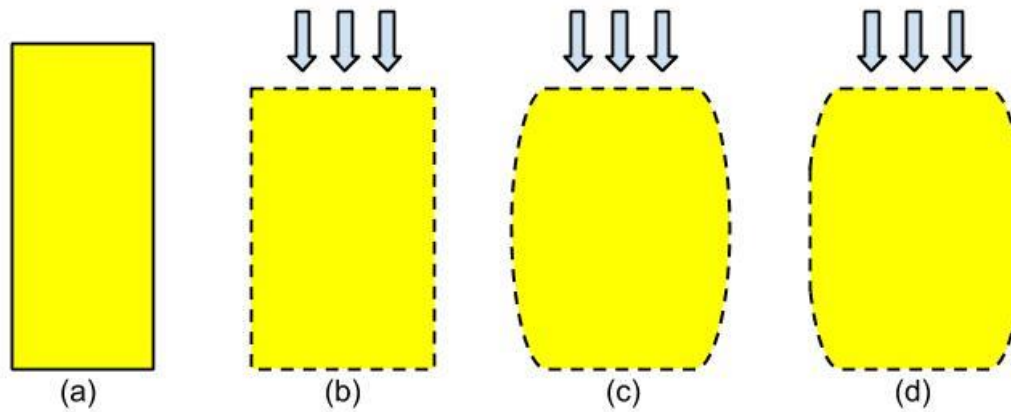


Figure 4.17: Schematic representations of the deformation states: (a) initial state without any compressive load; (b), (c) and (d) three hypotheses of as-deformed states.

4.3 Summary

In the chapter, the DIC method was employed to monitor the deformation of PZT specimen.

In section 4.1, both the longitudinal and transverse strains can be obtained from the same correlation calculation under a uniaxial electric field. LVDT data were used to compare to the longitudinal strain obtained from the DIC method. The results matched well and, thus, the DIC method was validated. The accuracy of the measurement was estimated by calculating the reference images and the accuracy was confirmed again by DIC displacement gauge checking.

The distribution of strain at two particular electric field values were plotted to describe the deformation behavior. This investigation proved that the deformation of PZT ceramic under uniaxial electric field loading without any mechanical constraints is homogeneous under the observing scale in this experiment. This finding was also confirmed by focusing on correspondingly selected ROIs and calculating the values of strain components there.

In section 4.2, the DIC method was used to study the deformation of PZT under uniaxial compressive loads. By using a Sawyer-Tower circuit, the depolarization under compressive loadings was obtained as well. The average strain components can be gained by focusing on correspondingly selected ROIs which can be located anywhere on the observation surface. In addition, the distribution of strains is obtained by contour plots. Based on this technique, barreling behavior under a uniaxial compressive load was proved. This barreling behavior is due to elastic strains, in the first place, while the remnant strains are less affected by this phenomenon. This finding is the experimental justification for the selection of an aspect ratio of 3:1 for our specimens, where only the region close to central cube of the specimen represents the purely uniaxial stress state. To get a desired stress-strain curve, the area on which the measurement is focused should be carefully considered.

5 Experiments on NBT-7BT under electric field loadings

As introduced in Chapter 1, (1-x)NBT-xBT is a family of lead-free piezoceramics with appealing replacement for lead-based materials in actuator applications due to its typically large piezoelectric coefficient and normalized strain S_{\max}/E_{\max} [8]. This NBT-BT solid solution has been shown to exhibit useful piezoelectric properties of compositions that are formulated near the morphotropic phase boundary (MPB) between the rhombohedral NBT and the tetragonal BT phase where $x=0.06\sim 0.07$ [72-74]. Therefore, many investigations have been focused on NBT-6BT and NBT-7BT. In this chapter, experiments of electric field loadings on NBT-7BT are reported to extend the knowledge of the electromechanical properties of this material [182].

5.1 Polarization and strain responses under bipolar loadings

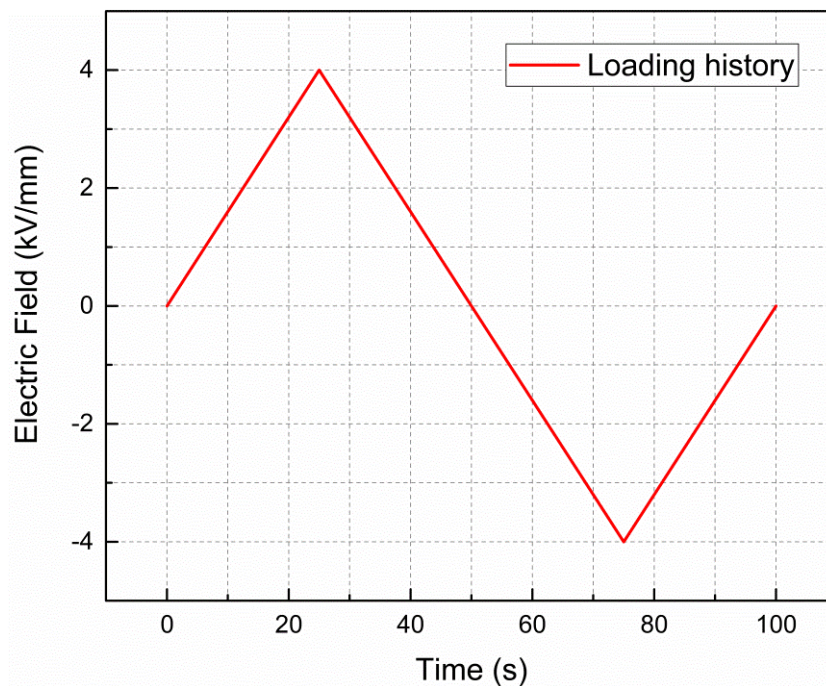


Figure 5.1: Loading history for one cycle of electric field loading.

Figure 5.1 illustrates the loading history for one cycle of the electric field loading. The subsequent loadings repeat this history for several times to reach the designed number of cycles. The loading and unloading rate was controlled at 0.01Hz for both the first loading cycle and the followings with the maximum electric fields of ± 4 kV/mm. The polarization was measured by a Sawyer–Tower circuit combined with an electrometer, while the longitudinal strain was recorded by a LVDT and a digital camera, simultaneously.

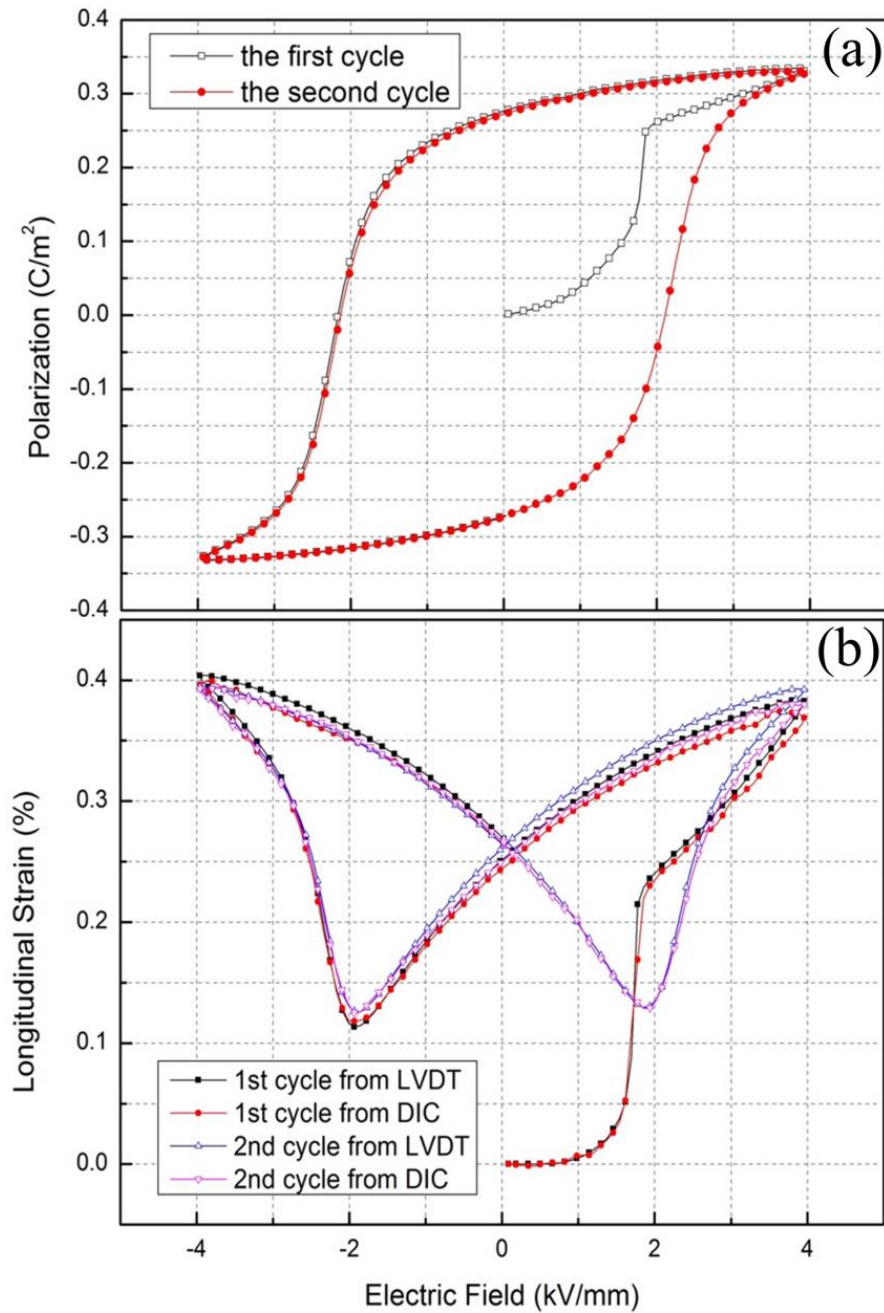


Figure 5.2: Polarization and strain hysteresis loops induced by cyclic electric field loading: (a) polarization hysteresis loops; (b) longitudinal strain curves.

The P - E loops and S - E curves are shown in Figure 5.2. Both the P - E and S - E curves demonstrate large remnant values after the first half cycle of electric field loading. Following additional cyclic electric field loading, the large remnant strain in Figure 5.2(b) remains unchanged. This behavior has been described as an irreversible transition from the non-ergodic RE state to the long-range FE state [54]. Furthermore, while a sufficient electric field is necessary to drive this phase transition it is irreversible even if the electric field is removed totally. Compared with the strains measured by using the LVDT and DIC methods, the results match each other well validating the DIC method once again.

5.2 Electromechanical responses under a constant electric field

In section 1.3.4, electric field-induced phase transition in NBT-BT has been reviewed. However, all those investigations were performed under varying electric field loadings. Not many experiments under a long-term constant electric loading on the lead-free piezomaterials were reported. Unlike the electric field-induced electromechanical responses in PZT materials which were attributed to ferroelectric domain switching processes [153, 183], the lead-free NBT-BT system exhibits a phase transition from RE to FE corresponding to the change from an unpoled to a poled state. This change influences the macroscopic performance strongly. Whether this phase transition can be induced by a static electric loading is still unknown. Therefore, the electromechanical behavior of virgin polycrystalline NBT-7BT induced by a constant electric field was investigated to explore the time-dependent RE-FE transition behavior.

5.2.1 Experimental procedures

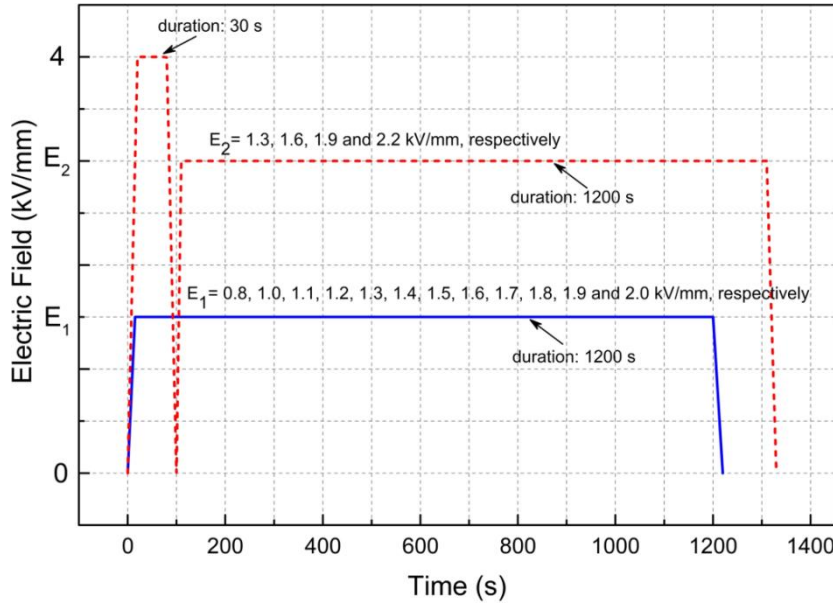


Figure 5.3: Two loading histories applied to the NBT-7BT specimens.

NBT-7BT specimens in an initially unpoled state were selected to perform the experiments. The time-dependent electromechanical response was recorded during unipolar constant electric fields. The loading history was applied on the specimens, as shown in Figure 5.3. Both, loading and unloading were controlled at a rate of $0.16 \text{ kV/mm s}^{-1}$ (0.01 Hz). In the first loading scenario, E_1 was applied to an unpoled sample and held constant for 1200 s for selected maximum electric fields between 0.8 kV/mm and 2.0 kV/mm (shown by the blue solid line in Figure 5.3). Following the holding time and electrical unloading, the piezoelectric coefficient d_{33} was estimated by means of averaging the strains induced by a triangular electric field between 0.0 and 0.2 kV/mm with a frequency of 0.5 Hz for 5 cycles. In the second loading scenario, the unpoled specimen was initially electrically poled at 4.0 kV/mm for 30 s. Following this, the samples were loaded to E_2 with values of 1.3, 1.6, 1.9 and 2.2 kV/mm, respectively. The hold time was also 1200 s (red dashed line in Figure 5.3). The longitudinal strain and polarization were recorded during the complete loading history for both scenarios.

5.2.2 Results and discussions

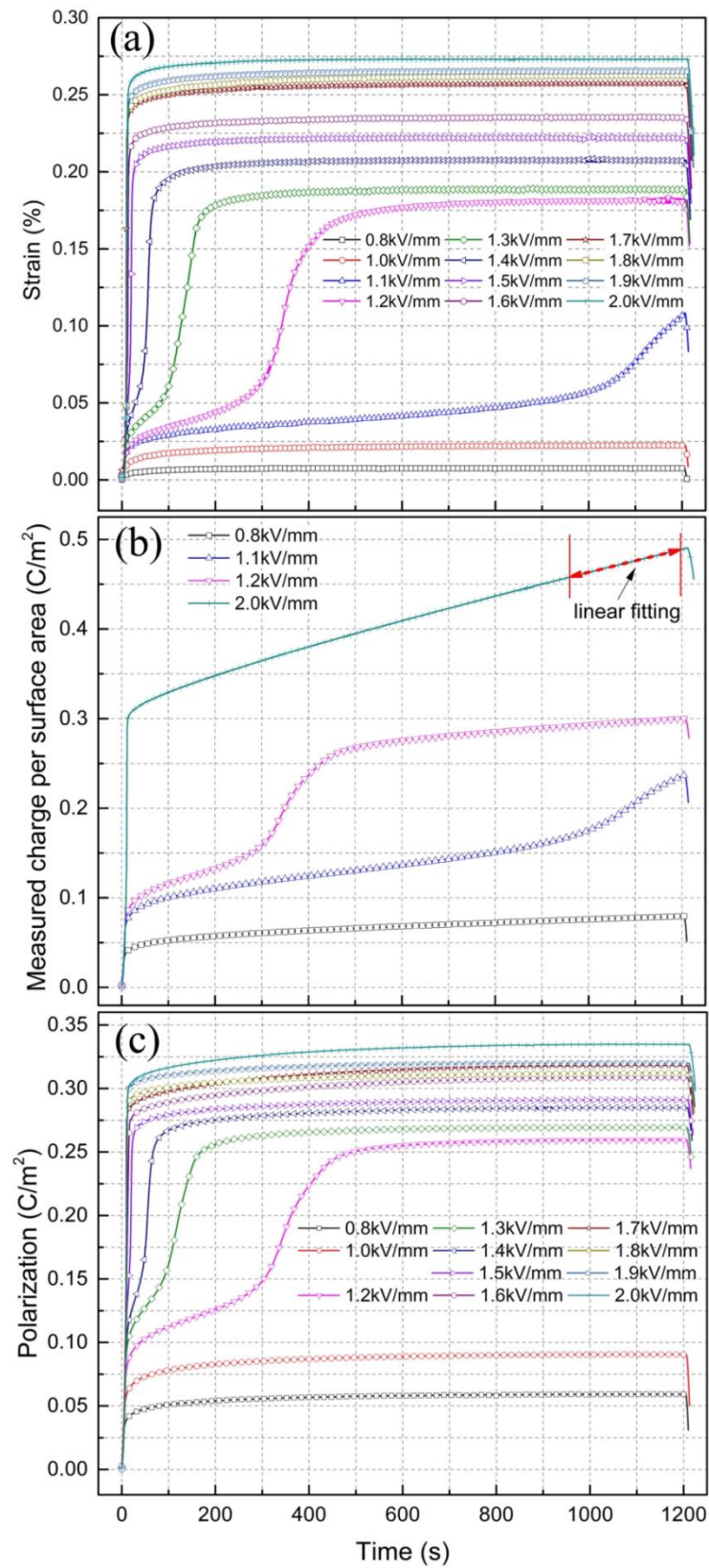


Figure 5.4: Longitudinal strain and polarization as a function of time: (a) measured strains; (b) measured charge per specimen surface area including charges from leakage; (c) polarization under various static electric fields.

Longitudinal strain and polarization as a function of time were measured under various constant electric field magnitudes, shown in Figure 5.4. Unlike the strain curves in Figure 5.4(a) where eventual saturation occurs, the measured charge per surface area in Figure 5.4(b) does not show saturation during the 1200 s hold time. Instead, this curve merges into a straight line with a non-zero slope. It is believed that in addition to the polarization charges, charges also caused by a leakage current accumulated in the capacitor of the Sawyer-Tower circuit. Thus, in obtaining Figure 5.4(b) charges caused by leakage current together with the polarization charges contributed to the voltage measured by the electrometer. To exclude this effect and determine the polarization charge response, only, a linear fitting was performed on the linearly increasing section of the measured charge per surface area towards the end of the hold time. The corresponding strain in Figure 5.4(a) is saturated after a sufficiently long time of electric field loading (except for the curve at 1.1 kV/mm), indicating that creep processes must have come to an end, such that the linear increase in the charge measurement can be ascribed solely to leakage currents. Figure 5.4(b) depicts only four charge responses, among which the measured charge per specimen surface area held at 2 kV/mm is taken as an example to show the range of linear fitting. The data obtained in the last 300s of the hold time where the charge shows almost linear increase were selected as the fitting range to calculate the value of the slope. In fact, this fitting was performed on each measurement except for the electric field held at 1.1 kV/mm, because in this case neither the strain nor charge curve presents a saturation stage.

Time-dependent changes in polarization during the application of a bias electric field can be obtained by

$$P = P_m - P_l \quad (\text{Equation 5.1})$$

$$P_l = mt \quad (\text{Equation 5.2})$$

In Equation 5.1, P is polarization without the influence of leakage current, which is shown in Figure 5.4(c), and P_m is the measured charge per specimen surface area, while P_l is the charge per specimen surface area caused by leakage current. P_l can be obtained by using Equation 5.2, which is the slope of the linear fit multiplied by time t . Figure 5.4(c) depicts polarization as a function of time under various static electric fields. It shows saturation behavior comparable to the strain curves.

From Figure 5.4(a) and (c), it can be clearly seen that the electric field-induced electromechanical behavior is time-dependent at electric fields below the poling field (~ 1.8 kV/mm). In addition, the magnitude of the constant electric field significantly influences the electromechanical response. Strain and polarization display two regimes: (i) an instantaneous strain response during the initial dynamic electrical loading, followed by (ii) gradually increasing creep strain during the subsequent holding time, which corresponds the periods of initial electric loading and holding time illustrated in Figure 5.3. When the electric field is not sufficient, i.e., 0.8 and 1 kV/mm, both the strain and polarization do not show large responses that eventually saturate during the holding time. With increasing electric field from 1.2 to 1.6 kV/mm, a two-stage cascade behavior is observed. This phenomenon, however, cannot be observed when the electric field is higher than 1.6 kV/mm. The cascade behavior occurs rapidly under a large electric field, so that the measurement cannot distinguish between the two stages of the response.

These phenomena indicate that the electric field-induced RE-FE transition plays a key role in the time-dependent response. Low electric fields are able to induce only a small amount of material to undergo a RE-FE transformation, resulting in a low polarization and strain value, despite long holding times. Therefore, the time-dependent RE-FE transition requires an external electric field higher than a certain threshold value. In Figure 5.4(a) it can be observed that in the strain response at 1.1 kV/mm includes a gradual creep without saturation, up to 100 s. Between 100 and 1000 s, there is a clear increase in the strain rate, which doesn't saturate. In contrast, the strain curve at 1.2 kV/mm shows a complete electric

field-induced strain evolution towards saturation as a function of time. The instantaneous strain response during the initial electrical loading contains electrostriction as well as strains arising from a field-induced RE-FE transition. When the electric field reaches 1.2 kV/mm (Figure 5.4(a)) and is held, the strain curve exhibits a two-step behavior consistent with measurements at 1.1 kV/mm. The first step, due to rapid electric field loading resulted in a strain and polarization of 0.021% and 0.09 C/m², respectively, similar to the values observed in bipolar hysteresis behavior during initial loading at 1.2 kV/mm (Figure 5.2). During the subsequent hold time both the strain and polarization were found to gradually increase with time. The second step occurred after a hold time of approximately 300 s, which is marked by a sharp increase in strain and polarization. Saturation of this second step was found after approximately 600 s with strain and polarization values of approximately 0.18% and 0.26 C/m², respectively. With an increasing constant electric field level there is a subsequent decrease in the hold time required to observe the second step.

The rapid increase in strain and polarization after a particular holding time can be explained by the nucleation and growth of the FE long-range order state. The newly formed regions with FE order act as polar seeds that can induce more surrounding regions to undergo a RE-FE transition in a cascading manner. To use an analogy, this “self-catalyzed” transition is accumulated into a very fast creep rate on the measured strain. Nevertheless, the total amount of RE that can be induced with this electric field (1.2 kV/mm) is limited. Therefore, the creep rate slows down again gradually with the exhaustion of transformable RE. The inflection point around 400 s appears to confirm this hypothesis. The evolution of the RE-FE transition is not only time-dependent but also electric field-dependent. With an increasing constant electric field, the time to the second step becomes gradually shorter. The cascade effect was not observed when the applied electric field was higher than 1.6 kV/mm, as the field was high enough to induce a complete RE-FE transition during the initial electrical loading. This gradually disappearance of the cascade reveals that the “self-catalyzed” state transition can be accelerated by applying a higher electric field until the poling and cascade behaviors cannot be distinguished.

Figure 5.5 illustrates an example of the strain as a function of time including both the initial and creep portions measured at 1.8 kV/mm. In this figure, the data defined as the instantaneous response and the range of creep response can be observed clearly.

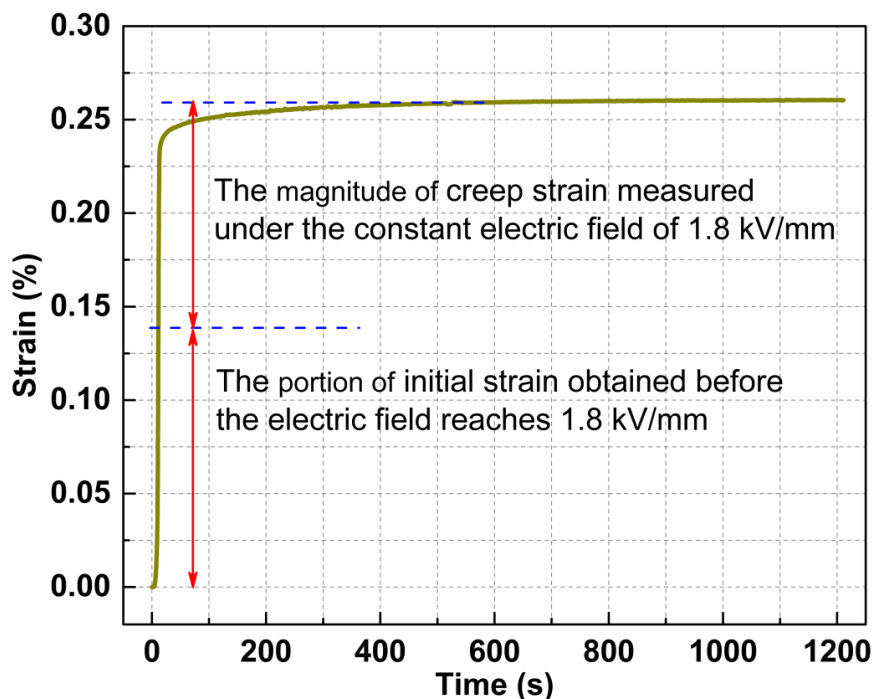


Figure 5.5: Two portions of the strain response measured at 1.8 kV/mm.

These instantaneous responses during the initial dynamic electrical field increase were subtracted from Figure 5.4(a) and (c) to obtain the pure strain and polarization evolution during the hold time at the various constant electric fields. The comparison of these magnitudes of creep strain and creep polarization are plotted in Figure 5.6. It can be seen that the magnitudes of creep strain with saturation states are not directly proportional to the constant external electric field. As previously mentioned, the amount of material able to undergo the RE-FE transformation is limited by the volume fraction of available RE and the magnitude of electric field applied. When large constant electric fields are applied, much of the material undergoes a RE-FE transition during the initial poling process (illustrated by the curve for 2 kV/mm in Figure 5.4(a)), consuming most of the available RE and resulting in a reduced creep strain (see the corresponding value for 2 kV/mm in Figure 5.6). On the other hand, a relatively low electric loading is not sufficient to activate the RE-FE transition; therefore, the creep responses are also small for 0.8 and 1.0 kV/mm. The creep responses at moderate fields between these two levels is larger because the external load is sufficient to induce the RE-FE transition but the exhaustion of the available RE is not reached before the maximum electric field is applied. Although some differences between the creep strain and polarization can be observed, both the two groups of values in Figure 5.6 follow roughly the same tendency. It implies that the time-dependent effects of strain and polarization arise from the same mechanism as has been observed in PZT materials [153].

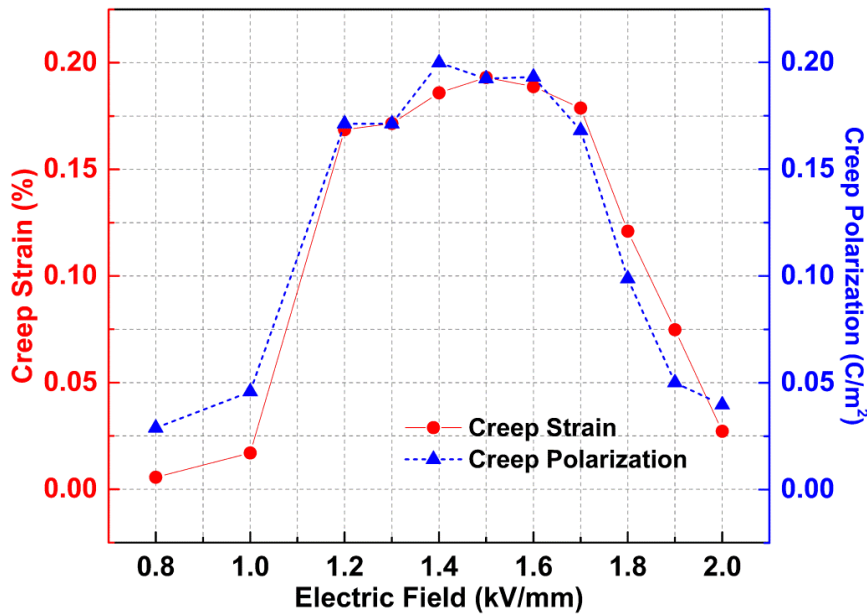


Figure 5.6: Comparison of the magnitudes of creep responses under various constant electric fields.

In order to find the threshold of electric field to activate this phase transition, two more experiments with the static loadings at 1.1 kV/mm were executed. In addition, the magnitude of 1.15 kV/mm between 1.1 and 1.2 kV/mm was selected to further explore this threshold. These results were plotted in Figure 5.7 with the duration of the hold time marked by arrows. In Figure 5.7, the three curves marked as 1.1 kV/mm-01, -02 and -03 show very different time-dependent strain evolution. The curve of 1.1 kV/mm-01 shows an uncompleted cascade phenomenon without eventual saturation which has been mentioned in the discussion of Figure 5.4(a). Interestingly, 1.1 kV/mm-02 does not show a clear increase in strain when held for 1200 s. This experiment was repeated at 1.1 kV/mm (1.1 kV/mm-03) but with a holding time of 1800 s. With an increase in the holding time there is eventually, at approximately 1500 s, the onset of the creep behavior, which even at 1800 s does not saturate. The differences in these results under identical conditions suggest that the electric field-induced strain at 1.1 kV/mm is close to the threshold. Therefore, an experiment at 1.15 kV/mm with a 3600 s holding time was con-

ducted to determine the threshold. This curve is in agreement with the former discussions on the two-stage cascade attributed to the “self-catalyzed” RE-FE transition.

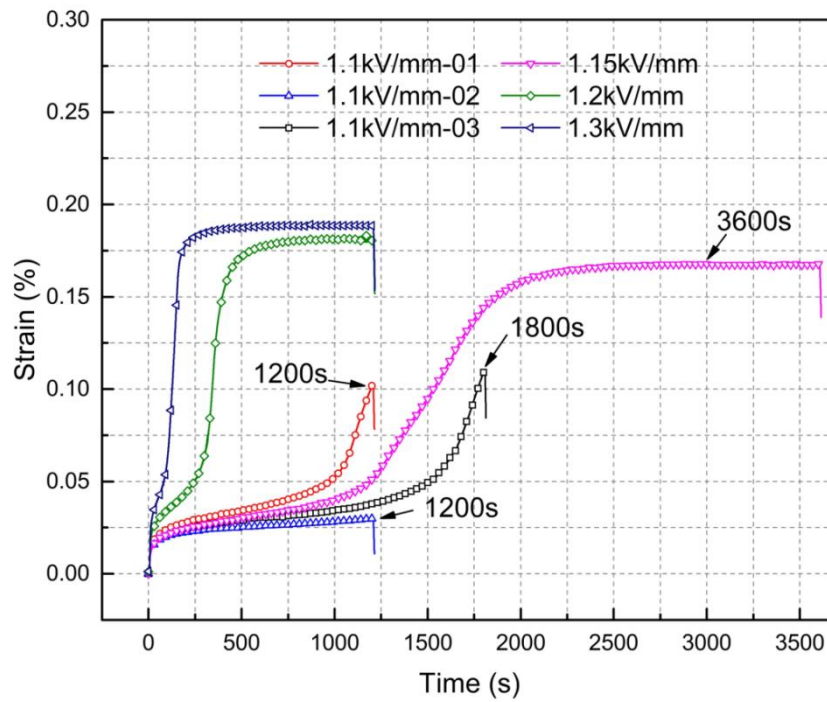


Figure 5.7: Longitudinal strains under three times of the constant electric field loadings of 1.1 kV/mm and under a constant electric field of 1.15 kV/mm with 3600 s holding time.

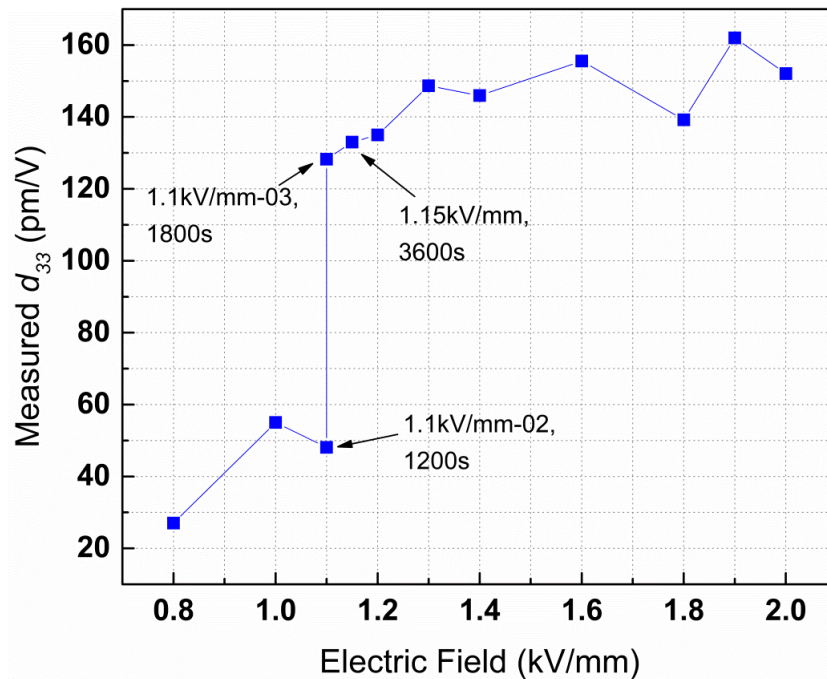


Figure 5.8: Measured d_{33} after various constant electric field loadings.

Following the hold time the d_{33} values were determined by application of an electric field of 0.2 kV/mm (Figure 5.8). These is a clear increase in d_{33} for constant electric field levels at 1.1 kV/mm from approximately 50 pm/V to 128 pm/V. This phenomenon reveals that the structure change induced by

the phase transition not only influences the macroscopic strain and polarization response, but also the piezoelectric properties. Above this electric field level there is a continual increase in d_{33} to approximately 150 pm/V for 2 kV/mm. It is suggested that this d_{33} behavior is related to the RE-FE transition generated during the creep process at a constant electric field loading. Therefore, the d_{33} values can be used to roughly check the completeness of the transition. The saturation state indicates the exhaustion of the available RE phases and the completion of the transition under this electric field. Therefore, no further significant change can be observed for the values of d_{33} .

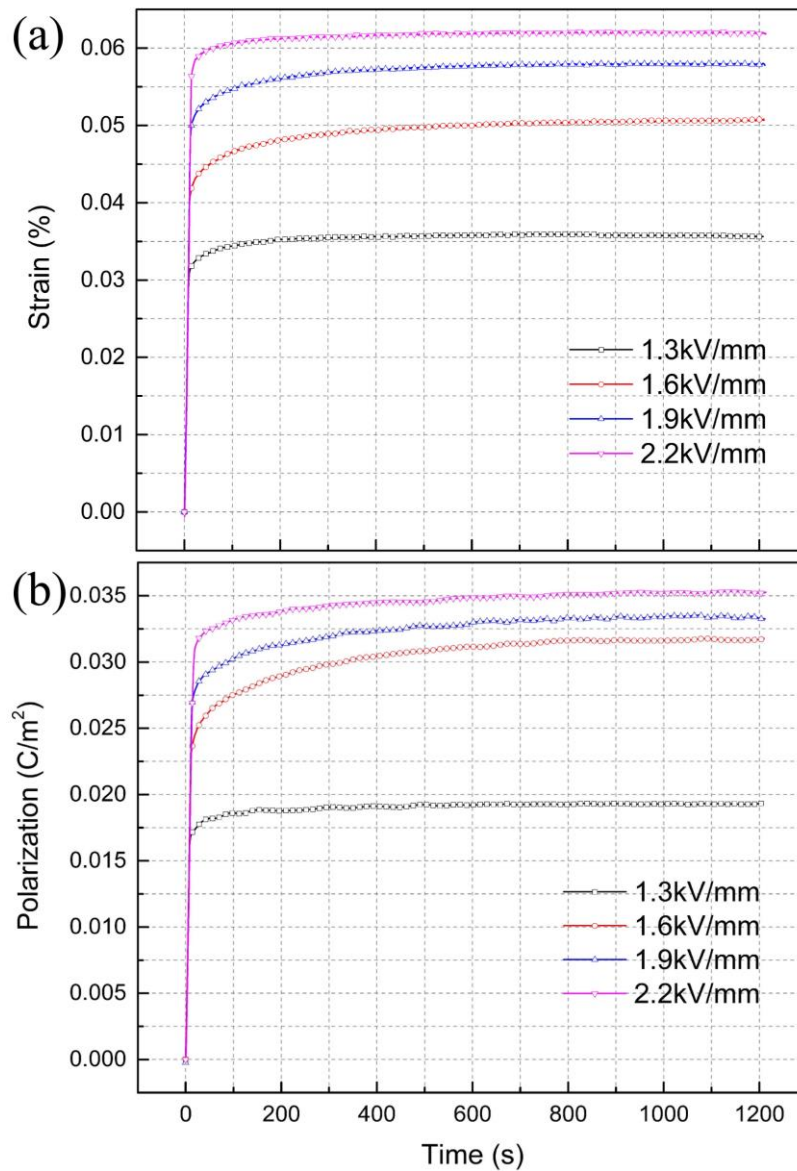


Figure 5.9: Longitudinal strain (a) and polarization (b) as a function of time measured on poled specimens.

Figure 5.9 shows strain and polarization (after subtracting leakage) as a function of time measured on poled specimens (poling field was 4 kV/mm, shown by red the dashed curve in Figure 5.3). Unlike the unpoled specimens, the RE has been transformed into FE irreversibly in these poled specimens at room temperature. As a result, the two-stage cascade phenomenon cannot be found. This time-dependent macroscopic behavior of the poled samples is similar to PZT materials which are dominated by gradual FE domain switching processes, only [153, 183].

5.3 Summary

In this chapter, experiments of electric field loadings on polycrystalline NBT-7BT specimens are reported. Especially, the time-dependent electromechanical response of these specimens induced by a constant electric field was investigated. For the specimen with an initially unpoled state, the evolution of the electric field-induced strain and polarization depend on both the hold time duration and the magnitude of the constant electric field. A relatively low electric field is not sufficient to activate a RE-FE transformation. The electric field required to induce a macroscopic response was determined to be at approximately 1.1 – 1.15 kV/mm. Externally applied electric field of 1.1 kV/mm or higher were found to induce a so-called “two-stage” cascade phenomenon for sufficient holding times. This cascade behavior under a proper constant electric field provides evidence that the electric field-induced RE-FE transition is a “self-catalyzed” behavior, namely, newly formed FE induces more RE to transform. The rate of this cascade development depends on the magnitude of the applied electric field. Owing to the irreversible nature of this transition, the cascade phenomenon cannot be observed on poled specimens.

6 Experiments on NBT-6BT-3KNN under electric field loadings

The NBT-BT-KNN ceramic system is a promising lead-free material for actuator applications owing to its giant electric field-induced strain [85, 115]. The previous introduction in section 1.3.4 has mentioned that its giant strain at room temperature is understood to be due to a reversible phase transition between RE and FE induced by a sufficient electric field [97]. To understand the electromechanical behavior of NBT-6BT-3KNN ceramic, electric field-induced strains are investigated in this chapter. Especially, the creep behavior of NBT-6BT-3KNN induced by a constant electric field is discussed. Approximate values of volume resistivity were obtained to eliminate the influence of leakage currents on the polarization measurement. Both of polarization and strain exhibit time-dependent effects upon the application of a constant electric field consistent with a time-dependent transformation from the RE state to a long-range ferroelectric order. These results are helpful to understand the creep phenomena, which in turn provide a basis for improving the performance and reliability of lead-free piezoactuators. Following the experiments in section 5.1, this work was also conducted in the same setup under the same loading history. Therefore the experimental procedures are not introduced in details here.

6.1 Polarization and strain responses under bipolar loadings

Figure 6.1 demonstrates the P - E hysteresis loops and S - E “sprout”-shaped curves of NBT-6BT-3KNN induced by cyclic bipolar electric fields. Unlike the P - E and S - E curves measured from NBT-7BT shown in Figure 5.1, these two measurements in NBT-BT-3KNN exhibit little remanence explained by its ergodic RE property. This ergodic RE behavior was reviewed in section 1.3.4, where the function of adding KNN into NBT-BT was introduced. Both the depolarization temperature (T_d) and the ferroelectric-to-relaxor transition temperature (T_{F-R}) of the NBT-BT solid solution system can be adjusted by adding KNN. By means of controlling the composition of NBT-BT-KNN, the T_{F-R} of the ceramic can be reduced slightly below room temperature [91]. Therefore, NBT-6BT-2KNN is transformed from RE into FE reversibly under a sufficient electric field at room temperature. This concept is also suitable for NBT-6BT-3KNN. Compared to NBT-6BT-2KNN, the NBT-6BT-3KNN specimens used in this work contain more KNN leading to an ergodic RE behavior, too [75]. The slim and pinched P - E loops in Figure 6.1(a) indicate this ergodic RE behavior featured by little remanence. The electric field-induced strain reaches 0.18% when the electric field is applied to 4 kV/mm. The P - E and S - E curves do not show saturation backing the discussion in section 1.3.5.2 that the NBT-based ceramic requires a high poling field usually higher than 4 kV/mm.

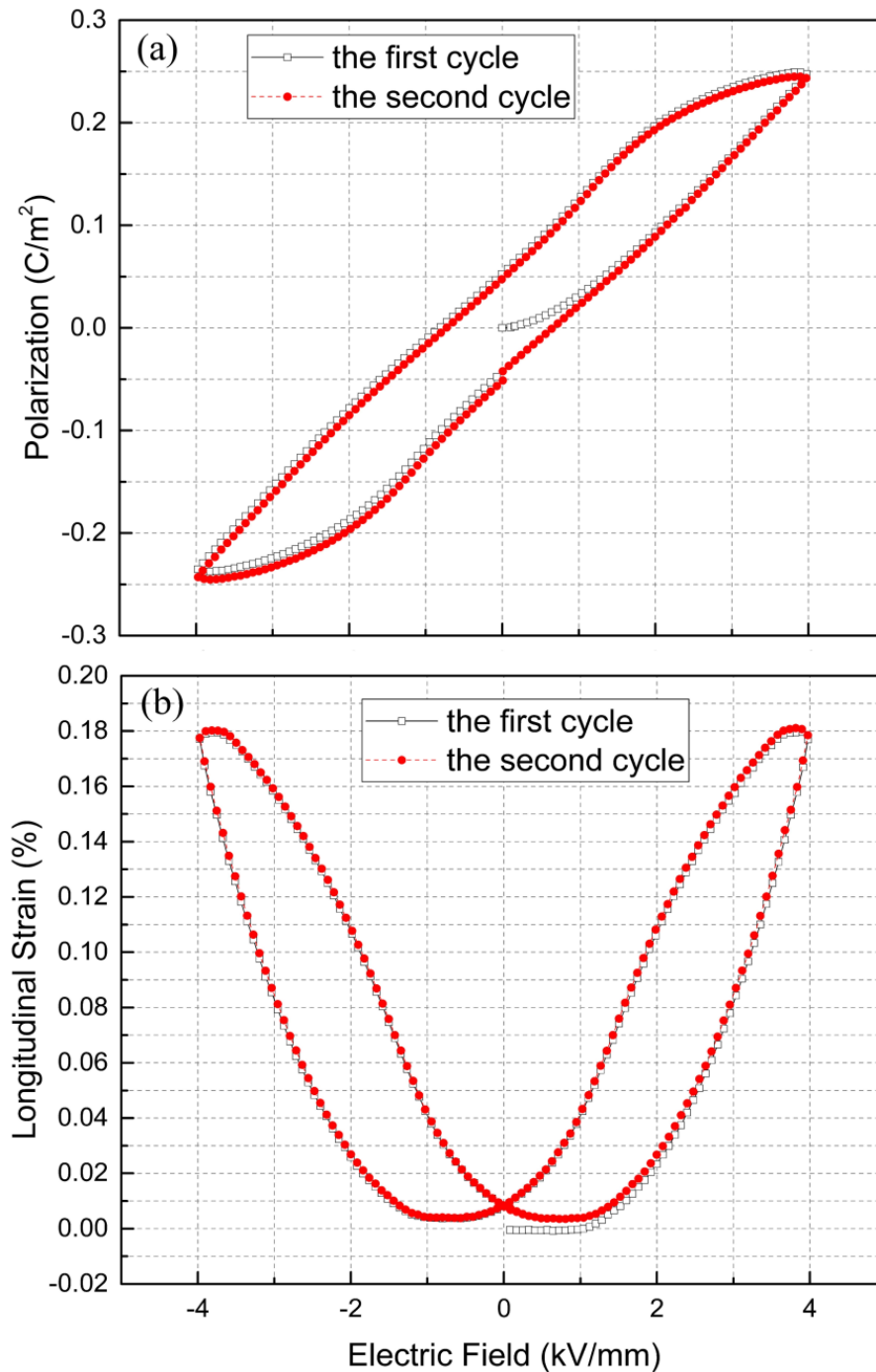


Figure 6.1: Polarization and strain hysteresis loops of NBT-6BT-3KNN induced by cyclic electric field loading: (a) polarization hysteresis loops; (b) longitudinal strain curves.

6.2 Electromechanical responses under a constant electric field

Most investigations to date have been performed under varying electric field loading to determine the macroscopic strain response. The creeping of strain and polarization, however, under a constant electric field remains largely uninvestigated in lead-free materials. For lead-based materials, Zhou and Kamlah [153] investigated the creeping of PZT under bipolar quasi-static electric fields with various hold times. The observed creeping was ascribed to gradual ferroelectric domain switching processes. Liu and

Huber measured the creep behavior under unipolar constant electric fields and provided a model to describe the creep [183]. For the NBT-BT-KNN family, piezoresponse force microscopy (PFM) was used to conduct time-dependent relaxation measurements to reveal the reversibility of the field-induced FE phase as a function of KNN content [4]. However, macroscopic measurements on the time-dependence of strain and polarization for NBT-BT-KNN have not been reported. To investigate the influence of creeping on the electromechanical behavior of ergodic RE, the strain and polarization creep behavior of NBT-6BT-3KNN specimens is characterized during a constant electric field loading.

6.2.1 Experimental procedures

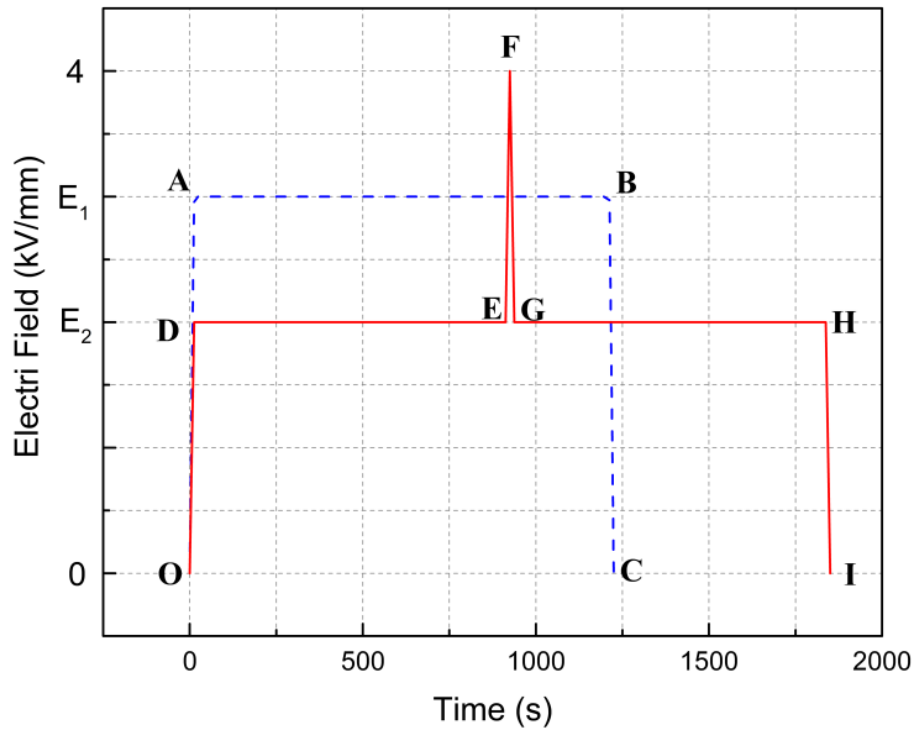


Figure 6.2: Two loading histories applied to the specimens of NBT-BT-3KNN.

Following the experiments of a constant electric field applied to NBT-7BT samples, the similar procedure are taken here. During measurement, NBT-BT-3KNN specimens were subjected to unipolar bias electric fields. Two different loading histories were applied, shown schematically in Figure 6.2. In these experiments, both the loading and unloading rate was $0.16 \text{ kV/mm s}^{-1}$. In the first loading scenario, E_1 was 1, 2, 3, or 4 kV/mm and held constant for 1200 s, denoted by line AB. Following this hold time, the sample was electrically unloaded to 0 kV/mm. In the second loading scenario, E_2 was either 1, 2 or 3 kV/mm and held for 900 s, as denoted by line DE. Following this hold time, the sample was electrically loaded to 4 kV/mm, followed by an immediate unload back to the original bias electric field, where it was held for another 900 s, denoted by line GH. Finally, after the second hold time, the sample was unloaded to 0 kV/mm. The longitudinal strain and polarization were characterized during the complete loading for both scenarios.

6.2.2 Results and discussion

Figure 6.3 demonstrates the changes of both longitudinal strain and polarization as a function of time for the first loading scenario. Both strain and polarization exhibit significant time-dependent effects upon the application of a constant electric field. Similar to the loading history in NBT-7BT, the strain

result in Figure 6.3(a) also includes two regimes discussed in section 5.2.2. An instantaneous strain response induced by the initial electrical loading is the first stage. Followed by the subsequent holding time, a gradual increase in the measured strain and eventual saturation can be observed. The strain grows rapidly during the first period and then shows a creep behavior under the constant loading. During the long hold time, the creep is reduced gradually and eventually reaches a final saturation value. However, the polarization curves in Figure 6.3(b) do not show saturation during the 1200 s hold time. The same phenomenon was recorded on the NBT-7BT sample used in section 5.2.2, and the discussion was made there. Due to leakage current, charges accumulated in the capacitor of the Sawyer-Tower circuit, thus, together with the polarization charges contributed to the voltage measured by the electrometer. Using the Sawyer-Tower circuit, it is assumed that the piezoceramic material is a capacitor with good insulating properties so that the measured charge is due to polarization only and not affected by any charges caused by leakage. In the present measurement, when applying high voltages for a long hold time, the leakage current contribution to measured charges cannot be ignored. To exclude this effect to determine the polarization charge response, a linear fitting operation was performed on the linearly increasing sections of the measured polarization towards the end of the hold time. In Figure 6.3(b), the measured charge per specimen surface area under static loading at 4 kV/mm is taken as an example to show the linear fitting area. The data obtained in last 300 s are selected as the fitting range to calculate the value of the slope. This area has been selected because the corresponding strain in Figure 6.3(a) is saturated in this regime, indicating that creep processes must have come to an end, such that the linear increase in the charge measurement can be ascribed solely to leakage currents. The same operation has been provided in section 5.2.2.

After performing this operation on all four curves in Figure 6.3(b), the values of slope in the fitted areas can be obtained. Then, the volume resistivity ρ can be calculated by

$$\rho = \frac{E}{m}, \quad (\text{Equation 6.1})$$

where E represents the static electric field applied and m is the slope of the linear fit as introduced in Equation 5.1 and 5.2. The experiments under the constant electric field loadings were repeated three times and the average results are listed in Table 6.1. The leakage at the electrometer is neglected due to the large input resistance of the device (Keithley 6514 with $1\text{T}\Omega$ input-resistance). For some commercial PZT materials, the values of resistivity at room temperature are $\sim 10^{10} \Omega\cdot\text{m}$ for PZT-4 or PIC141, and $\sim 10^{11} \Omega\cdot\text{m}$ for PZT-5H or PIC151 [184, 185]. The variation of this value depends on the composition as well as types of dopant and dopant concentrations of the material. The observed values of volume resistivity in Table 6.1 are found to be a nonlinear function of the applied high electric field. Usually, volume resistivity is measured under a relative small voltage of ~ 500 V based on the recommendation from ASTM D257 standard [186]. This recommended value is less than 0.2 kV/mm if the thickness of the ceramic specimen ~ 2.7 mm is used in this experiment. However, the actual electric fields ranging from 1 to 4 kV/mm used to perform this experiment are far beyond the value of 0.2 kV/mm. Under these strong electric fields, the volume resistivity is hard to keep a constant anymore. In Table 6.1, the higher the constant electric field was applied, the smaller value of resistivity was obtained. According to the knowledge of solid state physics, strong electric fields can induce ionization in dielectric materials [187], so the reason for the change in resistivity of NBT-6BT-3KNN could be attributed to the degree of strong electric field-induced mobility of charge carriers under different static electric fields [188]. Many other materials show a similar response upon application of a large electric field, including some nonpolar insulators. In this work, the measured volume resistivity under large electric fields can be used to eliminate the influence from the leakage currents, but the further physical consideration is not discussed here owing to lacking of more experimental data on this type of material.

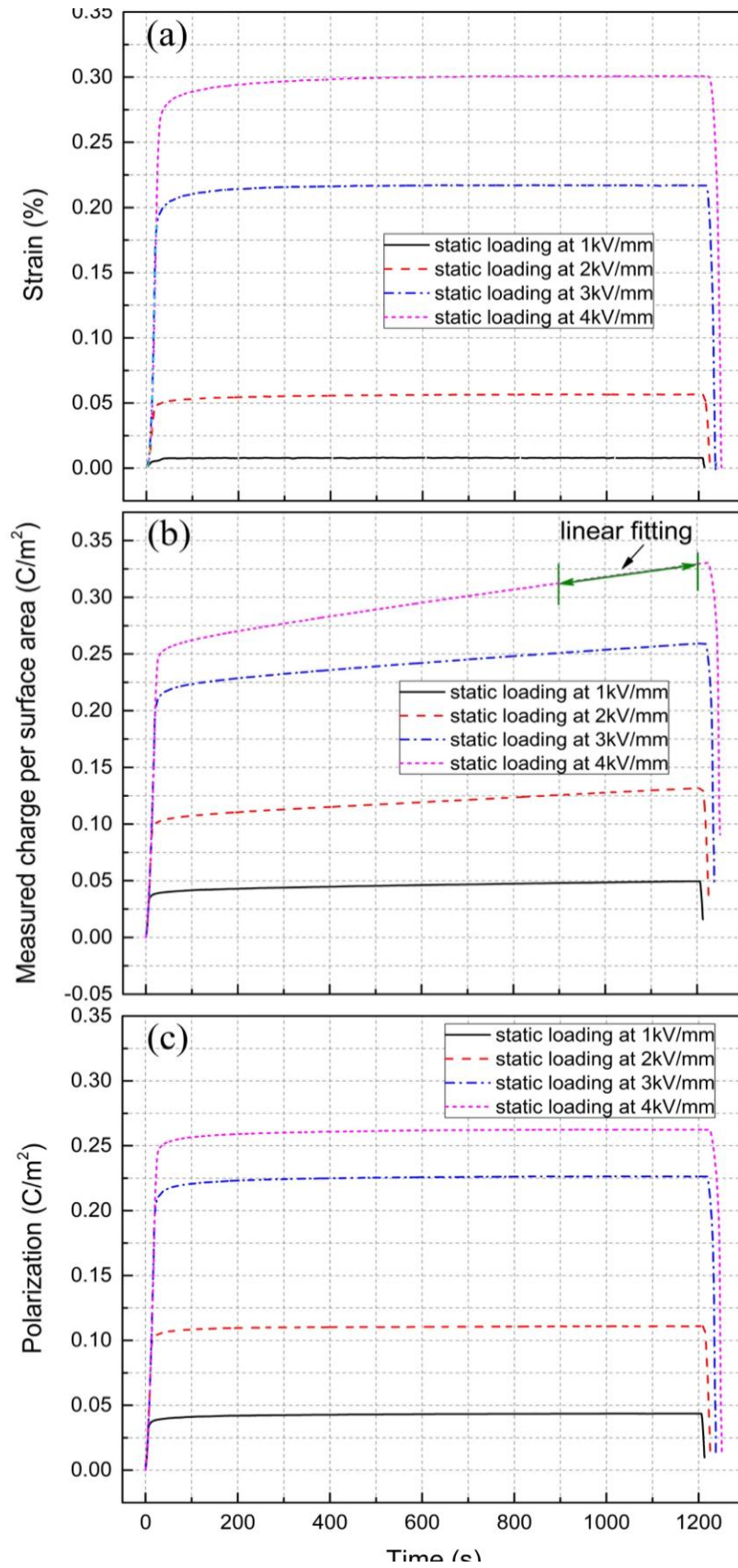


Figure 6.3: Longitudinal strain and polarization as a function of time: (a) measured strains; (b) measured charge per specimen surface area including charges from leakage; (c) polarization as a function of static electric fields.

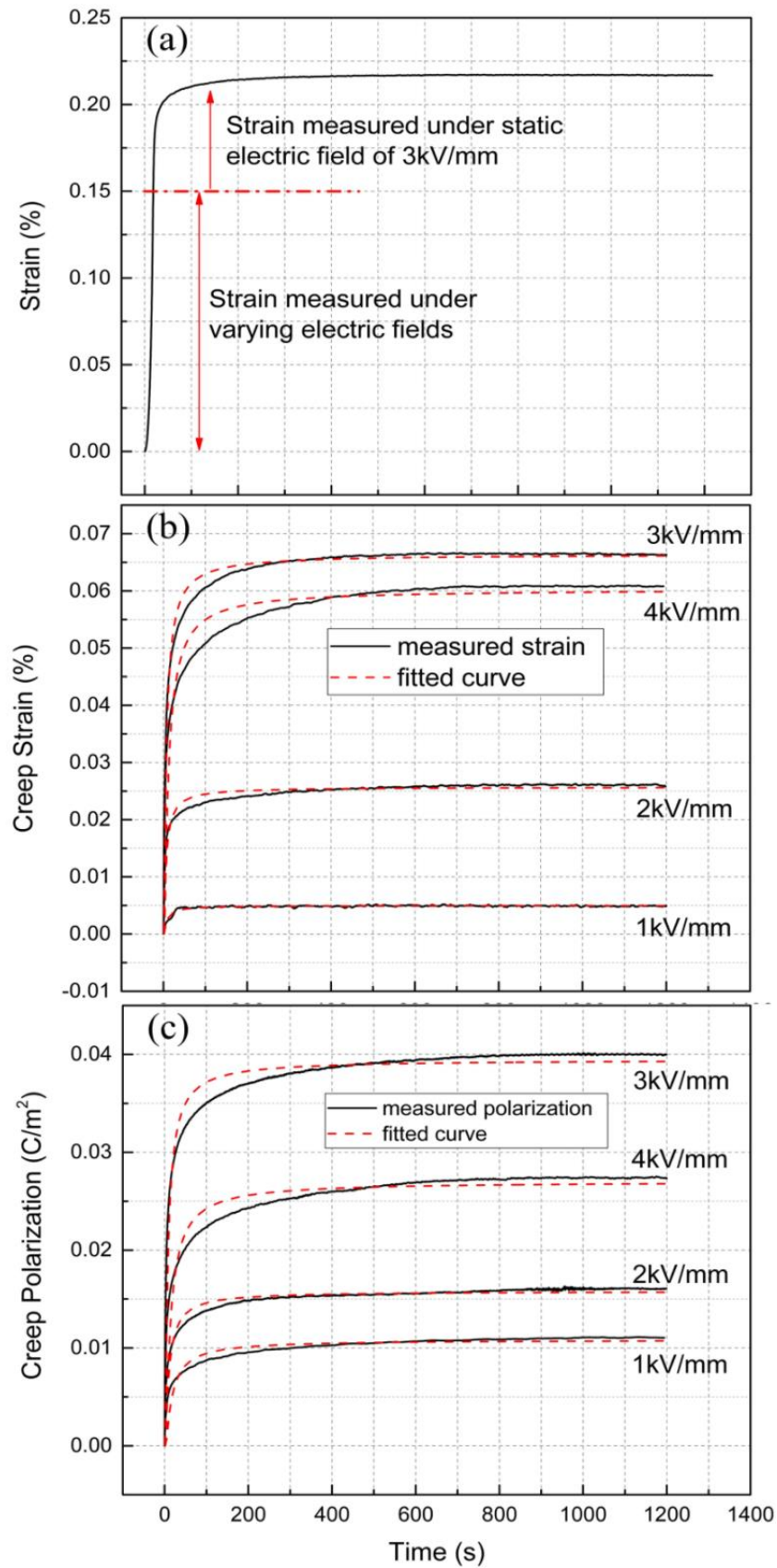


Figure 6.4: The creep behavior as a function of time: (a) two parts of the measured strain at 3kV/mm; (b) measured creep strains with their fitting curves; (c) creep polarizations with their fitting curves.

Table 6.1: Volume resistivity under various static electric fields.

Electric field (kV/mm)	Resistivity ρ ($\Omega \cdot \text{m}$)
1	$(3.6 \pm 1.4) \times 10^{11}$
2	$(1.3 \pm 0.2) \times 10^{11}$
3	$(9.9 \pm 1.0) \times 10^{10}$
4	$(6.7 \pm 2.6) \times 10^{10}$

Figure 6.3(c) depicts the polarization as a function of time under four static electric fields. It shows behavior comparable to the strain curves, i.e. growing rapidly first and then attaining saturation after a certain holding time. The measured results contain two parts: values obtained under varying electric field loading, followed by a creep response under static loading. Figure 6.4(a) provides an example to show those two regimes for the measured strain. In the first few seconds, the strain and polarization increase due to an electric field-induced transformation from a RE state to a long range ferroelectric order. As NBT-6BT-3KNN is an ergodic RE at room temperature that lacks macroscopic domains in the unloaded state, this domain switching below the RE-FE transformation field is unlikely to be a significant contribution.

When the electric field reaches the static state, creep strain (S_c) and creep polarization (P_c) are recorded at four constant electric fields, as shown in Figure 6.4(b) and (c), respectively. In these two figures, the zero point is the beginning of the hold time. It is apparent that the creep behavior depends on the magnitude of the applied static electric field. Interestingly, however, S_c and P_c reach the maximum values under 3 kV/mm, rather than 4 kV/mm. For the PZT materials, the theory of exhaustion of switchable domains is one of the potential mechanisms responsible for this observation [189]. The higher the applied electric field, the more easily ferroelectric domain switching is achieved. Therefore, the creep depends on the magnitude of the electric field. On the other hand, the total amount of domains available for switching is not infinite. When the externally applied constant electric field is higher than the coercive field, less creeping of strain and polarization can be observed because a large amount of the switchable domain has been exhausted around the coercive field [153]. The creep behavior presented in this experiment can analogously be attributed to the “exhaustion of state transition”. A much lower S_c and P_c can be obtained at 1 kV/mm because the low electric field cannot induce as much transition from RE to FE. Applying increasing static electric fields, the creep of both, S_c and P_c increase. This can be explained by the fact that the higher electric field further induces the RE-FE transition. However, the amount of RE phase available for transformation in one test has been consumed in large part once the electric field reaches 4 kV/mm, explaining why S_c and P_c do not show the largest values at 4 kV/mm.

Exponential function of Arrhenius type is used to fit the measured creep curves in order to describe the creep behavior:

$$S_c(t) = A_1 e^{-B_1/t} \quad (\text{Equation 6.2})$$

$$P_c(t) = A_2 e^{-B_2/t} \quad (\text{Equation 6.3})$$

Here t is the time, A_1 and A_2 are the magnitudes of creep response, and B_1 and B_2 are fitting coefficients to describe the degree of difficulty to reach saturation. The fitted curves are shown in Figure 6.4(b) and (c) as dashed lines and the values of the four fitting parameters A_1 , A_2 , B_1 and B_2 are listed in Table 6.2.

It should be noticed here, one fitting process to obtain the parameters of A_1 , A_2 , B_1 and B_2 is only suitable for the curve measured from the corresponding specimen. Owing to the errors in the measurement and fitting processes, these parameters listed in Table 6.2 are not applicable for quantitative analysis. The maximum values among the A_1 and A_2 can be observed at 3 kV/mm rather than 4 kV/mm, which matches the “exhaustion of state transition” hypothesis mentioned above. Compared with A_1 and A_2 , both B_1 and B_2 reach the maximum values when the maximum electric field is applied. The values of B_1 can still be separated into two categories. The values of B_1 under constant electric fields of 1, 2 and 3 kV/mm belong to a category, where the electric fields are not sufficient to transform the RE into FE entirely. Therefore, the values of B_1 under these three electric fields are close in value. The second category contains only the value of B_1 under an applied field of 4 kV/mm, owing to its markedly larger value as compared to electric fields of 1, 2, and 3 kV/mm. For NBT-BT-KNN materials, the minimum electric field needed to drive the material to reach its saturation state is termed the poling field (E_{pol}) [143], which is usually higher than 4 kV/mm. That is the reason why the electric fields in most published experiments on NBT-BT-KNN were applied at 6 kV/mm or higher [4, 54, 75]. The E_{pol} of NBT-6BT-3KNN has been reported between 4.5 and 5.5 kV/mm [4, 75], which depends on the processing conditions, composition, which dramatically affects the electromechanical properties, and the testing conditions, such as the electric field loading rate. In this context, note that the loading rate during the first period of electric field increasing corresponded to a frequency of 10 mHz, which is lower than the rate used in the formerly mentioned reports (50 mHz). A lower frequency induces larger strain in NBT-6BT-3KNN as demonstrated by Groh *et al.* [84]. The results of the aforementioned studies all point to the conclusion that a state of complete polarization has been reached at 4 kV/mm during the long hold time in our test, such that the RE phase is exhausted and completely transformed into the FE phase.

As a result, the creep behavior at the high electric field is different from the behavior at lower electric fields. The values of B_2 follow a similar tendency as B_1 , which implies that strain and polarization arise from the same creep mechanism. Before the exhaustion of the RE, the creep saturation is easier to reach. Once the RE to FE phase transition is complete or close to completion, the creep mechanism is no longer only dominated by this phase transition but also by a combined effect of FE domain creep due to switching and the transition mentioned above. Previous in-situ high-energy x-ray synchrotron studies have shown that during electrical loading there is the formation of ferroelectric domains perpendicular to the applied electric field loading direction [94]. These domains may become mobile for long enough hold time and contribute to the observed creep behavior. However, further work on modeling and experiments to explain this mechanism in details are still needed.

Table 6.2: The parameters obtained from the fitted creeping curves.

Electric field (kV/mm)	A_1	B_1	A_2	B_2
	1	0.5×10^{-2}	6.5	1.1×10^{-2}
2	2.6×10^{-2}	4.9	1.6×10^{-2}	7.9
3	6.6×10^{-2}	5.3	3.9×10^{-2}	6.1
4	6.0×10^{-2}	9.3	2.7×10^{-2}	10.9

In the second loading scenario, each sample was electrically loaded to 4 kV/mm. During loading, the electric field was held at 1, 2, or 3 kV/mm for 900 s before continuing to increase to 4 kV/mm. The results are plotted in Figure 6.5 and Figure 6.6. Based on the previous analysis, the leakage-induced charge has been subtracted from the data measured during holding. It can be seen that at the same

electric field level, higher values of polarization and strain can be obtained under loadings with hold times of electric fields compared to loadings without hold times. For example, when the electric field reaches 3 kV/mm (Figure 6.5(a), blue dash-dot line) and is held at that level, the measured polarization increases to $\sim 0.225 \text{ C/m}^2$ which is equivalent to the polarization at 3.5 kV/mm under the monotonic electric field loading conditions (Figure 6.5(a), green solid line).

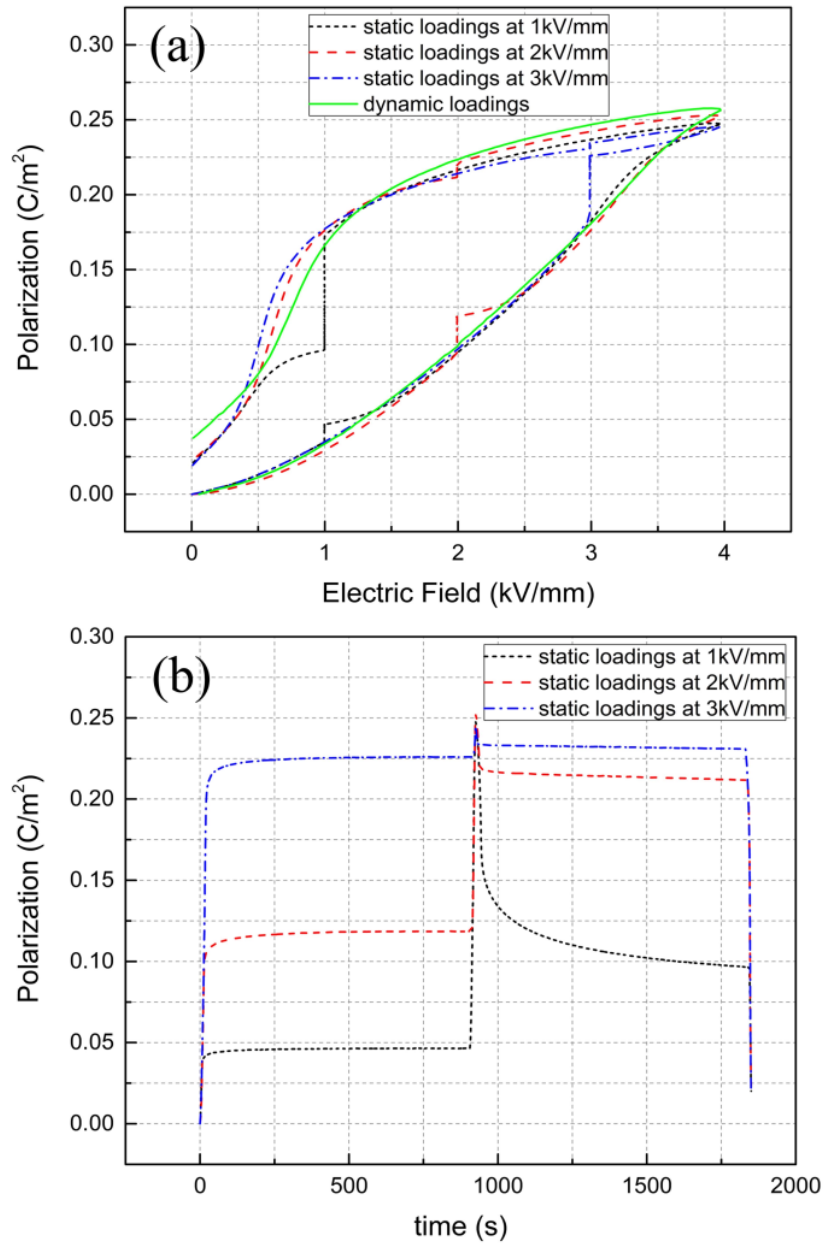


Figure 6.5: Polarization measured under constant electric fields controlled at both the loading and unloading periods: (a) polarization responses as a function of static and dynamic electric field loadings; (b) electric field and time dependent polarization responses.

When the constant electric field was held at 4 kV/mm, the polarization could reach or even exceed the value of polarization measured at E_{pol} , so that the electric field-induced phase transition is able to complete under the static electric field loading condition at 4 kV/mm. In Figure 6.5, it can clearly be observed that the creep behavior under constant electric fields held during the loading period matches the results in Figure 6.3(c) very well. During the first hold time of 900 s, there is an apparent saturation

behavior in both the strain and the polarization for each applied bias electric field level, demonstrated in Figure 6.5(b) and 6.6(b). During unloading, there is a subsequent relaxation that results in a time-dependent strain and polarization decrease. Conversely to loading, 1 kV/mm shows the largest electromechanical relaxation, whereas the relaxational strain and polarization for 2 and 3 kV/mm is significantly smaller. This is due to the proximity to the critical reverse transformation field from the long-range ferroelectric order to a RE state, defined as the inflection point in the unloading curve of the polarization-electric field response [143]. As a result, the FE state is still preserved when the unloading electric field is kept higher than this critical electric field. When the electric field decreases near to or below the transition field, a reverse FE-RE transformation occurs. Similarly, the largest creep is obtained in PZT around the coercive field due to the large amount of domain switching which is induced there [153, 183].

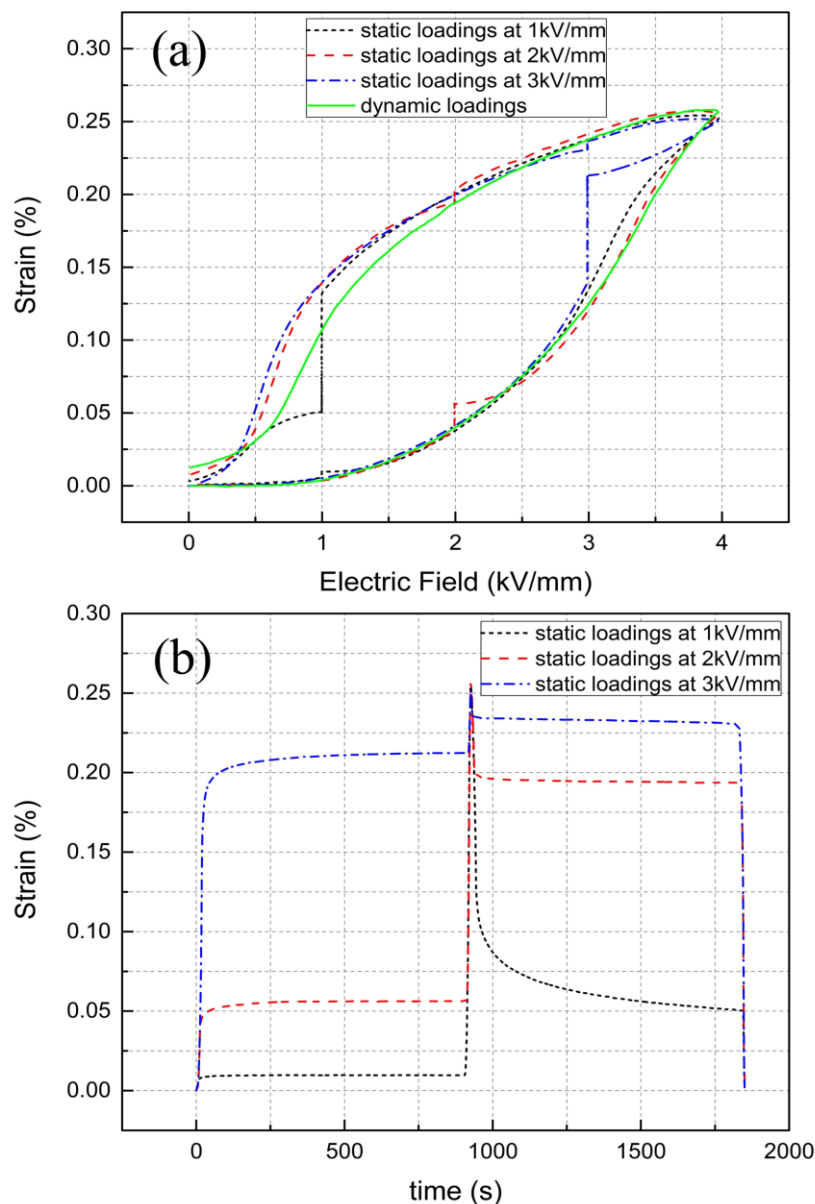


Figure 6.6: Strain measured under constant electric fields controlled at both the loading and unloading periods: (a) static and dynamic electric field and time dependent strain responses; (b) strain responses under constant electric fields plotted as a function of time.

6.3 Summary

In this chapter, electric field-induced strains and polarization were investigated. Especially, the creep polarization and creep strain in NBT-6BT-3KNN lead-free piezoceramics induced by constant electric fields was studied. The charge leakage induced error in the measurement of polarization was determined, providing approximate values of volume resistivity. It was found that the volume resistivity shows nonlinearity under large electric field loading. Both polarization and strain exhibited a time-dependent response under the application of a constant electric field. The mechanism of creep behavior of polarization and strain is primarily due to the gradual transition between RE and FE states, which is a reversible process. Therefore, when the constant electric field was held during both loading and unloading processes, the field-induced creep behavior can be explained by the exhaustion of this state transformation. A constant electric field induces large creep only before the exhaustion of the RE. Once there is no sufficient RE left to be transformed during the hold time, the higher electric field neither induces larger creep nor drives the creep into saturation easily. This finding was revealed by using an Arrhenius-type exponential fit function. However, further evidence is needed to explore this phenomenon in depth. During the electric unloading process, creeping can be obtained prominently near the critical field owing to the electric field here being no longer able to prevent the FE from transforming to the RE.

7 Experiments on NBT-7BT/NBT-6BT-3KNN composites under electric field loadings

7.1 Introduction

The introductions of the NBT-BT and NBT-BT-KNN ceramic families have been given in section 1.3.2 and section 1.3.3, respectively. The NBT-BT system has been of great interest since the discovery of a MPB where rhombohedral NBT and tetragonal BT coexist [48]. By optimizing the content of BT around 6~7 mol.%, a significant enhancement in dielectric permittivity and electromechanical coupling factor k_{33} can be obtained [72]. Recently, KNN was used to modify the NBT-BT system which results in the NBT-BT-KNN piezoceramic system. This new solid solution family presents a giant electric field-induced strain to make it one of the most promising lead-free piezoelectric alternatives for the application of actuators, and consequently it has attracted great attention [4, 85].

However, the requirement of high poling fields and large strain hysteresis are the drawbacks limiting the application of these materials [131]. The design of a relaxor/ferroelectric (RE/FE) composite provides a highly effective way to resolve both the challenges [5] which has been reviewed in section 1.3.5.2. Following this idea, recent work on the lead-free RE/FE composites have proven that the composite with this structure provides a reduction of the driving electric field and also yields an enhanced strain by tailoring the contents of the RE phase (works as matrix) and the FE phase (works as seed) [5]. Besides, the mechanism of polarization and strain coupling were also discussed [143]. To date, most of the strain measurements on such composites were performed by using linear variable displacement transducers (LVDT), which does not provide details of the strain distribution in the composite during the electric field loading. That hinders further investigation to understand the electromechanical coupling. The DIC method was widely adopted in the field experimental mechanics owing to its unique advantages [163], which has been introduced in the previous chapters. By selecting a region of interest (ROI) on a test object surface, the information on strains can be obtained where the ROI is located. This feature makes the DIC method be a highly effective tool suitable for monitoring the deformation of each layer of the RE/FE multilayer composite mentioned above, separately.

In this chapter, the lead-free materials NBT-6BT-3KNN and NBT-7BT were used as RE matrix and FE seed, respectively. RE/FE bilayer and RE/FE/RE trilayer composites were prepared to investigate the polarization and strain coupling effects. The DIC method was employed to record the complete deformation behavior of each layer and the whole composite during the electric field loadings. By selecting the ROIs located on each layer and calculating the strains there, an obvious remnant strain from the RE matrix layer and a decreased value from the FE seed layer can be found after cyclic electric field loading. This finding implies the existence of internal stresses in each layer. For further investigation, full-field contour plots of strain were drawn. An intermediate strain state can be watched around the interface between the two layers. So graded stress states around both sides of the interface are expected. This method of test presents high potential for measuring complex multilayer structures which provides helpful experimental data for constitutive modeling.

7.2 Experimental procedures

The introduction on preparation of BNT-BT-3KNN and BNT-7BT powders, bilayer ceramics and trilayer ceramics can be found in section 3.1. It should be noticed that, the bilayer and trilayer composites were designed as model system to understand the electric field-induced strains of each layer as a part of the composite rather than obtaining the largest enhanced strain response. Therefore, the ratios of RE layer and FE layer were not optimized but keep the ratios easy to be observed by a digital camera. The maximum electric field of 4 kV/mm was selected to avoid the possible electric arcing rather than 6 kV/mm which would provide a higher value of d_{33}^* .

The setup employed to conduct this work was presented in section 3.2. Compared with the system designed for investigating the PZT samples, two modifications were adopted for measuring the ceramic/ceramic composite specimens. First, a lens with $2\times$ magnification was used to provide a higher resolution ($1.75\ \mu\text{m}/\text{pixel}$) than the former $1\times$ lens ($3.5\ \mu\text{m}/\text{pixel}$). Second, artificial speckles were sprayed onto the observation surfaces by means of taking an air brush (AT-Airbrush Pistole Kit, AT-AK-02, Agora-Tec, Germany) instead of the natural texture on the surfaces. The size of the droplet of the paint (Model Air, Black, Acrylicos Vallejo, Spain) can be controlled by the air brush to create patterns suitable for the DIC tracking. In this work, 3 cycles of bipolar ramp loading with the same loading rate of $0.016\ \text{kV}/\text{mm}\ \text{s}^{-1}$ (0.01Hz) were applied to the samples from their unpoled state. At the same time, the camera captured 2 images per second to record the deformation of the object when the loading was applied.

7.3 Electromechanical behavior on the two end member materials

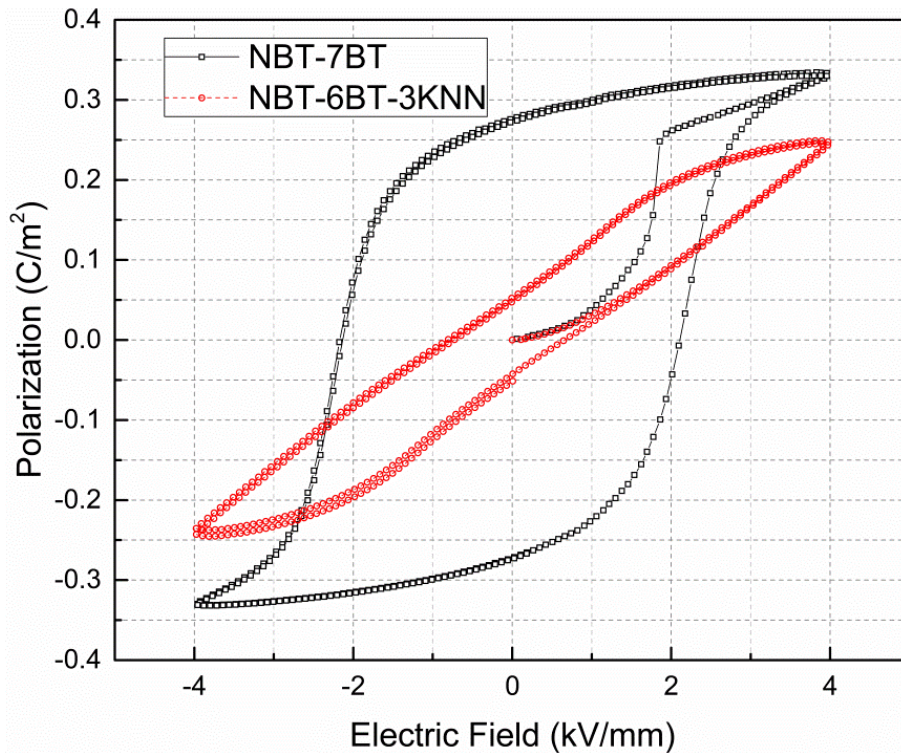


Figure 7.1: Polarization curves measured from NBT-7BT and NBT-6BT-3KNN ceramics independently.

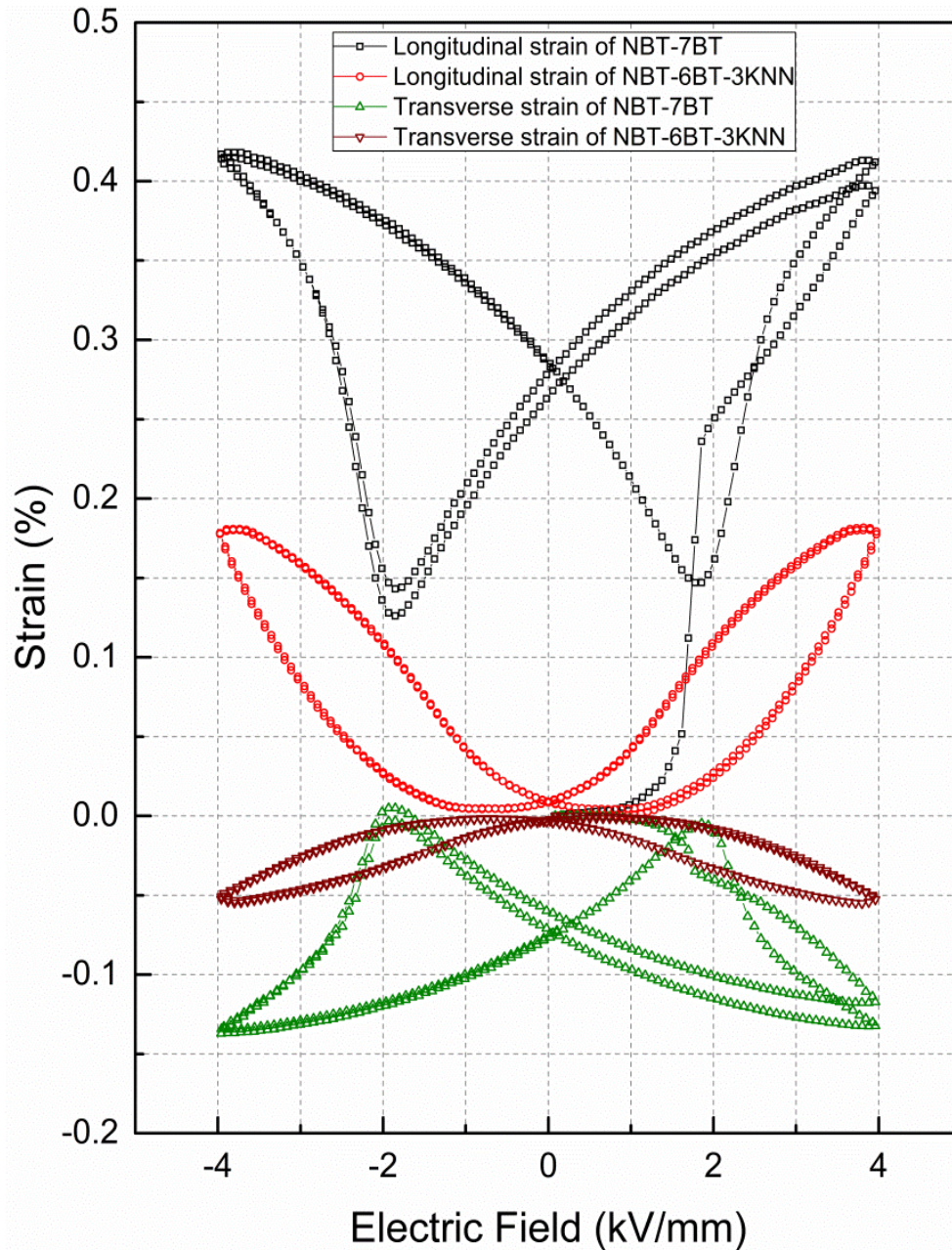


Figure 7.2: Longitudinal and transverse strains measured from NBT-7BT and NBT-6BT-3KNN ceramics under cyclic electric field loadings.

Figure 7.1 and Figure 7.2 show the polarization and strain curves measured on NBT-7BT and NBT-6BT-3KNN ceramics. These results have been discussed in section 5.1 and 6.1, respectively. These curves are plotted here again to provide a better illustration for comparison. In addition, the transverse strain was added into Figure 7.2 where the deformation monitored along both the longitudinal and transverse directions are shown simultaneously.

Figure 7.3 demonstrates the volume changes on the two types of ceramic specimens. The volume changes S_{volume} were calculated by

$$S_{\text{volume}} = S_3 + 2S_1. \quad (\text{Equation 7.1})$$

Here, S_3 and S_1 denote longitudinal and transverse strain respectively. The S_{volume} of NBT-6BT-3KNN shows approximately 0.07% of change at 4 kV/mm and leaves almost zero volume change when the

electric field is removed. In contrast, the NBT-7BT shows a large remnant volume change after the first half cycle of electric load. Under the following bipolar loadings, the volume change does not show much variation. It indicates that once the non-ergodic RE is transformed into FE state by an electric field, the following electric loading only induces domain switching with little volume changes. However, the reversible transition from the ergodic RE to FE state leads to large volume changes. These phenomena on the two materials are attributed to the reversible and irreversible state transitions which were discussed in section 1.3.4. These results shown in Figure 7.3 validate the ergodic and nonergodic properties mentioned previously once again.

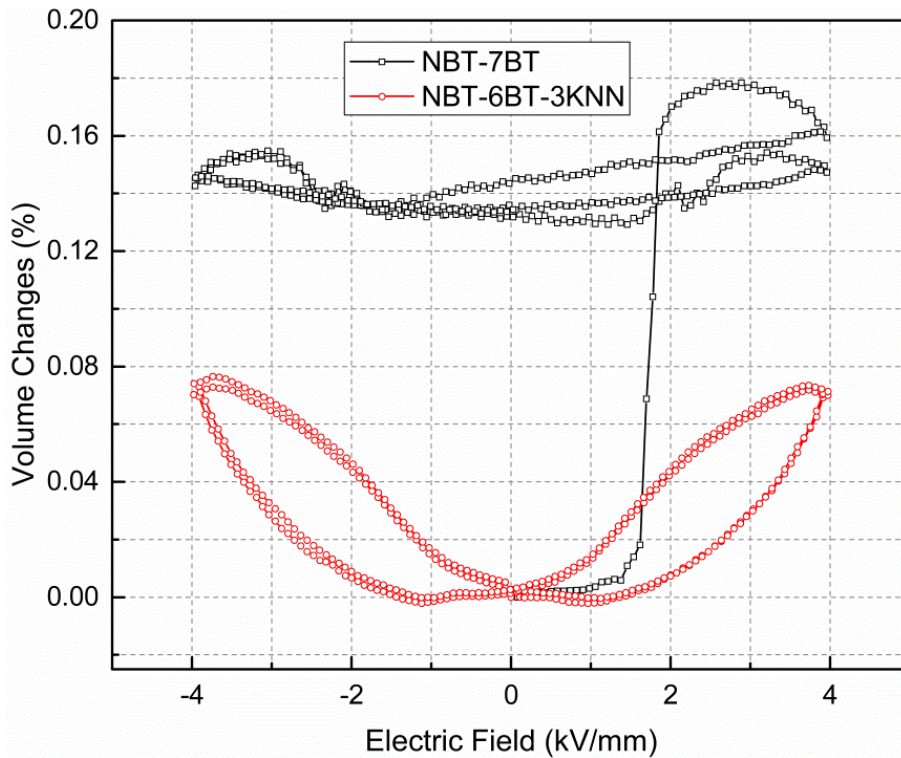


Figure 7.3: Volume changes of the two specimens.

7.4 Experiments on bilayer composite

7.4.1 Initial state selected for DIC tracing

The DIC method compares the images of deformed states of the object with a reference image. As seen in Figure 7.4, the image without any loading as reference was captured from a bilayer specimen. The NBT-7BT layer and NBT-BT-3KNN layer show a slight difference in darkness so that the interfaces can be distinguished and marked in Figure 7.4(a) approximately. The artificial patterns covering the surface of the specimen provides enough random markers with sufficient contrast for the DIC tracing. The red crosses in Figure 7.4(c) represent the targets for tracing, i.e. the centers of the subsets to be traced. Consequently the area of the images covered by the red crosses will be the corresponding ROI for evaluating the strains [174]. As a result from the interdiffusion at the interface of the two end members during the preparation, the state of stresses around these regions could vary from those of each end member. Therefore, the ROIs were placed carefully to avoid the region close to the interface. A big advantage of the DIC method is that the ROI can be placed anywhere on the captured images to calculate the strain of this part of the surface. The strains obtained from these various ROIs simultaneously and independently.

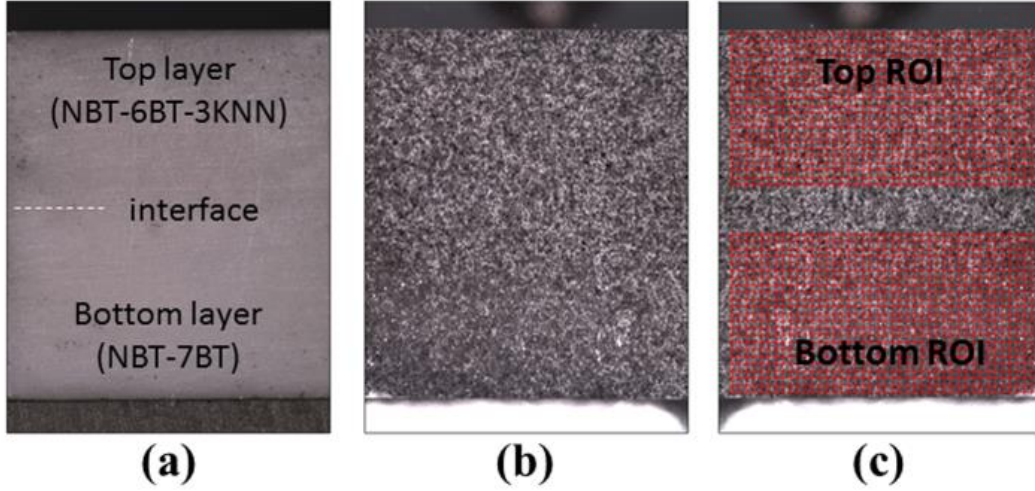


Figure 7.4: Reference images of bilayer composites: (a) digital image of specimen without artificial patterns; (b) specimen with sprayed black and white patterns; (c) selected ROIs on the surfaces of specimen.

The initial state of bilayer sample selected as a reference here is the as-prepared specimen without any external electric field load. However, these specimens were not at a “zero stress” state in fact. It is ascribed to the in-plane biaxial stresses developed by the mismatch in sintering the two layers during the preparing processing [190]. A. Ayrıkyan *et al.* [138] sintered NBT-7BT/NBT-25ST bilayer composite and found that the NBT-7BT is in a biaxial compression while NBT-25ST is in a state of biaxial tension. In the investigation of NBT-7BT/NBT-6BT-3KNN composite, more studies are still required to provide the additional information on the analysis of the internal stresses. In the following discussions on the strains measured from ceramic/ceramic composites, these internal stresses induced by sintering have to be excluded because of lacking more experimental evidences.

7.4.2 Polarization and strains in bilayer

7.4.2.1 Polarization in bilayer

The P - E hysteresis is depicted by Figure 7.5. The maximum polarization reaches around 0.34 C/m^2 when the electric field was applied at 4 kV/mm , which is larger than the pure end member of NBT-6BT-3KNN (around 0.25 C/m^2) but close to the value of NBT-7BT (around 0.33 C/m^2) at the same amplitude of electric field (given by Figure 7.1). The enhanced polarization of the NBT-6BT-3KNN layer can be explained by the polarization coupling effect, and similar results were reported by Groh *et al.* [84]. In Figure 7.1, the coercive fields (E_c) of NBT-7BT and NBT-6BT-3KNN are $\sim 2.2 \text{ kV/mm}$ and $\sim 0.7 \text{ kV/mm}$, respectively, while this switching field shown in Figure 7.5 locates approximately at $\sim 1.5 \text{ kV/mm}$. This coercive field of the bilayer is close to an average value of 2.2 kV/mm and 0.7 kV/mm mentioned above, which corresponds to the volume fraction of RE:FE is 50% to 50%. An equation is proposed to estimate E_c of bilayer composite as a function of volume fraction of RE and FE layer approximately as

$$E_c^{bi} = E_c^{FE} a + E_c^{RE} (1-a). \quad (\text{Equation 7.2})$$

Here, E_c^{bi} is the coercive field of the bilayer composite, and E_c^{FE} and E_c^{RE} represent the coercive field values of the pure FE and RE end members, respectively, while a is the volume fraction of the FE layer in the composite. Lacking of more specimens with varying volume fraction of RE:FE in this experiment, the data reported by Groh *et al.* [84, 142] were taken to validate this equation. In these references, similar RE and FE materials as well as the bilayer systems were prepared. Therefore, the Equa-

tion 7.2 is suitable for estimating the coercive field of a bilayer composite of NBT-7BT and NBT-6BT-3KNN at room temperature.

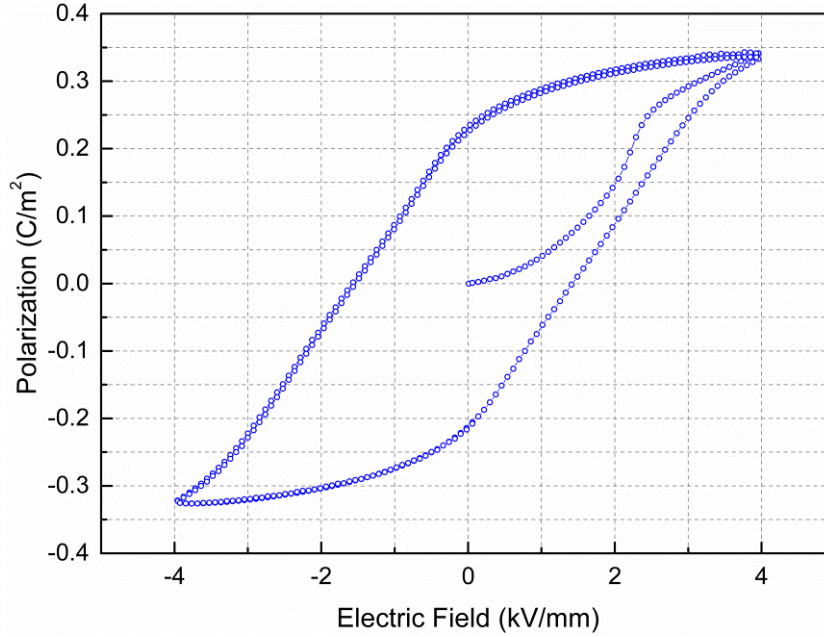


Figure 7.5: Polarization measured from the bilayer composite.

7.4.2.2 Stress mismatch of the composite

By reading the data from Figure 7.2, the remnant strains in transverse direction of the single components NBT-7BT (FE) and NBT-BT-3KNN (RE) after an electric field loading are around -0.075% and 0%, respectively. These two end members are assumed in the virgin state even after sintering together into a piece of composite. To keep a balance of forces after applying and removing the electric field of 4 kV/mm, the internal stresses between the two components in the bilayer composite can be calculated by two equations given by H. Zhang *et al.* [143]

$$\sigma_{RE} = \varepsilon_r^{FE} \left[\frac{1}{Y_{RE}} + \frac{1}{Y_{FE}} \left(\frac{n^{RE} h^{RE}}{n^{FE} h^{FE}} \right) (1 + \varepsilon_r^{FE}) \right]^{-1} \quad (\text{Equation 7.3})$$

$$\sigma_{FE} = -\sigma_{RE} \left(\frac{n^{RE} h^{RE}}{n^{FE} h^{FE}} \right). \quad (\text{Equation 7.4})$$

Here, σ is the internal stress, Y is isotropic elastic modulus, n is the number of layers, h is the thickness of one single layer, and ε_r is the transverse remnant strain of one ceramic end member. The elastic moduli are 103 GPa and 111 GPa for NBT-6BT and NBT-6BT-2KNN, respectively [191], which are taken to compute the internal stresses owing to lacking of the data for NBT-7BT and NBT-6BT-3KNN. For the bilayer composite, the biaxial compressive stress on the NBT-6BT-3KNN layer is -33 MPa while the biaxial tensile stress on the NBT-7BT layer is 33 MPa to ensure force equilibrium.

The average strains plotted in Figure 7.6(a) and (b) was calculated by tracking the displacement over a large ROI (Figure 7.4) and averaging the displacement of every marker in that region for calculation of overall strain. From Figure 7.6(a), the biaxial remnant strain value of the RE component of the bilayer is shown to be approximately 0.105%, as compared to 0% in the pure RE sample in Figure 7.2. On the other hand, the remnant longitudinal strain of the FE portion drops from 0.275% in the pure end mem-

ber to 0.16% in the bilayer. The remnant transverse strain of the RE layer is $-1.8 \times 10^{-2}\%$, while the value for FE portion is close to 0 ($-4.8 \times 10^{-3}\%$) as shown by Figure 7.6(b). From those two values, it can be observed that RE layer shrinks more than the FE layer along the transverse directions. As a result, the RE layer experiences tensile stress while the FE layer is under compressive stress to ensure the force equilibrium. These directions of stresses are the reverse of those predicted by the calculations using Equations 7.3 and 7.4 based on the piezoelectric response of the pure end members, which cannot be provided by checking from using an LVDT.

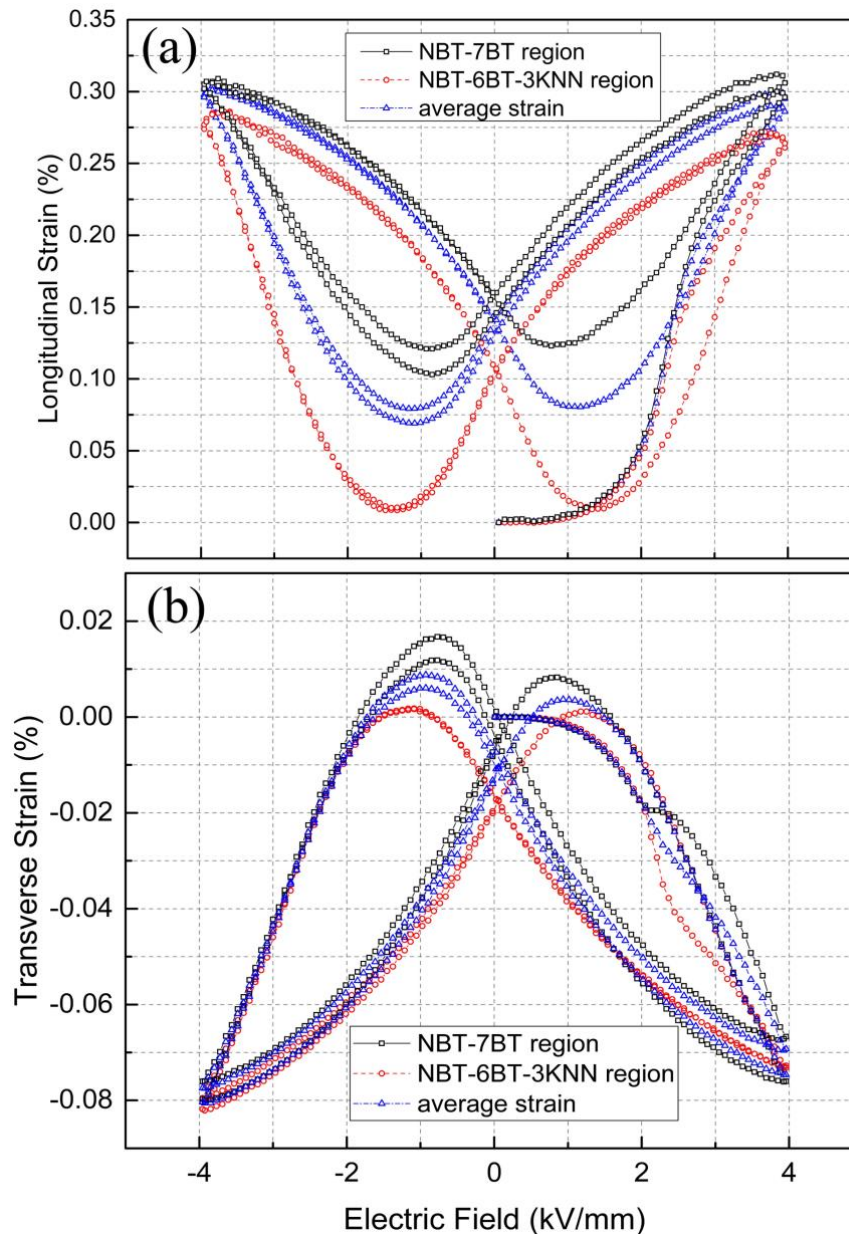


Figure 7.6: Strains measured from the same composite: (a) longitudinal strains obtained from the corresponded ROIs on the surface of the specimen; (b) transverse strains obtained from the corresponded ROIs.

The difference in the d_{31}^* values between two pure end members was used to explain the stress mismatch in 91BNT-6BT-3AN/BNT-7BT multilayer systems [143]. In the experiment here, d_{31}^* values are obtained by the secant modulus between the remnant and maximum transverse strain measured at 4 kV/mm provided in Figure 7.2. The d_{31}^* values are -135 pm/V and -150 pm/V for RE and FE pure end

members, respectively. This small difference of 15 pm/V in the two d_{31}^* values after the initial loading (first half cycle of electric field loading) would not induce an obvious stress mismatch under the electric field range of 4 kV/mm. However, the nonlinear relationship between the transverse strain and applied electrical field was not investigated, and this estimation is also based on the piezoelectric response of the pure end members. Therefore, further work on modeling and experiments to explain this phenomenon and analyze the stress states are still needed.

In this section, three factors influencing the internal stress state have been introduced. There are: 1) Mismatch in sintering between the two layers. This factor induces internal stresses during the sample preparation. However, it is still hard to estimate these stresses quantitatively. The only thing clear is that pure NBT-7BT shrinks faster than pure NBT-6BT-3KNN during sintering. 2) Difference in the remnant transverse strains in the two ceramics. This difference is induced by a first half cycle loading and it is an irreversible behavior unless an efficient high temperature is reached. The difficulty is that the coupling effects (both polarization and strain coupling) should be considered to understand the remnant transverse strains in the bilayer, which is much harder than the analysis on the pure end members. 3) Variation in the d_{31}^* values between the two materials. As discussed previously, the two d_{31}^* values of the pure end members do not show a large difference. However these two values are obtained after the first half cycle of loading and the nonlinear behavior is not considered. Therefore, the curves shown in Figure 7.6 are the combined results in a bilayer specimen. It is still hard to make a solid conclusion owing to lacking of more data. But, the results provided by this experiment are helpful to other investigations which could explain this complicated electromechanical coupling effect under an electric field loading.

7.4.2.3 Volume changes in bilayer

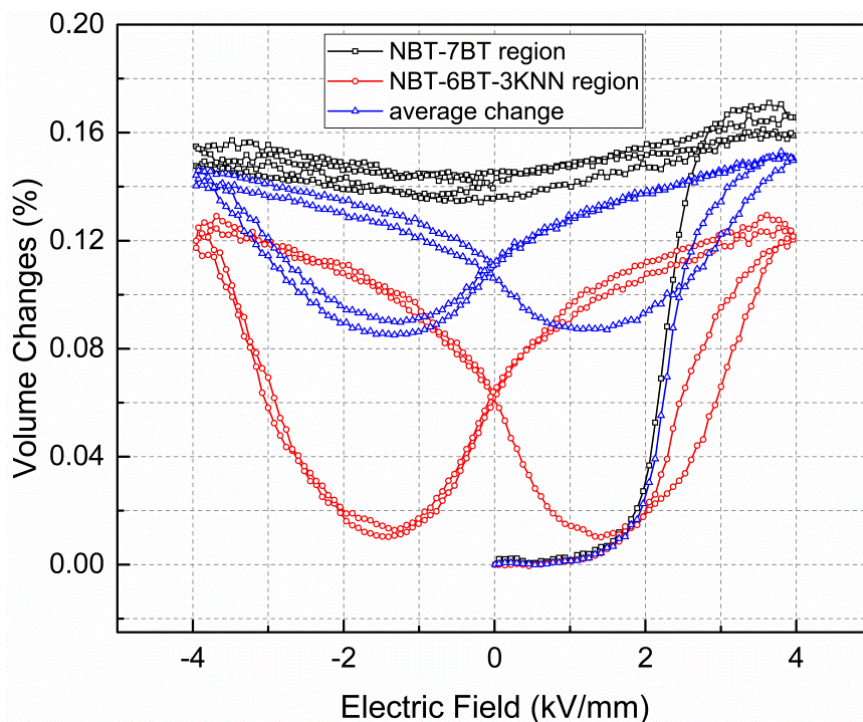


Figure 7.7: Volume changes measured from the bilayer composite.

Previous work has investigated the volume change of BNT-based ferroelectrics with applied electric field [97, 192], but to date this phenomenon has not been evaluated in BNT-based composites. In Figure 7.7, the volume changes of bilayer sample are plotted. These values were calculated by using

the longitudinal and transverse strain data depicted in Figure 7.6. The FE layer shows a large change in volume to $\sim 0.15\%$ during the first half electric field loading, at which it plateaus and does not change during electric field cycling. The large remnant volume change corresponds the transition of the FE layer from the unpoled state to the poled state, which is associated with a crystallographic phase transition from a mixed rhombohedral and tetragonal phase in the unpoled state to a predominantly tetragonal structure in the poled state [94]. Corresponding to the remnant strains plotted in Figure 7.6, the RE layer shows 0.062% remnant volume change, approximately. This result is different from the volume change measured from pure NBT-BT-3KNN, where the volume change after removal of applied field was 0. However, due to the complexity of the stress states on each layer and the possible inner electric field, more investigations on this composite are needed to explain these findings.

7.4.2.4 Contour plots of strains on the bilayer composite

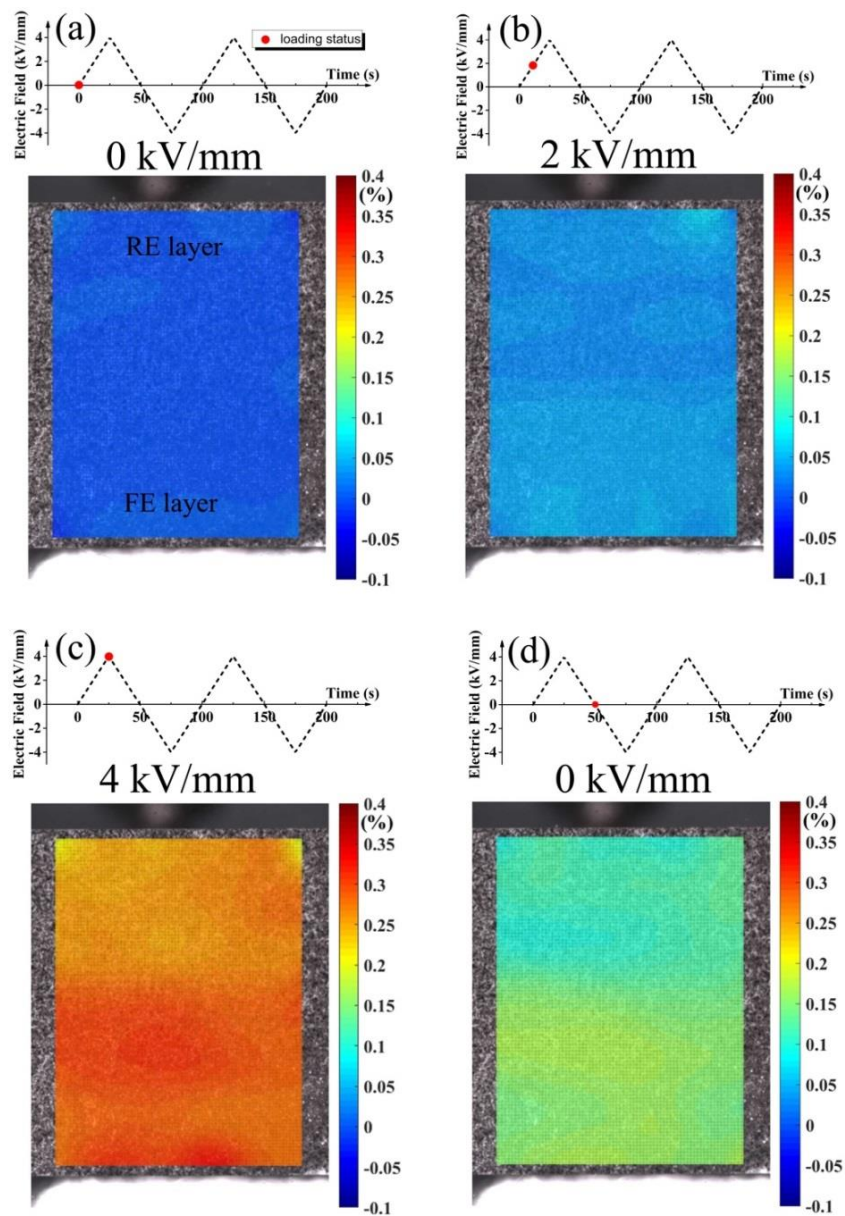


Figure 7.8: Contour plots of longitudinal strains measured under the first half cycle of a bipolar loading.

In Figure 7.8 and 7.9, the contour plots of the longitudinal strains are shown. This strain distributions provide more “local” information, the spatial resolution of which depends on the resolution of the camera used during measurement. These contour plots provide direct evidence of the inhomogeneous deformation in the bilayer composite. Figure 7.8 is used to describe the first cycle of electric loading and unloading. The subsequent strain states under bipolar loadings are demonstrated in Figure 7.9. Owing to the symmetry of S - E “butterfly” curve after the first half of the loading cycle (as shown in Figure 7.6), only two states of strain are plotted in Figure 7.9 (c) and (d) for the subsequent bipolar loading.

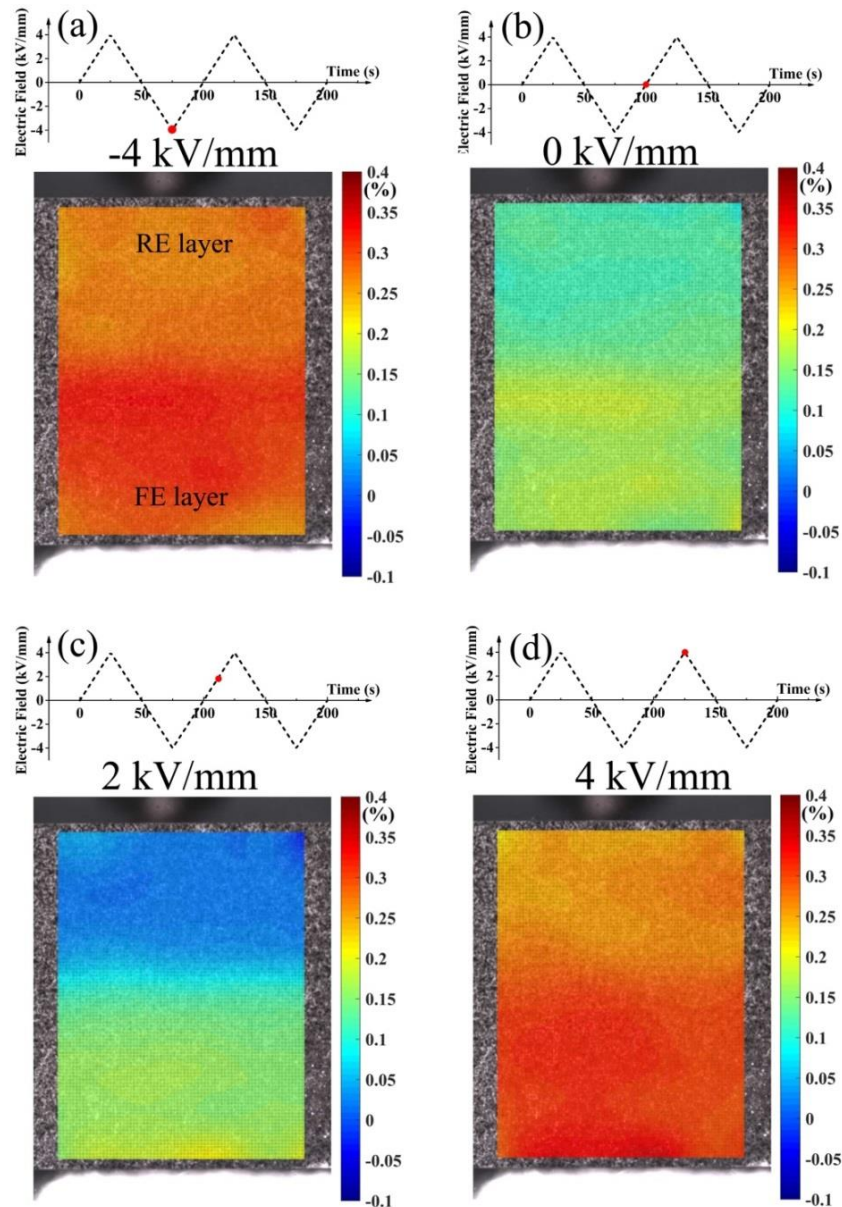


Figure 7.9: Contour plots of longitudinal strains measured at various states of electric field.

The initial state is shown in Figure 7.8(a). Due to the small gap between the starting times of the voltage source and digital camera (0.02 s), there are slight errors in that contour plot. As the electric field is applied, the two layers show strain responses which can be distinguished gradually (Figure 7.8(b) and (c)). At an electric field of 4 kV/mm, both the layers reach the maximum states of strain (Figure 7.8(c)). Figure 7.9(a) and (d) demonstrate the strain states at -4 and 4 kV/mm, respectively.

These two states are similar to Figure 7.8(c) shows, corresponds to the numerical values for average longitudinal strain as shown in Figure 7.6 (a) well. Figure 7.8(d) and 7.9(b) show almost the same strain distribution at 0 kV/mm. However, obvious remnant strains can be observed in both the two layers compared with the initial state in Figure 7.8(a). In Figure 7.9(c), an intermediate strain state can be found at the interface between the two layers. It is expected that the strain will show a gradation in value on both sides of the interface, due to the differences in stress state between the FE and RE layers. The natural properties of ergodic RE and non-ergodic RE can be used to explain the difference between Figure 7.8(b) and 7.9(c). For the NBT-BT-3KNN (ergodic RE), the electric field-induced phase transition from RE to FE is a reversible process. On the contrary, once the transition from RE to FE is completed for NBT-7BT (non-ergodic RE), the FE phase will not disappear during the electric field unloading process. Therefore, the large remnant strains are retained unless the sample is heated past its depolarization temperature. Figure 7.8(d) shows the remnant strain after the first half cycle of loading, in which a large remnant strain of approximately 0.2% appears in the FE layer, as compared to the RE layer, in which the remnant strain is below 0.1%. The remnant strain in the RE layer then enables a higher strain response upon application of electric field as compared to the FE layer. Therefore, during the second loading cycle, at 2 kV/mm (as shown in Figure 7.9(c)) a large difference between the FE and RE layers can be observed in the strain response, relative to 2 kV/mm in the first cycle, shown in Figure 7.8(b), where the two layers are nearly uniform in strain response. Figure 7.9(c) also shows an interface region between the RE and FE layers, in which a strain of approximately 0.1% can be observed, spanning the length of the interface. This strain value lies between the strains measured in the FE and RE layer, providing evidence of intermediate stress states that enable strain coupling between the two components of the composite structure.

7.5 Experiments on trilayer composite

In last section, the deformation of bilayer composites induced by external electric fields was discussed. However, the variations in sintering rates induce the biaxial stresses resulting in a certain degree of bending. Therefore, a local density gradient was observed in a bilayer system [138]. This effect in the middle layer of a trilayer composite could be compensated by the top and bottom layers in this “sandwich” structure. Following the experiments in bilayers, the same experimental procedures are applied to the RE/FE/RE trilayer composites.

7.5.1 Initial state of trilayer selected for DIC tracing

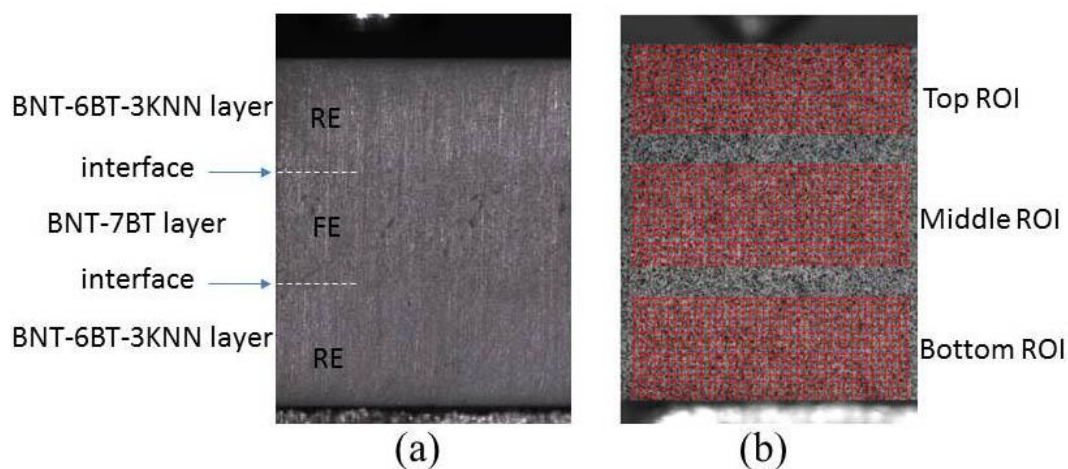


Figure 7.10: Reference images of trilayer structures: (a) digital image of trilayer without artificial patterns, (b) selected ROIs on the surfaces of trilayer with sprayed black and white patterns.

Figure 7.10 shows the initial state of the trilayer specimen selected for DIC tracing. Similar to the state selected for the bilayer in Figure 7.4, this initial state cannot provide the information of strains caused by the internal stresses during sintering. Three ROIs were placed carefully to avoid the regions close to the interfaces after painting the artificial patterns (as demonstrated in Figure 7.10(b)).

7.5.2 Polarization and strains in trilayer

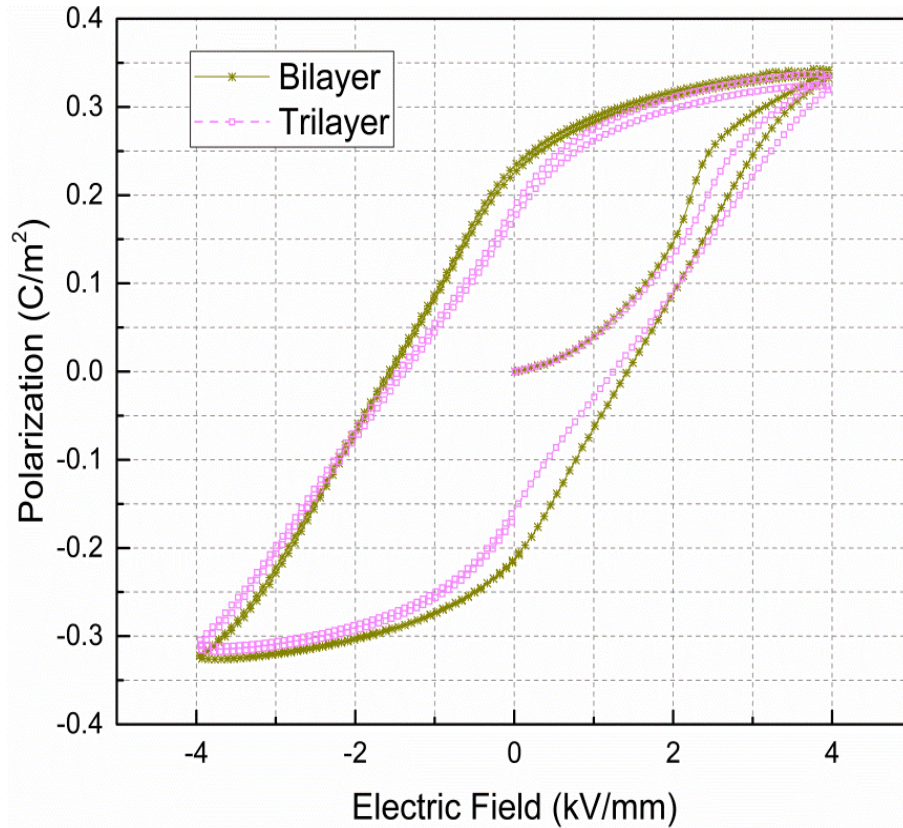


Figure 7.11: Polarization measured from the bilayer and trilayer composites.

In order to make a comparison between the polarization measured on bilayers and trilayers, the results measured on each composite are plotted in Figure 7.11. The bilayer presents a slightly larger remnant polarization and coercive field than the values of the trilayer. That is explained by the content of FE in the bilayer being larger than that in the trilayer, which has been discussed in other report [84]. In addition, the states of the internal in-plane stresses should be considered. The coercive field of the trilayer sample is around 1.2 kV/mm (as shown in Figure 7.11), which matches the value estimated by using Equation 7.2. This result validates that the coercive field of a composite follows the proportionality of the volume fraction of each layer that has been discussed in section 7.3 before.

Owing to the variation in the volume fractions of each layer between the two composites, differences in bipolar strains measured from the bilayer and trilayer can be observed. The strains measured from the trilayer composite are shown in Figure 7.12. Compared with the strain curves of the bilayer plotted in Figure 7.6, the remnant strain of each layer is smaller than the ones in the bilayer. The deformation behavior of the trilayer is similar to the bilayer; therefore, the mismatch of the stresses discussed on the bilayer can also be adopted here. Such as Equations 7.3 and 7.4 can be applied on the trilayer to obtain that the biaxial compressive stress on each RE layer is -22 MPa while the biaxial tensile stress on FE layer is 44 MPa. However, this calculation is also based on the piezoelectric response of the pure end members. Owing to the complexity of the coupling effects mentioned in section 7.4.2, a solid conclu-

sion is still hard to make only from the results shown in Figure 7.11 and 7.12. Table 7.1 lists a comprehensive comparison of longitudinal strains and polarizations for single component ceramics, the bilayer composite and the trilayer composite. These data would provide contribution for the community.

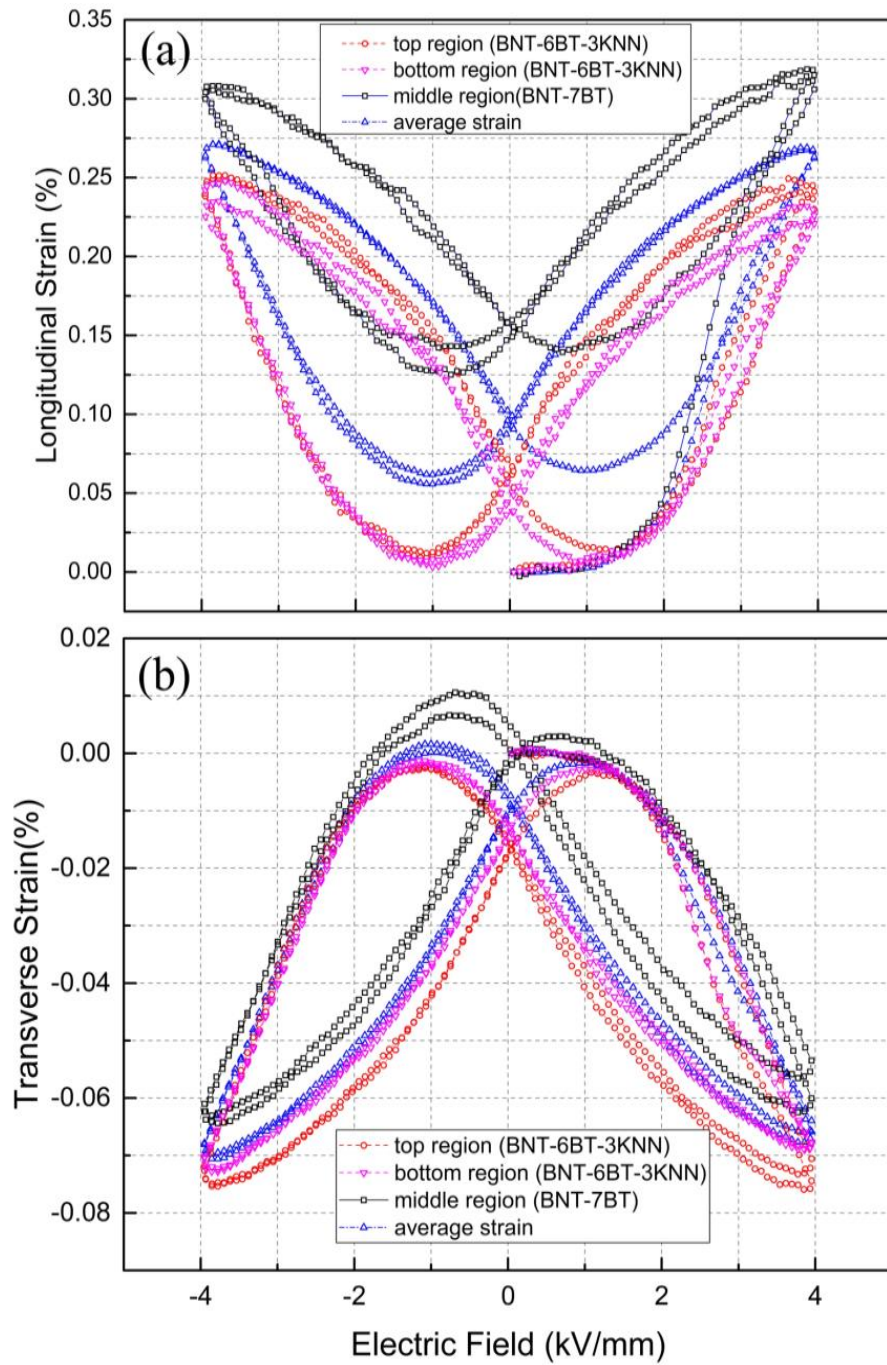


Figure 7.12: Strains measured from the trilayer composite: (a) longitudinal strains obtained from the corresponded ROIs on the surface of the specimen; (b) transverse strains obtained from the corresponded ROIs on the surface of the specimen.

Table 7.1: Comparison of bipolar longitudinal strain and polarization loops

	Pure ceramic end member		Bilayer composite			Trilayer composite			
	Pure 7BT	Pure 3KNN	Bilayer total	FE layer	RE layer	Trilayer total	FE layer	RE layer (top)	RE layer (bottom)
Maximum total strain (%)	0.41	0.18	0.31	0.30	0.27	0.27	0.31	0.25	0.24
Remnant strain (%)	0.27	0.01	0.13	0.15	0.11	0.09	0.16	0.06	0.04
Backswitching strain (%)	0.14	0	0.07	0.04	0.1	0.03	0.03	0.06	0.04
Maximum polarization (C/m ²)	0.33	0.25	0.34	-	-	0.33	-	-	-
Coercive field (kV/mm)	2.2	0.7	1.5	-	-	1.2	-	-	-
Remnant polarization (C/m ²)	0.26	0.05	0.23	-	-	0.16	-	-	-

7.6 Summary

In this chapter, the DIC method was implemented to check the strain distribution in the ceramic/ceramic bilayer and trilayer composites.

For the bilayers, it was shown that the coercive field of the bilayer corresponds to the rule of mixtures predictions. It was further demonstrated that the local strain of individual components or ROIs of a composite could be measured with the DIC system. A high remnant strain was observed in the RE layer and a decreased value from the FE layer upon cyclic electric field loading. This finding reveals the directions of the internal stresses on each layer (biaxial tensile stress on RE layer and compressive stress on FE layer). The full-field contour plots of strain are used to demonstrate the strain distributions. An intermediate strain state is observed around the interface between the two layers. It is expected that the different stress states around both sides of the interface induced this intermediate strain state.

Similar to the discussions on the bilayer specimen, the deformation on trilayer sample was also monitored. The results are provided and added into a comparison of bipolar longitudinal strain and polarization loops among the pure end members, bilayers and trilayers. However, owing to the lacking of more evidence, a solid explanation to understand the stress states in each layer after an electric field loading is still missing. Even though, The DIC method used in this work presents great potential for measuring complex multilayer structures thereby enabling further investigations electromechanical interactions in composites.

8 Summary of this thesis

The primary objective of this thesis is to examine the strain distributions and the polarization in piezoceramics. These results can be utilized to get a better understanding of electromechanical behavior of the materials. In addition, the experimental data are useful to build models which are served to describe the electromechanical coupling effect and develop new materials for the actuator applications.

To achieve this target, two setups equipped with digital cameras were developed. One is designed for checking the electric field-induced strain and polarization. The other is assembled for monitoring the deformation of piezoceramics under a uniaxial compression. The strains were obtained by using the DIC method and/or an LVDT, and the polarizations were measured by means of a Sawyer-Tower circuit, simultaneously.

Commercial lead-based soft PZT ceramics (PIC 151) were chosen to check the reliability of the setups. The DIC method shows advantages over other traditional methods of strain measurement. It provides both longitudinal and transverse strains from the same correlation calculation. The longitudinal strain obtained from using LVDT was taken to validate the accuracy of the DIC measurement. The errors of the DIC method used in this work were estimated by calculating the standard images of “2D test image sets” downloaded from “the Society for Experimental Mechanics”.

The distributions of strain at two particular electric field values were plotted to describe the deformation behavior. This investigation observed under the macro-scale proved that the deformation of PZT ceramic under a pure electric field loading without any mechanical constraints is homogeneous.

The DIC method is not limited to measuring the strain induced by an electric field. It also can be applied to study the deformation of piezoceramics under a compressive load. The strain components were calculated from nine selected ROIs located on the observation surface to examine the deformation on each selected region. The results reveal that the PZT specimen with an aspect ratio of 3:1 shows barreling behavior under large uniaxial compressive stresses. Furthermore, the distributions of transverse and shear strains are plotted in contour plots. These results demonstrate that the barreling behavior is due to elastic strains, in the first place, while the remnant strains are less involved in this phenomenon. The strain distributions provide the experimental supports for the selection of an aspect ratio of 3:1 in the specimens. The purely uniaxial stress state cannot be obtained from the regions close to top or bottom part, but only the region close to central cube of the specimen. In these compressive loading and unloading tests, only from the central cubic region true uniaxial stress-strain results are obtained. These data can be used for developing constitutive models.

In addition to the PZT specimens, the electric field-induced strains in lead-free piezoceramics were also measured. Electric field loads were applied on the lead-free specimens including pure NBT-7BT ceramic, pure NBT-6BT-3KNN ceramic and two types of composites combining these two end member materials.

For both the two pure ceramics, polarization and longitudinal strains were measured under cyclic electric fields. A large remnant strain can be found in NBT-7BT ceramic after the first half cycle of loading from the initial state, while there is almost no remanence in the NBT-6BT-3KNN ceramic. These are attributed to the irreversible transition from a relaxor to a ferroelectric phase upon the application of a sufficiently large electric field and the reversible transition between a relaxor to a ferroelectric phase, respectively.

In order to understand these non-ergodic and ergodic behaviors of the two relaxors, the time-dependent electromechanical responses on induced by a constant electric field were investigated. For the specimen with an initially unpoled state, the evolutions of the electric field-induced strain and polarization depend on both the hold time duration and the magnitude of the constant electric field. The state transition requires a sufficient electric field to activate RE to be transformed into the FE. An obvious macroscopic response can be observed starting from 1.15 kV/mm, approximately. When the constant electric field is higher than that value and held there for a long time, a so-called “two-stage” cascade phenomenon can be obtained. This cascade behavior under a proper constant electric field reveals that this transition is a “self-catalyzed” behavior, namely, newly formed FE induces more RE to be transformed. What’s more, the rate of this cascade development strongly relies on the magnitude of the constant electric field. This cascade phenomenon could not be observed for the specimen with a poled state, which is explained by the non-ergodic nature of the material.

Similar experiments were performed on the NBT-6BT-3KNN ceramics. The “two-stage” cascade phenomenon was not found any more on this material but it shows a time-dependent creep and reaches a final saturation eventually. The approximate values of volume resistivity were estimated from the charge leakage induced error in the measurement of polarization after a long time electric field loading. The volume resistivity is not a constant value but shows nonlinearity under various magnitudes of the static electric field.

The creep behavior of polarization and strain is primary due to the gradual state transition between RE and FE which is a reversible process. In addition, when the electric field was held constantly during the unloading process, the electric field-induced creep behavior can be explained by the exhaustion of the state transition, too.

Large creep can be observed only before the exhaustion of the RE in the loading process. Once there is not sufficient RE left to be transformed during the hold time, the higher electric field neither induces larger creeping nor drives the creeping into saturation easily. Two exponential functions were used to fit the creep curves. The fitting parameters obtained from these fittings supported this finding. However, further evidence is needed in order to explore this phenomenon in depth. For the electric unloading process, creep can be obtained prominently near the depoling field owing to the electric field here being no longer able to sustain the FE from transforming to the RE.

The electric field-induced deformations of NBT-6BT-3KNN/NBT-7BT bilayer and NBT-6BT-3KNN/NBT-7BT/NBT-6BT-3KNN trilayer composites were monitored by using the DIC method. The values of the coercive field of both the bilayer and trilayer composites are proportional to the volume fraction of each layer. By means of selecting the ROIs located on each layer and calculating the strains there, an obvious remnant strain of the RE layer and a decreased value of the FE layer can be found after the cyclic electric field loading. For the bilayer specimen used in these experiments, the full-field contour plots of strain were used to demonstrate the strain distributions. An intermediate strain state was observed around the interface between the two layers. It is expected that the mismatch of the stress states around both sides of the interface induced this intermediate strain state. After obtaining the experimental results measured from the trilayer specimens, a comparison of bipolar longitudinal strain and polarization loops among the pure end members, bilayers and trilayers was provided. However, the internal stresses induced by the variation in sintering rates between the two layers were ignored, which requires additional work to analyze the exact stress states in each layer. Especially, a model considering both polarization coupling and strain coupling is needed to understand this electromechanical behavior completely.

Overall, the strain distribution and polarization in lead-based (soft PZT) and lead-free (NBT-based) ferroelectrics were checked. The DIC method used in this thesis presents high potential for monitoring deformations on complex multilayer structures. The polarization and strain results obtained in experimental work can be utilized for constitutive modeling and developing new ferroelectrics for actuator applications.

References

- [1] S.R. Anton, H.A. Sodano, A review of power harvesting using piezoelectric materials (2003–2006), *Smart Mater. Struct.*, 16 (2007) R1-R21.
- [2] D.L. Polla, L.F. Francis, Processing and characterization of piezoelectric materials and integration into microelectromechanical systems, *Annu. Rev. Mater. Sci.*, 28 (1998) 563-597.
- [3] M.S. Senousy, F.X. Li, D. Mumford, M. Gadala, R.K.N.D. Rajapakse, Thermo-electro-mechanical Performance of Piezoelectric Stack Actuators for Fuel Injector Applications, *J. Intell. Mater. Syst. Struct.*, 20 (2008) 387-399.
- [4] R. Dittmer, W. Jo, J. Rödel, S. Kalinin, N. Balke, Nanoscale insight into lead-free BNT-BT-xKNN, *Adv. Funct. Mater.*, 22 (2012) 4208-4215.
- [5] C. Groh, D.J. Franzbach, W. Jo, K.G. Webber, J. Kling, L.A. Schmitt, H.J. Kleebe, S.J. Jeong, J.S. Lee, J. Rödel, Relaxor/ferroelectric composites: a solution in the quest for practically viable lead-free incipient piezoceramics, *Adv. Funct. Mater.*, 24 (2014) 356-362.
- [6] W. Liu, X. Ren, Large piezoelectric effect in Pb-free ceramics, *Phys. Rev. Lett.*, 103 (2009) 257602.
- [7] Y. Saito, H. Takao, T. Tani, T. Nonoyama, K. Takatori, T. Homma, T. Nagaya, M. Nakamura, Lead-free piezoceramics, *Nature*, 432 (2004) 84-87.
- [8] J. Rödel, W. Jo, K.T.P. Seifert, E.-M. Anton, T. Granzow, D. Damjanovic, Perspective on the development of lead-free piezoceramics, *J. Am. Ceram. Soc.*, 92 (2009) 1153-1177.
- [9] G.H. Haertling, Ferroelectric ceramics: History and technology, *J. Am. Ceram. Soc.*, 82 (1999) 797-818.
- [10] J. Valasek, Piezo-Electric and Allied Phenomena in Rochelle Salt, *Phys. Rev.*, 17 (1921) 475-481.
- [11] S. Roberts, Dielectric and Piezoelectric Properties of Barium Titanate, *Phys. Rev.*, 71 (1947) 890-895.
- [12] W.L. Cherry, R. Adler, Piezoelectric Effect in Polycrystalline Barium Titanate, *Phys. Rev.*, 72 (1947) 981-982.
- [13] M. Kamlah, Ferroelectric and ferroelastic piezoceramics – modeling of electromechanical hysteresis phenomena, *Continuum Mech. Thermodyn.*, 13 (2001) 219-268.
- [14] B. Wul, Barium Titanate - a New Ferro-Electric, *Nature*, 157 (1946) 808-808.
- [15] H.F. Kay, P. Vousden, XCV. Symmetry changes in barium titanate at low temperatures and their relation to its ferroelectric properties, *The London, Edinburgh, and Dublin Philosophical Magazine and Journal of Science*, 40 (1949) 1019-1040.
- [16] Y. Xu, *Ferroelectric Materials and their Applications*, Elsevier, Amsterdam, 1991.
- [17] D. Dragan, Ferroelectric, dielectric and piezoelectric properties of ferroelectric thin films and ceramics, *Rep. Prog. Phys.*, 61 (1998) 1267.
- [18] W.G. Cady, *Piezoelectricity: an introduction to the theory and applications of electromechanical phenomena in crystals*, McGraw-Hill, New York, 1946.
- [19] B. Jaffe, W.R. Cook, H.L. Jaffe, *Piezoelectric ceramics*, Academic Press, London; New York, 1971.

- [20] M.E. Lines, A.M. Glass, Principles and applications of ferroelectrics and related materials, Oxford university press, Oxford, 1977.
- [21] C.S. Lynch, The effect of uniaxial stress on the electro-mechanical response of 8/65/35 PLZT, *Acta Mater.*, 44 (1996) 4137-4148.
- [22] D. Zhou, Experimental investigation of non-linear constitutive behavior of PZT piezoceramics, Universität Karlsruhe (TH), Karlsruhe, 2003.
- [23] D. Zhou, M. Kamlah, D. Munz, Effects of Bias Electric Fields on the Non-linear Ferroelastic Behavior of Soft Lead Zirconate Titanate Piezoceramics, *J. Am. Ceram. Soc.*, 88 (2005) 867-874.
- [24] V.V. Shvartsman, D.C. Lupascu, D.J. Green, Lead-Free Relaxor Ferroelectrics, *J. Am. Ceram. Soc.*, 95 (2012) 1-26.
- [25] A.S. George, The relaxational properties of compositionally disordered ABO₃ perovskites, *J. Phys.: Condens. Matter*, 15 (2003) R367.
- [26] G.A. Smolenskii, A.I. Agranovskaya, Dielectric Polarization of a Number of Complex Compounds, *Sov. Phys.-Solid State*, 1 (1960) 1429-1437.
- [27] H. Ouchi, K. Nagano, S. Hayakawa, Piezoelectric Properties of Pb(Mg_{1/3}Nb_{2/3})O₃—PbTiO₃—PbZrO₃ Solid Solution Ceramics, *J. Am. Ceram. Soc.*, 48 (1965) 630-635.
- [28] L.E. Cross, S.J. Jang, R.E. Newnham, S. Nomura, K. Uchino, Large electrostrictive effects in relaxor ferroelectrics, *Ferroelectrics*, 23 (1980) 187-191.
- [29] S. Nomura, K. Uchino, Recent applications of PMN-based electrostrictors, *Ferroelectrics*, 50 (1983) 197-202.
- [30] H. Takenaka, I. Grinberg, Y.-H. Shin, A.M. Rappe, Computational Studies of Lead-based Relaxor Ferroelectrics, *Ferroelectrics*, 469 (2014) 1-13.
- [31] R. Dittmer, Lead-Free Piezoceramics—Ergodic and Nonergodic Relaxor Ferroelectrics Based on Bismuth Sodium Titanate, Technische Universität Darmstadt, Darmstadt, 2013.
- [32] A.A. Bokov, Z.G. Ye, Recent progress in relaxor ferroelectrics with perovskite structure, *J. Mater. Sci.*, 41 (2006) 31-52.
- [33] W. Kleemann, The relaxor enigma — charge disorder and random fields in ferroelectrics, *J. Mater. Sci.*, 41 (2006) 129-136.
- [34] Z. Ye, Relaxor ferroelectric complex perovskites: structure, properties and phase transitions, *Key Eng. Mater.*, 155-156 (1998) 81-122.
- [35] G. Burns, B.A. Scott, Index of refraction in ‘dirty’ displacive ferroelectrics, *Solid State Commun.*, 13 (1973) 423-426.
- [36] B. Mihailova, B. Maier, C. Paulmann, T. Malcherek, J. Ihringer, M. Gospodinov, R. Stosch, B. Güttler, U. Bismayer, High-temperature structural transformations in the relaxor ferroelectrics PbSc_{0.5}Ta_{0.5}O₃ and Pb_{0.78}Ba_{0.22}Sc_{0.5}Ta_{0.5}O₃, *Phys. Rev. B*, 77 (2008).
- [37] J. Toulouse, F. Jiang, O. Svitelskiy, W. Chen, Z.G. Ye, Temperature evolution of the relaxor dynamics in Pb(Zn_{1/3}Nb_{2/3})O₃: A critical Raman analysis, *Phys. Rev. B*, 72 (2005).

- [38] B. Mihailova, R.J. Angel, B.J. Maier, A.M. Welsch, J. Zhao, M. Gospodinov, U. Bismayer, The structural state of lead-based relaxor ferroelectrics under pressure, *IEEE Trans. Ultrason. Ferroelectr. Freq. Control*, 58 (2011) 1905-1913.
- [39] H.D. Rosenfeld, T. Egami, A model of local atomic structure in the relaxor ferroelectric $\text{Pb}(\text{Mg}_{1/3}\text{Nb}_{2/3})\text{O}_3$, *Ferroelectrics*, 150 (1993) 183-197.
- [40] I.K. Jeong, T.W. Darling, J.K. Lee, T. Proffen, R.H. Heffner, J.S. Park, K.S. Hong, W. Dmowski, T. Egami, Direct observation of the formation of polar nanoregions in $\text{Pb}(\text{Mg}_{1/3}\text{Nb}_{2/3})\text{O}_3$ using neutron pair distribution function analysis, *Phys. Rev. Lett.*, 94 (2005) 147602.
- [41] S. Vakhrushev, A. Nabereznov, S.K. Sinha, Y.P. Feng, T. Egami, Synchrotron X-ray scattering study of lead magnoniobate relaxor ferroelectric crystals, *J. Phys. Chem. Solids*, 57 (1996) 1517-1523.
- [42] R.F. Service, Shape-Changing Crystals Get Shiftier, *Science*, 275 (1997) 1878-1878.
- [43] W. Heywang, K. Lubitz, W. Wersing, *Piezoelectricity: evolution and future of a technology*, Springer Science & Business Media, Berlin; Heidelberg, 2008.
- [44] A.J. Moulson, J.M. Herbert, *Electroceramics: materials, properties, applications*, John Wiley & Sons, West Sussex, 2003.
- [45] F. Ebrahimi, *Piezoelectric Materials and Devices—Practice and Applications*, InTech, Rijeka, 2013.
- [46] J. Glaum, M. Hoffman, D.J. Green, Electric Fatigue of Lead-Free Piezoelectric Materials, *J. Am. Ceram. Soc.*, 97 (2014) 665-680.
- [47] M. Ahart, M. Somayazulu, R.E. Cohen, P. Ganesh, P. Dera, H.K. Mao, R.J. Hemley, Y. Ren, P. Liermann, Z. Wu, Origin of morphotropic phase boundaries in ferroelectrics, *Nature*, 451 (2008) 545-548.
- [48] T. Takenaka, K. Maruyama, K. Sakata, $(\text{Bi}_{1/2}\text{Na}_{1/2})\text{TiO}_3$ - BaTiO_3 system for lead-free piezoelectric ceramics, *Jpn. J. Appl. Phys.*, 30 (1991) 2236-2239.
- [49] D. Berlincourt, Piezoelectric ceramic compositional development, *J. Acoust. Soc. Am.*, 91 (1992) 3034-3040.
- [50] N.J. Donnelly, T.R. Shrout, C.A. Randall, Addition of a Sr, K, Nb (SKN) Combination to PZT(53/47) for High Strain Applications, *J. Am. Ceram. Soc.*, 90 (2007) 490-495.
- [51] L.A. Schmitt, H. Kungl, M. Hinterstein, L. Riekehr, H.-J. Kleebe, M.J. Hoffmann, R.-A. Eichel, H. Fuess, The Impact of Heat Treatment on the Domain Configuration and Strain Behavior in $\text{Pb}[\text{Zr,Ti}]\text{O}_3$ Ferroelectrics, *J. Am. Ceram. Soc.*, 98 (2015) 269-277.
- [52] H. Kungl, M.J. Hoffmann, Temperature dependence of poling strain and strain under high electric fields in LaSr-doped morphotropic PZT and its relation to changes in structural characteristics, *Acta Mater.*, 55 (2007) 5780-5791.
- [53] J. Rödel, K.G. Webber, R. Dittmer, W. Jo, M. Kimura, D. Damjanovic, Transferring lead-free piezoelectric ceramics into application, *J. Eur. Ceram. Soc.*, 35 (2015) 1659-1681.
- [54] W. Jo, R. Dittmer, M. Acosta, J. Zang, C. Groh, E. Sapper, K. Wang, J. Rödel, Giant electric-field-induced strains in lead-free ceramics for actuator applications – status and perspective, *J. Electroceram.*, 29 (2012) 71-93.

- [55] E. Aksel, J.L. Jones, Advances in lead-free piezoelectric materials for sensors and actuators, *Sensors*, 10 (2010) 1935-1954.
- [56] T.R. Shrout, S.J. Zhang, Lead-free piezoelectric ceramics: Alternatives for PZT?, *J. Electroceram.*, 19 (2007) 113-126.
- [57] E. Cross, Materials science: Lead-free at last, *Nature*, 432 (2004) 24-25.
- [58] L. Zhang, E. Erdem, X. Ren, R.d.A. Eichel, Reorientation of $(\text{Mn}_{\text{Ti}}''-\text{V}_{\text{O}}^-)^{\times}$ defect dipoles in acceptor-modified BaTiO_3 single crystals: An electron paramagnetic resonance study, *Appl. Phys. Lett.*, 93 (2008) 202901.
- [59] R.C. Rogan, N. Tamura, G.A. Swift, E. Ustundag, Direct measurement of triaxial strain fields around ferroelectric domains using X-ray microdiffraction, *Nat. Mater.*, 2 (2003) 379-381.
- [60] M. Ahtee, A.M. Glazer, Lattice parameters and tilted octahedra in sodium-potassium niobate solid solutions, *Acta Crystallogr., Sect. A*, 32 (1976) 434-446.
- [61] M.D. Maeder, D. Damjanovic, N. Setter, Lead Free Piezoelectric Materials, *J. Electroceram.*, 13 (2004) 385-392.
- [62] J. Acker, H. Kungl, R. Schierholz, S. Wagner, R.-A. Eichel, M.J. Hoffmann, Microstructure of sodium-potassium niobate ceramics sintered under high alkaline vapor pressure atmosphere, *J. Eur. Ceram. Soc.*, 34 (2014) 4213-4221.
- [63] Y. Guo, K.-i. Kakimoto, H. Ohsato, Phase transitional behavior and piezoelectric properties of $(\text{Na}_{0.5}\text{K}_{0.5})\text{NbO}_3\text{-LiNbO}_3$ ceramics, *Appl. Phys. Lett.*, 85 (2004) 4121.
- [64] J.-F. Li, K. Wang, B.-P. Zhang, L.-M. Zhang, Ferroelectric and Piezoelectric Properties of Fine-Grained $\text{Na}_{0.5}\text{K}_{0.5}\text{NbO}_3$ Lead-Free Piezoelectric Ceramics Prepared by Spark Plasma Sintering, *J. Am. Ceram. Soc.*, 89 (2006) 706-709.
- [65] G.A. Smolenskii, V.A. Isupov, A.I. Agranovskaya, N.N. Krainik, New Ferroelectrics of Complex Composition. IV, *Sov. Phys.-Solid State*, 2 (1961) 2651-2654.
- [66] C. Ma, H. Guo, X. Tan, A New Phase Boundary in $(\text{Bi}_{1/2}\text{Na}_{1/2})\text{TiO}_3\text{-BaTiO}_3$ Revealed via a Novel Method of Electron Diffraction Analysis, *Adv. Funct. Mater.*, 23 (2013) 5261-5266.
- [67] J. Suchanicz, W.S. Ptak, On the phase transition in $\text{Na}_{0.5}\text{Bi}_{0.5}\text{TiO}_3$, *Ferroelectrics Letters Section*, 12 (1990) 71-78.
- [68] C.S. Tu, I.G. Siny, V.H. Schmidt, Sequence of dielectric anomalies and high-temperature relaxation behavior in $\text{Na}_{1/2}\text{Bi}_{1/2}\text{TiO}_3$, *Phys. Rev. B*, 49 (1994) 11550-11559.
- [69] J. Suchanicz, A. Jeżowski, R. Poprawski, Low-Temperature Thermal and Dielectric Properties of $\text{Na}_{0.5}\text{Bi}_{0.5}\text{TiO}_3$, *Phys. Status Solidi A*, 169 (1998) 209-215.
- [70] G.O. Jones, P.A. Thomas, Investigation of the structure and phase transitions in the novel A-site substituted distorted perovskite compound $\text{Na}_{0.5}\text{Bi}_{0.5}\text{TiO}_3$, *Acta Crystallogr., Sect. B*, 58 (2002) 168-178.
- [71] Y. Hiruma, H. Nagata, T. Takenaka, Thermal depoling process and piezoelectric properties of bismuth sodium titanate ceramics, *J. Appl. Phys.*, 105 (2009) 084112.

- [72] W. Jo, J.E. Daniels, J.L. Jones, X. Tan, P.A. Thomas, D. Damjanovic, J. Rödel, Evolving morphotropic phase boundary in lead-free $(\text{Bi}_{1/2}\text{Na}_{1/2})\text{TiO}_3\text{-BaTiO}_3$ piezoceramics, *J. Appl. Phys.*, 109 (2011) 014110.
- [73] B.-J. Chu, D.-R. Chen, G.-R. Li, Q.-R. Yin, Electrical properties of $\text{Na}_{1/2}\text{Bi}_{1/2}\text{TiO}_3\text{-BaTiO}_3$ ceramics, *J. Eur. Ceram. Soc.*, 22 (2002) 2115-2121.
- [74] M. Chen, Q. Xu, B.H. Kim, B.K. Ahn, J.H. Ko, W.J. Kang, O.J. Nam, Structure and electrical properties of $(\text{Na}_{0.5}\text{Bi}_{0.5})_{1-x}\text{Ba}_x\text{TiO}_3$ piezoelectric ceramics, *J. Eur. Ceram. Soc.*, 28 (2008) 843-849.
- [75] S.-T. Zhang, A.B. Kounga, E. Aulbach, T. Granzow, W. Jo, H.-J. Kleebe, J.r. Rödel, Lead-free piezoceramics with giant strain in the system $\text{Bi}_{0.5}\text{Na}_{0.5}\text{TiO}_3\text{-BaTiO}_3\text{-K}_{0.5}\text{Na}_{0.5}\text{NbO}_3$. I. Structure and room temperature properties, *J. Appl. Phys.*, 103 (2008) 034107.
- [76] R. Dittmer, E. Aulbach, W. Jo, K.G. Webber, J. Rödel, Large blocking force in $\text{Bi}_{1/2}\text{Na}_{1/2}\text{TiO}_3$ -based lead-free piezoceramics, *Scr. Mater.*, 67 (2012) 100-103.
- [77] S.-T. Zhang, A.B. Kounga, E. Aulbach, Y. Deng, Temperature-Dependent Electrical Properties of $0.94\text{Bi}_{0.5}\text{Na}_{0.5}\text{TiO}_3\text{-}0.06\text{BaTiO}_3$ Ceramics, *J. Am. Ceram. Soc.*, 91 (2008) 3950-3954.
- [78] C. Ma, X. Tan, E. Dul'kin, M. Roth, Domain structure-dielectric property relationship in lead-free $(1-x)(\text{Bi}_{1/2}\text{Na}_{1/2})\text{TiO}_3\text{-xBaTiO}_3$ ceramics, *J. Appl. Phys.*, 108 (2010) 104105.
- [79] C. Ma, X. Tan, Phase diagram of unpoled lead-free – ceramics, *Solid State Commun.*, 150 (2010) 1497-1500.
- [80] C. Ma, X. Tan, H.J. Kleebe, In situ Transmission Electron Microscopy Study on the Phase Transitions in Lead-Free $(1-x)(\text{Bi}_{1/2}\text{Na}_{1/2})\text{TiO}_3\text{-xBaTiO}_3$ Ceramics, *J. Am. Ceram. Soc.*, 94 (2011) 4040-4044.
- [81] T. Takenaka, H. Nagata, Y. Hiruma, Phase transition temperatures and piezoelectric properties of $(\text{Bi}_{1/2}\text{Na}_{1/2})\text{TiO}_3$ - and $(\text{Bi}_{1/2}\text{K}_{1/2})\text{TiO}_3$ -based bismuth perovskite lead-free ferroelectric ceramics, *IEEE Trans. Ultrason. Ferroelectr. Freq. Control*, 56 (2009) 1595-1612.
- [82] S. Zhang, R. Xia, T.R. Shrout, Lead-free piezoelectric ceramics vs. PZT?, *J. Electroceram.*, 19 (2007) 251-257.
- [83] B. Wylie-van Eerd, D. Damjanovic, N. Klein, N. Setter, J. Trodahl, Structural complexity of $(\text{Na}_{0.5}\text{Bi}_{0.5})\text{TiO}_3\text{-BaTiO}_3$ as revealed by Raman spectroscopy, *Phys. Rev. B*, 82 (2010).
- [84] C. Groh, W. Jo, J. Rödel, Frequency and temperature dependence of actuating performance of $\text{Bi}_{1/2}\text{Na}_{1/2}\text{TiO}_3\text{-BaTiO}_3$ based relaxor/ferroelectric composites, *J. Appl. Phys.*, 115 (2014) 234107.
- [85] S.-T. Zhang, A.B. Kounga, E. Aulbach, H. Ehrenberg, J. Rödel, Giant strain in lead-free piezoceramics $\text{Bi}_{0.5}\text{Na}_{0.5}\text{TiO}_3\text{-BaTiO}_3\text{-K}_{0.5}\text{Na}_{0.5}\text{NbO}_3$ system, *Appl. Phys. Lett.*, 91 (2007) 112906.
- [86] S.-T. Zhang, A.B. Kounga, E. Aulbach, W. Jo, T. Granzow, H. Ehrenberg, J.r. Rödel, Lead-free piezoceramics with giant strain in the system $\text{Bi}_{0.5}\text{Na}_{0.5}\text{TiO}_3\text{-BaTiO}_3\text{-K}_{0.5}\text{Na}_{0.5}\text{NbO}_3$. II. Temperature dependent properties, *J. Appl. Phys.*, 103 (2008) 034108.
- [87] S.-T. Zhang, F. Yan, B. Yang, W. Cao, Phase diagram and electrostrictive properties of $\text{Bi}_{0.5}\text{Na}_{0.5}\text{TiO}_3\text{-BaTiO}_3\text{-K}_{0.5}\text{Na}_{0.5}\text{NbO}_3$ ceramics, *Appl. Phys. Lett.*, 97 (2010) 122901.

- [88] E.-M. Anton, W. Jo, D. Damjanovic, J.r. Rödel, Determination of depolarization temperature of $(\text{Bi}_{1/2}\text{Na}_{1/2})\text{TiO}_3$ -based lead-free piezoceramics, *J. Appl. Phys.*, 110 (2011) 094108.
- [89] E. Sapper, S. Schaab, W. Jo, T. Granzow, J.r. Rödel, Influence of electric fields on the depolarization temperature of Mn-doped $(1-x)\text{Bi}_{1/2}\text{Na}_{1/2}\text{TiO}_3-x\text{BaTiO}_3$, *J. Appl. Phys.*, 111 (2012) 014105.
- [90] X. Tan, E. Aulbach, W. Jo, T. Granzow, J. Kling, M. Marsilius, H.J. Kleebe, J. Rödel, Effect of uniaxial stress on ferroelectric behavior of $(\text{Bi}_{1/2}\text{Na}_{1/2})\text{TiO}_3$ -based lead-free piezoelectric ceramics, *J. Appl. Phys.*, 106 (2009) 044107.
- [91] K. Wang, A. Hussain, W. Jo, J. Rödel, D.D. Viehland, Temperature-dependent properties of $(\text{Bi}_{1/2}\text{Na}_{1/2})\text{TiO}_3$ - $(\text{Bi}_{1/2}\text{K}_{1/2})\text{TiO}_3$ - SrTiO_3 lead-free piezoceramics, *J. Am. Ceram. Soc.*, 95 (2012) 2241-2247.
- [92] C.W. Ahn, C.-H. Hong, B.-Y. Choi, H.-P. Kim, H.-S. Han, Y. Hwang, W. Jo, K. Wang, J.-F. Li, J.-S. Lee, I.W. Kim, A brief review on relaxor ferroelectrics and selected issues in lead-free relaxors, *Journal of the Korean Physical Society*, 68 (2016) 1481-1494.
- [93] W. Jo, S. Schaab, E. Sapper, L.A. Schmitt, H.-J. Kleebe, A.J. Bell, J.r. Rödel, On the phase identity and its thermal evolution of lead free $(\text{Bi}_{1/2}\text{Na}_{1/2})\text{TiO}_3$ -6 mol% BaTiO_3 , *J. Appl. Phys.*, 110 (2011) 074106.
- [94] J.E. Daniels, W. Jo, J. Rödel, J.L. Jones, Electric-field-induced phase transformation at a lead-free morphotropic phase boundary: Case study in a 93% $(\text{Bi}_{0.5}\text{Na}_{0.5})\text{TiO}_3$ -7% BaTiO_3 piezoelectric ceramic, *Appl. Phys. Lett.*, 95 (2009) 032904.
- [95] C. Ma, H. Guo, S.P. Beckman, X. Tan, Creation and destruction of morphotropic phase boundaries through electrical poling: a case study of lead-free $(\text{Bi}_{1/2}\text{Na}_{1/2})\text{TiO}_3$ - BaTiO_3 piezoelectrics, *Phys. Rev. Lett.*, 109 (2012) 107602.
- [96] M. Hinterstein, L.A. Schmitt, M. Hoelzel, W. Jo, J. Rödel, H.J. Kleebe, M. Hoffman, Cyclic electric field response of morphotropic $\text{Bi}_{1/2}\text{Na}_{1/2}\text{TiO}_3$ - BaTiO_3 piezoceramics, *Appl. Phys. Lett.*, 106 (2015) 222904.
- [97] W. Jo, T. Granzow, E. Aulbach, J. Rödel, D. Damjanovic, Origin of the large strain response in $(\text{K}_{0.5}\text{Na}_{0.5})\text{NbO}_3$ -modified $(\text{Bi}_{0.5}\text{Na}_{0.5})\text{TiO}_3$ - BaTiO_3 lead-free piezoceramics, *J. Appl. Phys.*, 105 (2009) 094102.
- [98] L.A. Schmitt, J. Kling, M. Hinterstein, M. Hoelzel, W. Jo, H.J. Kleebe, H. Fuess, Structural investigations on lead-free $\text{Bi}_{1/2}\text{Na}_{1/2}\text{TiO}_3$ -based piezoceramics, *J. Mater. Sci.*, 46 (2011) 4368-4376.
- [99] L.A. Schmitt, M. Hinterstein, H.-J. Kleebe, H. Fuess, Comparative study of two lead-free piezoceramics using diffraction techniques, *J. Appl. Crystallogr.*, 43 (2010) 805-810.
- [100] J. Kling, X. Tan, W. Jo, H.-J. Kleebe, H. Fuess, J. Rödel, In Situ Transmission Electron Microscopy of Electric Field-Triggered Reversible Domain Formation in Bi-Based Lead-Free Piezoceramics, *J. Am. Ceram. Soc.*, 93 (2010) 2452-2455.
- [101] J.E. Daniels, W. Jo, J. Rödel, V. Honkimäki, J.L. Jones, Electric-field-induced phase-change behavior in $(\text{Bi}_{0.5}\text{Na}_{0.5})\text{TiO}_3$ - BaTiO_3 - $(\text{K}_{0.5}\text{Na}_{0.5})\text{NbO}_3$: A combinatorial investigation, *Acta Mater.*, 58 (2010) 2103-2111.

- [102] C.M. Fancher, T. Iamsasri, J.E. Blendell, K.J. Bowman, Effect of Crystallographic Texture on the Field-Induced-Phase Transformation Behavior of $\text{Bi}_{0.5}\text{Na}_{0.5}\text{TiO}_3\text{-}7\text{BaTiO}_3\text{-}2\text{K}_{0.5}\text{Na}_{0.5}\text{NbO}_3$, *Mater. Res. Lett.*, 1 (2013) 156-160.
- [103] M. Acosta, *Strain Mechanisms in Lead-Free Ferroelectrics for Actuators*, Technische Universität Darmstadt, Darmstadt, 2015.
- [104] K. Wang, F.-Z. Yao, W. Jo, D. Gobeljic, V.V. Shvartsman, D.C. Lupascu, J.-F. Li, J. Rödel, Temperature-Insensitive (K,Na)NbO₃-Based Lead-Free Piezoactuator Ceramics, *Adv. Funct. Mater.*, 23 (2013) 4079-4086.
- [105] E. Hollenstein, M. Davis, D. Damjanovic, N. Setter, Piezoelectric properties of Li- and Ta-modified $(\text{K}_{0.5}\text{Na}_{0.5})\text{NbO}_3$ ceramics, *Appl. Phys. Lett.*, 87 (2005) 182905.
- [106] M. Masato, Y. Toshiaki, K. Koichi, H. Shin-ichi, Sinterability and Piezoelectric Properties of (K,Na)NbO₃ Ceramics with Novel Sintering Aid, *Jpn. J. Appl. Phys.*, 43 (2004) 7159.
- [107] D. Damjanovic, A. Biancoli, L. Batooli, A. Vahabzadeh, J. Trodahl, Elastic, dielectric, and piezoelectric anomalies and Raman spectroscopy of $0.5\text{Ba}(\text{Ti}_{0.8}\text{Zr}_{0.2})\text{O}_3\text{-}0.5(\text{Ba}_{0.7}\text{Ca}_{0.3})\text{TiO}_3$, *Appl. Phys. Lett.*, 100 (2012) 192907.
- [108] M.C. Ehmke, S.N. Ehrlich, J.E. Blendell, K.J. Bowman, Phase coexistence and ferroelastic texture in high strain $(1-x)\text{Ba}(\text{Zr}_{0.2}\text{Ti}_{0.8})\text{O}_3\text{-}x(\text{Ba}_{0.7}\text{Ca}_{0.3})\text{TiO}_3$ piezoceramics, *J. Appl. Phys.*, 111 (2012) 124110.
- [109] J. Hao, W. Bai, W. Li, J. Zhai, C. Randall, Correlation Between the Microstructure and Electrical Properties in High-Performance $(\text{Ba}_{0.85}\text{Ca}_{0.15})(\text{Zr}_{0.1}\text{Ti}_{0.9})\text{O}_3$ Lead-Free Piezoelectric Ceramics, *J. Am. Ceram. Soc.*, 95 (2012) 1998-2006.
- [110] D.R.J. Brandt, M. Acosta, J. Koruza, K.G. Webber, Mechanical constitutive behavior and exceptional blocking force of lead-free BZT-xBCT piezoceramics, *J. Appl. Phys.*, 115 (2014) 204107.
- [111] R. Dittmer, K.G. Webber, E. Aulbach, W. Jo, X. Tan, J. Roedel, Electric-field-induced polarization and strain in $0.94(\text{Bi}_{1/2}\text{Na}_{1/2})\text{TiO}_3\text{-}0.06\text{BaTiO}_3$ under uniaxial stress, *Acta Mater.*, 61 (2013) 1350-1358.
- [112] T. Takenaka, H. Nagata, Current status and prospects of lead-free piezoelectric ceramics, *J. Eur. Ceram. Soc.*, 25 (2005) 2693-2700.
- [113] Y. Hiruma, Y. Imai, Y. Watanabe, H. Nagata, T. Takenaka, Large electrostrain near the phase transition temperature of $(\text{Bi}_{0.5}\text{Na}_{0.5})\text{TiO}_3\text{-}\text{SrTiO}_3$ ferroelectric ceramics, *Appl. Phys. Lett.*, 92 (2008) 262904.
- [114] Y. Hiruma, H. Nagata, T. Takenaka, Phase diagrams and electrical properties of $(\text{Bi}_{1/2}\text{Na}_{1/2})\text{TiO}_3$ -based solid solutions, *J. Appl. Phys.*, 104 (2008) 124106.
- [115] S.T. Zhang, A.B. Kounga, W. Jo, C. Jamin, K. Seifert, T. Granzow, J. Rödel, D. Damjanovic, High-strain lead-free antiferroelectric electrostrictors, *Adv. Mater.*, 21 (2009) 4716-4720.

- [116] M. Acosta, W. Jo, J. Rödel, D.C. Lupascu, Temperature- and Frequency-Dependent Properties of the $0.75\text{Bi}_{1/2}\text{Na}_{1/2}\text{TiO}_3\text{-}0.25\text{SrTiO}_3$ Lead-Free Incipient Piezoceramic, *J. Am. Ceram. Soc.*, 97 (2014) 1937-1943.
- [117] R.A. Malik, J.-K. Kang, A. Hussain, C.-W. Ahn, H.-S. Han, J.-S. Lee, High strain in lead-free Nb-doped $\text{Bi}_{1/2}(\text{Na}_{0.84}\text{K}_{0.16})_{1/2}\text{TiO}_3\text{-SrTiO}_3$ incipient piezoelectric ceramics, *Appl. Phys. Express*, 7 (2014) 061502.
- [118] H. Kungl, R. Theissmann, M. Knapp, C. Baehtz, H. Fuess, S. Wagner, T. Fett, M.J. Hoffmann, Estimation of strain from piezoelectric effect and domain switching in morphotropic PZT by combined analysis of macroscopic strain measurements and synchrotron X-ray data, *Acta Mater.*, 55 (2007) 1849-1861.
- [119] Y.-H. Seo, J. Koruza, A. Benčan, B. Malič, J. Rödel, K.G. Webber, C. Landis, Simultaneous Enhancement of Fracture Toughness and Unipolar Strain in $\text{Pb}(\text{Zr,Ti})\text{O}_3\text{-ZrO}_2$ Composites Through Composition Adjustment, *J. Am. Ceram. Soc.*, 97 (2014) 1582-1588.
- [120] R. Dittmer, W. Jo, J. Daniels, S. Schaab, J. Rödel, D.W. Johnson, Relaxor Characteristics of Morphotropic Phase Boundary $(\text{Bi}_{1/2}\text{Na}_{1/2})\text{TiO}_3\text{-}(\text{Bi}_{1/2}\text{K}_{1/2})\text{TiO}_3$ Modified with $\text{Bi}(\text{Zn}_{1/2}\text{Ti}_{1/2})\text{O}_3$, *J. Am. Ceram. Soc.*, 94 (2011) 4283-4290.
- [121] M.-H. Zhang, K. Wang, J.-S. Zhou, J.-J. Zhou, X. Chu, X. Lv, J. Wu, J.-F. Li, Thermally stable piezoelectric properties of (K, Na) NbO_3 -based lead-free perovskite with rhombohedral-tetragonal coexisting phase, *Acta Mater.*, 122 (2017) 344-351.
- [122] Y. Huan, X. Wang, J. Koruza, K. Wang, K.G. Webber, Y. Hao, L. Li, Inverted electro-mechanical behaviour induced by the irreversible domain configuration transformation in (K,Na) NbO_3 -based ceramics, *Sci. Rep.*, 6 (2016) 22053.
- [123] D. Lin, D. Xiao, J. Zhu, P. Yu, Piezoelectric and ferroelectric properties of $[\text{Bi}_{0.5}(\text{Na}_{1-x-y}\text{K}_x\text{Li}_y)_{0.5}]\text{TiO}_3$ lead-free piezoelectric ceramics, *Appl. Phys. Lett.*, 88 (2006) 062901.
- [124] D.Q. Xiao, D.M. Lin, J.G. Zhu, P. Yu, Studies on new systems of BNT-based lead-free piezoelectric ceramics, *J. Electroceram.*, 21 (2007) 34-38.
- [125] A. Herabut, A. Safari, Processing and Electromechanical Properties of $(\text{Bi}_{0.5}\text{Na}_{0.5})_{(1-1.5x)}\text{La}_x\text{TiO}_3$ Ceramics, *J. Am. Ceram. Soc.*, 80 (1997) 2954-2958.
- [126] Y. Jae Yun, L. Jung-Kun, H. Kug Sun, The role of Cation Vacancies on Microstructure and Piezoelectricity of Lanthanum-Substituted $(\text{Na}_{1/2}\text{Bi}_{1/2})\text{TiO}_3$ Ceramics, *Jpn. J. Appl. Phys*, 43 (2004) 6188.
- [127] W. Ge, H. Liu, X. Zhao, W. Zhong, X. Pan, T. He, D. Lin, H. Xu, X. Jiang, H. Luo, Growth, optical and electrical properties of pure and Mn-doped $\text{Na}_{0.5}\text{Bi}_{0.5}\text{TiO}_3$ lead-free piezoelectric crystals, *J. Alloys Compd.*, 462 (2008) 256-261.
- [128] J. Zhang, Z. Pan, F.F. Guo, W.C. Liu, H. Ning, Y.B. Chen, M.H. Lu, B. Yang, J. Chen, S.T. Zhang, X. Xing, J. Rodel, W. Cao, Y.F. Chen, Semiconductor/relaxor 0-3 type composites without thermal depolarization in $\text{Bi}_{0.5}\text{Na}_{0.5}\text{TiO}_3$ -based lead-free piezoceramics, *Nat. Commun.*, 6 (2015) 6615.

- [129] X. Liu, X. Tan, Giant Strains in Non-Textured $(\text{Bi}_{1/2}\text{Na}_{1/2})\text{TiO}_3$ -Based Lead-Free Ceramics, *Adv. Mater.*, 28 (2016) 574-578.
- [130] D. Maurya, Y. Zhou, Y. Wang, Y. Yan, J. Li, D. Viehland, S. Priya, Giant strain with ultra-low hysteresis and high temperature stability in grain oriented lead-free $\text{K}_{0.5}\text{Bi}_{0.5}\text{TiO}_3$ - BaTiO_3 - $\text{Na}_{0.5}\text{Bi}_{0.5}\text{TiO}_3$ piezoelectric materials, *Sci. Rep.*, 5 (2015) 8595.
- [131] O.L. Serhiy, E.E. Richard, Progress in engineering high strain lead-free piezoelectric ceramics, *Sci. Technol. Adv. Mater.*, 11 (2010) 044302.
- [132] T. Shrout, W.A. Schulze, J.V. Biggers, Electromechanical Behavior of Antiferroelectric-Ferroelectric Multilayer PZT Based Composites, *Ferroelectrics*, 29 (1980) 129-134.
- [133] D.E. Dausch, E. Furman, F. Wang, G.H. Haertling, PLZT-based multilayer composite thin films, part I: Experimental investigation of composite film structures, *Ferroelectrics*, 177 (1996) 221-236.
- [134] D.E. Dausch, E. Furman, F. Wang, G.H. Haertling, PLZT-based multilayer composite thin films, part II: Modeling of the dielectric and hysteresis properties, *Ferroelectrics*, 177 (1996) 237-253.
- [135] O. Furukawa, M. Harata, M. Imai, Y. Yamashita, S. Mukaeda, Low firing and high dielectric constant X7R ceramic dielectric for multilayer capacitors based on relaxor and barium titanate composite, *J. Mater. Sci.*, 26 (1991) 5838-5842.
- [136] K. Hiroki, N. Yuichi, T. Tadashi, S. Koichiro, Piezoelectric and Pyroelectric Composite Ceramics of the Multilayer Type by Tape Casting, *Jpn. J. Appl. Phys.*, 28 (1989) 114.
- [137] V.O. Sherman, A.K. Tagantsev, N. Setter, Model of a low-permittivity and high-tunability ferroelectric based composite, *Appl. Phys. Lett.*, 90 (2007) 162901.
- [138] A. Ayrikyan, V. Rojas, L. Molina-Luna, M. Acosta, J. Koruza, K.G. Webber, Enhancing electromechanical properties of lead-free ferroelectrics with bilayer ceramic/ceramic composites, *IEEE Trans. Ultrason. Ferroelectr. Freq. Control*, 62 (2015) 997-1006.
- [139] S.-Y. Choi, S.-J. Jeong, D.-S. Lee, M.-S. Kim, J.-S. Lee, J.H. Cho, B.I. Kim, Y. Ikuhara, Gigantic Electrostrain in Duplex Structured Alkaline Niobates, *Chem. Mater.*, 24 (2012) 3363-3369.
- [140] M. Acosta, L.A. Schmitt, L. Molina-Luna, M.C. Scherrer, M. Brilz, K.G. Webber, M. Deluca, H.-J. Kleebe, J. Rödel, W. Donner, D. Johnson, Core-Shell Lead-Free Piezoelectric Ceramics: Current Status and Advanced Characterization of the $\text{Bi}_{1/2}\text{Na}_{1/2}\text{TiO}_3$ - SrTiO_3 System, *J. Am. Ceram. Soc.*, 98 (2015) 3405-3422.
- [141] D.S. Lee, D.H. Lim, M.S. Kim, K.H. Kim, S.J. Jeong, Electric field-induced deformation behavior in mixed $\text{Bi}_{0.5}\text{Na}_{0.5}\text{TiO}_3$ and $\text{Bi}_{0.5}(\text{Na}_{0.75}\text{K}_{0.25})_{0.5}\text{TiO}_3$ - BiAlO_3 , *Appl. Phys. Lett.*, 99 (2011) 062906.
- [142] C. Groh, W. Jo, J. Rödel, D. Johnson, Tailoring strain properties of $(0.94-x)\text{Bi}_{1/2}\text{Na}_{1/2}\text{TiO}_3$ - 0.06BaTiO_3 - $x\text{K}_{0.5}\text{Na}_{0.5}\text{NbO}_3$ ferroelectric/relaxor composites, *J. Am. Ceram. Soc.*, 97 (2014) 1465-1470.
- [143] H.B. Zhang, C. Groh, Q. Zhang, W. Jo, K.G. Webber, J. Rödel, Large Strain in Relaxor/Ferroelectric Composite Lead-Free Piezoceramics, *Adv. Electron. Mater.*, 1 (2015).

- [144] M.A. Sutton, W.J. Wolters, W.H. Peters, W.F. Ranson, S.R. McNeill, Determination of displacements using an improved digital correlation method, *Image Vision Comput.*, 1 (1983) 133-139.
- [145] T.C. Chu, W.F. Ranson, M.A. Sutton, Applications of digital-image-correlation techniques to experimental mechanics, *Exp. Mech.*, 25 (1985) 232-244.
- [146] Y.M. He, Y. Sun, J. Zhang, X.D. Li, An analysis of deformation mechanism in the $\text{Si}_3\text{N}_4\text{-AgCuTi} + \text{SiCp-Si}_3\text{N}_4$ joints by digital image correlation, *J. Eur. Ceram. Soc.*, 33 (2013) 157-164.
- [147] M.H. Malakooti, H.A. Sodano, Noncontact and simultaneous measurement of the $d(33)$ and $d(31)$ piezoelectric strain coefficients, *Appl. Phys. Lett.*, 102 (2013) 061901.
- [148] F. Lagattu, F. Bridier, P. Villechaise, J. Brillaud, In-plane strain measurements on a microscopic scale by coupling digital image correlation and an in situ SEM technique, *Mater. Charact.*, 56 (2006) 10-18.
- [149] Z.B. Zhou, P.W. Chen, F.L. Huang, S.Q. Liu, Experimental study on the micromechanical behavior of a PBX simulant using SEM and digital image correlation method, *Opt. Lasers Eng.*, 49 (2011) 366-370.
- [150] Z.H. Xu, M.A. Sutton, X.D. Li, Mapping nanoscale wear field by combined atomic force microscopy and digital image correlation techniques, *Acta Mater*, 56 (2008) 6304-6309.
- [151] Q.M. Zhang, W.Y. Pan, L.E. Cross, Laser interferometer for the study of piezoelectric and electrostrictive strains, *J. Appl. Phys.*, 63 (1988) 2492.
- [152] S.J. Kim, D.W. Ji, Temperature-dependent compressive creep of ferroelectric ceramics and evolution of remnant state variables, *J. Eur. Ceram. Soc.*, 33 (2013) 1779-1792.
- [153] D. Zhou, M. Kamlah, Determination of room-temperature creep of soft lead zirconate titanate piezoceramics under static electric fields, *J. Appl. Phys.*, 98 (2005) 104107.
- [154] S.E. Park, T.R. Shrout, Ultrahigh strain and piezoelectric behavior in relaxor based ferroelectric single crystals, *J Appl Phys*, 82 (1997) 1804-1811.
- [155] M.H. Malakooti, H.A. Sodano, Direct measurement of piezoelectric shear coefficient, *J. Appl. Phys.*, 113 (2013) 214106.
- [156] M. Bornert, F. Valès, H. Gharbi, D. Nguyen Minh, Multiscale Full-Field Strain Measurements for Micromechanical Investigations of the Hydromechanical Behaviour of Clayey Rocks, *Strain*, 46 (2010) 33-46.
- [157] A. Saai, H. Louche, L. Tabourot, H.J. Chang, Experimental and numerical study of the thermo-mechanical behavior of Al bi-crystal in tension using full field measurements and micromechanical modeling, *Mech. Mater.*, 42 (2010) 275-292.
- [158] P. Leplay, J. Rethore, S. Meille, M.C. Baietto, Damage law identification of a quasi brittle ceramic from a bending test using Digital Image Correlation, *J. Eur. Ceram. Soc.*, 30 (2010) 2715-2725.
- [159] X. Yang, Z. Liu, H. Xie, A real time deformation evaluation method for surface and interface of thermal barrier coatings during 1100 °C thermal shock, *Meas. Sci. Technol.*, 23 (2012) 105604.

- [160] J. Blaber, B.S. Adair, A. Antoniou, A methodology for high resolution digital image correlation in high temperature experiments, *Rev. Sci. Instrum.*, 86 (2015) 035111.
- [161] P. Wang, F. Pierron, O.T. Thomsen, Identification of Material Parameters of PVC Foams using Digital Image Correlation and the Virtual Fields Method, *Exp. Mech.*, 53 (2012) 1001-1015.
- [162] D.Y. Zhou, M. Kamlah, D. Munz, Uniaxial compressive stress dependence of the high-field dielectric and piezoelectric performance of soft PZT piezoceramics, *J. Mater. Res.*, 19 (2004) 834-842.
- [163] B. Pan, K. Qian, H. Xie, A. Asundi, Two-dimensional digital image correlation for in-plane displacement and strain measurement: a review, *Meas. Sci. Technol.*, 20 (2009) 062001.
- [164] A. Giachetti, Matching techniques to compute image motion, *Image Vision Comput.*, 18 (2000) 247-260.
- [165] W. Tong, An evaluation of digital image correlation criteria for strain mapping applications, *Strain*, 41 (2005) 167-175.
- [166] B. Pan, H. Xie, Z. Guo, T. Hua, Full-field strain measurement using a two-dimensional Savitzky-Golay digital differentiator in digital image correlation, *Opt. Eng.*, 46 (2007) 033601.
- [167] H.W. Schreier, J.R. Braasch, M.A. Sutton, Systematic errors in digital image correlation caused by intensity interpolation, *Opt. Eng.*, 39 (2000) 2915-2921.
- [168] W.G. Knauss, I. Chasiotis, Y. Huang, Mechanical measurements at the micron and nanometer scales, *Mech. Mater.*, 35 (2003) 217-231.
- [169] E. Jones, Improved Digital Image Correlation (DIC),
<<http://www.mathworks.com/matlabcentral/fileexchange/43073>>.
- [170] C. Eberl, R.J. Thompson, D.S. Gianola, S. Bundschuh, Digital Image Correlation and Tracking,
<<http://www.mathworks.com/matlabcentral/fileexchange/12413>>.
- [171] J. Carroll, W. Abuzaid, J. Lambros, H. Sehitoglu, An experimental methodology to relate local strain to microstructural texture, *Rev. Sci. Instrum.*, 81 (2010) 083703.
- [172] F. Hild, S. Roux, Digital Image Correlation: from Displacement Measurement to Identification of Elastic Properties – a Review, *Strain*, 42 (2006) 69-80.
- [173] 2D Test Image Sets, <https://sem.org/2d-test-image-sets/>.
- [174] D. Chen, M. Kamlah, Deformation in lead zirconate titanate ceramics under large signal electric field loading measured by digital image correlation, *Rev. Sci. Instrum.*, 86 (2015) 113707.
- [175] N. Lee, S.-J. Kim, Effects of loading rate and temperature on domain switching and evolutions of reference remnant state variables during polarization reversal in a PZT wafer, *Ceram. Int.*, 38 (2012) 1115-1126.
- [176] M. Kamlah, Q. Jiang, A constitutive model for ferroelectric PZT ceramics under uniaxial loading, *Smart Mater. Struct.*, 8 (1999) 441-459.
- [177] S.C. Hwang, R.M. McMeeking, A finite element model of ferroelastic polycrystals, *Int. J. Solids Struct.*, 36 (1999) 1541-1556.

- [178] D. Chen, E. Carter, M. Kamlah, Deformation behavior of lead zirconate titanate ceramics under uniaxial compression measured by the digital image correlation method, *Smart Mater. Struct.*, 25 (2016) 097001.
- [179] E.M.C. Jones, M.N. Silberstein, S.R. White, N.R. Sottos, In Situ Measurements of Strains in Composite Battery Electrodes during Electrochemical Cycling, *Exp. Mech.*, 54 (2014) 971-985.
- [180] Standard Test Method for Monotonic Compressive Strength of Advanced Ceramics at Ambient Temperature, ASTM International, (2015).
- [181] Advanced technical ceramics-Mechanical properties of ceramic composites at room temperature- Part 2: Determination of compression properties, British Standards Institution, (2002).
- [182] D. Chen, A. Ayrikyan, K.G. Webber, M. Kamlah, Time-dependent electromechanical response of $0.93(\text{Na}_{1/2}\text{Bi}_{1/2})\text{TiO}_3\text{-}0.07\text{BaTiO}_3$ lead-free piezoceramic under constant electric field, *J. Appl. Phys.*, under review, (2017).
- [183] Q.D. Liu, J.E. Huber, Creep in ferroelectrics due to unipolar electrical loading, *J. Eur. Ceram. Soc.*, 26 (2006) 2799-2806.
- [184] Piezo ceramic tutorials-typical properties, Morgan Advanced Materials, <http://www.morgantechnicalceramics.com/products/product-groups/piezo-ceramic-components/piezo-ceramic-tutorials/typical-properties>.
- [185] Technical data, PI Ceramic, http://www.pi-usa.us/pztactuators/1_32.html.
- [186] Standard Test Methods for DC Resistance or Conductance of Insulating Materials, ASTM International, (2014).
- [187] C. Kittel, Introduction to Solid State Physics-8th Edition, John Wiley & Sons, 2004.
- [188] V.V. Bryksin, T. Damker, H. Böttger, Motion of localized carriers in a strong electric field, *J. Phys.: Condens. Matter*, 10 (1998) 7907.
- [189] G. Viola, K.B. Chong, F. Guiu, M.J. Reece, Role of internal field and exhaustion in ferroelectric switching, *J. Appl. Phys.*, 115 (2014).
- [190] D.J. Green, O. Guillon, J. Rödel, Constrained sintering: A delicate balance of scales, *J. Eur. Ceram. Soc.*, 28 (2008) 1451-1466.
- [191] R. Dittmer, W. Jo, K.G. Webber, J.L. Jones, J. Rödel, Local structure change evidenced by temperature-dependent elastic measurements: Case study on $\text{Bi}_{1/2}\text{Na}_{1/2}\text{TiO}_3$ -based lead-free relaxor piezoceramics, *J. Appl. Phys.*, 115 (2014) 084108.
- [192] W. Jo, J. Rödel, Electric-field-induced volume change and room temperature phase stability of $(\text{Bi}_{1/2}\text{Na}_{1/2})\text{TiO}_3\text{-}x$ mol. % BaTiO_3 piezoceramics, *Appl. Phys. Lett.*, 99 (2011) 042901.

Acknowledgements

I would like to express my sincerest acknowledgements to all the people who helped me in this PhD work. My supervisor Prof. M. Kamlah who leads the way and shows me the direction in this exploring is the first one I would like to appreciate. His great patience and supports enlightened me during my whole study in IAM. Prof. K.G. Webber and Miss A. Ayrikyan are greatly thanked for discussing the results measured from the lead-free specimens. These ceramics prepared in their group provide me an excellent opportunity to touch the new materials. It is hard to imagine that how I could complete this work without their helps.

Mr. S. Bundschuh, Mr. D. Leisen, Dr. S. Slaby and Dr. J. Xu were the colleagues in our institute who helped me a lot in the Labview software, Matlab code and the camera system. Mr. E. Ernst is especially thanked for the technical assistance. Miss E. Cater, Mr. R. Georger and Mr. M. Viry are thanked for the assistance in the setups and experiments.

Furthermore, our group members Dr. M. Huttin, Dr. R. Annabattula, Dr. M. Feuchter, Dr. J. Ott, Mrs. M. Moscardini, Mr. T. Zhang and Mr. O. Birkholz are appreciated for the support on my work. Mr. T. Kreuter is greatly acknowledged for the language translation.

My friends and family are deeply thanked. Under their endless supports, this work can be completed.

At last, China Scholarship Council is deeply appreciated. This 4-year scholarship means a lot for me. It was so nice I got this scholarship; it is so great to meet you all in Germany.

Curriculum Vitae

Personal Information

Name: Di Chen

Gender: Male

Nationality: Chinese

Education Background

Sept. 2005 - Jun. 2009: Bachelor of Science, Inorganic Non-metallic Material Science and Engineering, Taiyuan University of Technology, China.

Sept. 2009 - Jun. 2012: Master of Science, Material Science, Hainan University, China.

Sept. 2012 - April 2017: PhD candidate, Experimental Mechanics, Institute for Applied Materials (IAM-WBM), Karlsruhe Institute of Technology (KIT), Germany.

Work Experience

Nov. 2009: Intern, Shandong shanlv cement Co., Ltd. Zibo, China.

Dec. 2009: Intern, G-Crystal Glass Group Corp. Zibo, China.

Sept. 2016 - March 2017: Research assistant, Institute for Applied Materials (IAM-WBM), Karlsruhe Institute of Technology (KIT), Germany.

Presentations in Conferences

Sept. 30 - Oct.02, 2013: The 9th International Workshop Direct and Inverse Problems on Piezoelectricity. Weimar, Germany.

Sept. 21-24, 2014: The 10th International Workshop in Direct and Inverse Problems on Piezoelectricity. Vienna, Austria.

Sep.21-23, 2015: ASME 2015 Conference on Smart Materials, Adaptive Structures and Intelligent Systems (SMASIS2015). Colorado Springs CO, USA.

August 21-25, 2016: IEEE 2016 Joint ISAF/ECAPD/PFM Conference. Darmstadt, Germany.

October 4-6, 2016: The 2nd Seminar on Ferroic Functional Materials & 12th International Workshop on Direct and Inverse Problems in Piezoelectricity. Erlangen, Germany.

Publications

1. D. Chen, H.T. Zhang, R.K. Chen, X.Y. Deng, J.B. Li, G.Q. Zhang, L.M. Wang, Well-ordered arrays of ferroelectric single-crystalline BaTiO₃ nanostructures, *Phys. Status Solidi A*, 209 (2012) 714-717.
2. D. Chen, M. Kamlah, Deformation in lead zirconate titanate ceramics under large signal electric field loading measured by digital image correlation, *Rev. Sci. Instrum.*, 86 (2015) 113707.
3. D. Chen, E. Carter, M. Kamlah, Deformation behavior of lead zirconate titanate ceramics under uniaxial compression measured by the digital image correlation method, *Smart Mater. Struct.*, 25 (2016) 097001.
4. D. Chen, A. Ayrikyan, K. G. Webber, and M. Kamlah, Time-dependent electromechanical response of 0.93(Na_{1/2}Bi_{1/2})TiO₃-0.07BaTiO₃ lead-free piezoceramic under constant electric field, *J. Appl. Phys.*, 121 (2017) 114106.